PONTIFÍCIA UNIVERSIDADE CATÓLICA
DO RIO DE JANEIRO

Esteban Camilo Moreno Diaz

Uncovering the role of $Al_2W_3O_{12}$ phase as an electrode in lithium-ion batteries

Tese de Doutorado

Thesis presented to the Programa de Pós-graduação em Engenharia Química, de Materiais e Processos Ambientais, do Departamento de Engenharia Química e de Materiais da PUC-Rio in fulfillment of the requirements for the degree of Doutor em Engenharia Química, de Materiais e Processos Ambientais.

Advisor: Prof. Bojan Marinkovic
Co-advisor: Prof. Guillermina Leticia Luque

Rio de Janeiro
September 2025

PONTIFÍCIA UNIVERSIDADE CATÓLICA
DO RIO DE JANEIRO

Esteban Camilo Moreno Diaz

Uncovering the role of $Al_2W_3O_{12}$ phase as an electrode in lithium-ion batteries

Thesis presented to the Programa de Pós-Graduação em Engenharia Química, de Materiais e Processos Ambientais da PUC-Rio, in partial fulfillment of the requirements for the degree of Doutor em Engenharia Química, de Materiais e Processos Ambientais. Approved by the Examination Committee.

Prof. Bojan Marinkovic
Advisor
Departamento de Engenharia Química e de Materiais – PUC-Rio

Prof. Guillermina Leticia Luque
Co-advisor
Universidade Nacional de Córdoba, Argentina - UNC

Prof. Anupama Ghosh
Departamento de Engenharia Química e de Materiais – PUC-Rio

Prof. Leandro Silva Rosa Rocha
Departamento de Engenharia Química e de Materiais – PUC-Rio

Prof. Elson Longo da Silva
Universidade Federal de São Carlos, Centro de Ciências Exatas e de Tecnologia - UFSCAR

Prof. Maria Victoria Bracamonte
Universidade Nacional de Córdoba, Argentina - UNC

Rio de Janeiro, September 25th 2025.

Esteban Camilo Moreno Diaz

Major in Chemistry Engineering by the Fundación Universidad de América University, Bogotá, Colombia. M.Sc. in Materials, Chemical, and Metallurgical Process Engineering, Pontifical Catholic University of Rio de Janeiro, Brazil.

Bibliographic data

Moreno Diaz, Esteban Camilo

Uncovering the role of $Al_2W_3O_{12}$ phase as an electrode in lithium-ion batteries / Esteban Camilo Moreno Diaz ; advisor: Bojan Marinkovic ; co-advisor: Guillermina Leticia Luque. – 2025.

112 f. : il. color. ; 30 cm

Tese (doutorado)–Pontifícia Universidade Católica do Rio de Janeiro, Departamento de Engenharia Química e de Materiais, 2025.

Inclui bibliografia

1. Engenharia Química e de Materiais – Teses. 2. Baterias recarregáveis. 3. Desempenho eletroquímico. 4. Capacidade de descarga. 5. Estruturas de estrutura aberta. 6. Amorfização. I. Marinkovic, Bojan. II. Luque, Guillermina Leticia. III. Pontifícia Universidade Católica do Rio de Janeiro. Departamento de Engenharia Química e de Materiais. IV. Título.

CDD: 620.11

In memory of my grandfather.

To my parents, Lilia Diaz and Eberto Moreno.

To my sister, Alejandra and my brother Nicolas.

To my grandmother Mery Oicata.

To my wife Elizabeth Verdugo

Acknowledgments

To my Advisor, Prof. Bojan Marinkovic, for his patience, support, advice, dedication, availability, and trust throughout the development of this study.

To my Co-advisor, Prof. Guillermina Leticia Luque, for her support during my visit in her laboratory, advice, patience, and human warmth that made me feel at home.

To Prof. Fernando Cometto (Institute of Physical Chemistry Research of Cordoba, UNC), for his support and advice in the analysis and measurement of the samples for XPS characterization.

To Prof. André O. Guimaraês (Physical Science Laboratory, UENF), for his collaboration and patience in the analysis and measurement of the samples for EPR characterization.

To the Laes Laboratory for their support, company, and warm welcome of their team and laboratory

To my friends from our Ceramic Materials Research Group (PUC-Rio) and CePeCAM for their total welcome and support.

To my wife, Elizabeth Verdugo, for her love, help, support, wise advice, and understanding. She has been my emotional and professional pillar throughout this process, and this achievement reflects her unconditional support.

To my family for their unconditional love, support and inspiration. To my parents, sister, brother, and my grandmother Mery. I am really grateful to share this step with them.

To the Conselho Nacional de Desenvolvimento Científico e Tecnológico (CNPQ) for the doctoral degree scholarship.

This study was financed in part by the Coordenacao de Aperfeicoamento de Pessoal de Nivel Superior - Brasil (CAPES) - Finance Code 001.

To the Coordenação de Aperfeiçoamento de Pessoal de Nível Superior (CAPES), for the scholarship provided through the CAPES-Print program.

Abstract

Esteban Camilo Moreno Diaz; Bojan Marinkovic (Advisor); Guillermina Leticia Luque (Co-advisor). **Uncovering the role of $Al_2W_3O_{12}$ phase as an electrode in lithium-ion batteries**. Rio de Janeiro, 2025. 112p. Tese de Doutorado - Departamento de Engenharia Química e de Materiais, Pontifícia Universidade Católica do Rio de Janeiro.

$Al_2W_3O_{12}$ belongs to the $A_2M_3O_{12}$ family of ceramics, which is known for its unique mechanical and thermal properties. Due to its low positive thermal expansion, this phase is a good candidate for applications that require high resistance to thermal shock. In addition, a strong interest in this ceramic family has recently emerged due to its low-density structure with a lot of empty spaces likely capable of storing alkaline ions. Therefore, these orthorhombic open-framework structures can be potentially useful as electrodes in lithium-ion batteries (LIBs).

Here, $Al_2W_3O_{12}$ was synthesized by co-precipitation method and subsequently used as active material in LIBs, achieving a discharge capacity of 130 mA h g^{-1} at the 100^{th} cycle. Two post-synthesis routes are applied to add carbon phases to $Al_2W_3O_{12}$, thus providing an additional mechanism to tune the energy delivered using $Al_2W_3O_{12}$ as the active material. The first route for carbon addition considered mechanical mixing of the as-obtained ceramic powder with graphite, achieving a discharge capacity of 240 mA h g^{-1} at the 100^{th} cycle. In the second approach, sucrose impregnation followed by a dehydration step within a strong acid medium was used as a carbon source, and the discharge capacity of this material was 230 mA h g^{-1} at the 100^{th} cycle. Electrochemical performance of all three materials was thoroughly studied.

The presence of the carbon coating was confirmed by Raman spectroscopy, thermogravimetric analysis (TGA), scanning transmission electron microscopy (STEM), and energy dispersive X-ray spectroscopy (EDS). X-ray powder diffraction (XRPD), X-ray photoelectron spectroscopy (XPS), and scanning electron microscopy (SEM) were used to study $Al_2W_3O_{12}$ before and after lithiation.

On the other hand, some members of the open-framework $A_2M_3O_{12}$ ceramic family containing oxygen vacancies (OV), have been investigated as candidates

for photocatalytic applications and those requiring high thermal shock resistance, due to their negative or near-zero thermal expansion. In addition, OV can enhance capacity, rate performance, and promote Li^+ diffusion in LIB. Therefore, this study also compares the electrochemical properties of $Al_2W_3O_{12}$-based electrodes with and without OV as a new anode in LIB. Extrinsic OV were introduced into $Al_2W_3O_{12}$ through heat treatment in a hydrogen atmosphere, and the resulting ceramic powder was used as the active material. Electron paramagnetic resonance (EPR) confirmed the presence of OV in the $Al_2W_3O_{12}$ ceramic. The OV-containing electrode delivered a discharge capacity of 110 mAh g^{-1} at the 100^{th} cycle, which was lower than that of the electrode without OV (133 mAh g^{-1} at the 100^{th} cycle). In order to explain the reduced performance of the OV-containing electrode, XRPD and SEM were used to analyze structural and morphological changes before and after lithiation.

In conclusion, this study found that the addition of carbon to $Al_2W_3O_{12}$ is a promising approach to enhance charge storage capacity and electrochemical performance of open-framework $A_2M_3O_{12}$-based phases. Furthermore, this work unravels important considerations for evaluating OV as a potential strategy to improve the electrochemical properties of other $A_2M_3O_{12}$-based electrodes in LIB.

Keywords

Rechargeable batteries; Electrochemical performance; Discharge capacity; Open-framework structures; Amorphization.

Resumo

Esteban Camilo Moreno Diaz; Bojan Marinkovic (Advisor); Guillermina Leticia Luque (Co-advisor). **Revelando o papel da fase $Al_2W_3O_{12}$ como eletrodo em baterias de íon-lítio**. Rio de Janeiro, 2025. 112p. Tese de Doutorado - Departamento de Engenharia Química e de Materiais, Pontifícia Universidade Católica do Rio de Janeiro.

$Al_2W_3O_{12}$ pertence à família cerâmica $A_2M_3O_{12}$, conhecida por suas propriedades mecânicas e térmicas únicas. Devido à sua baixa expansão térmica positiva, essa fase é uma boa candidata para aplicações que exigem alta resistência a choque térmico. Além disso, recentemente surgiu um forte interesse por essa família cerâmica devido à sua estrutura de baixa densidade, com muitos espaços vazios, provavelmente capazes de armazenar íons alcalinos. Portanto, essas estruturas ortorrômbicas de rede aberta podem ser potencialmente úteis como eletrodos em baterias de íons de lítio (BILs).

Aqui, o $Al_2W_3O_{12}$ foi sintetizado pelo método de coprecipitação e, posteriormente, utilizado como material ativo em BILs, alcançando uma capacidade de descarga de 130 mA h g^{-1} no 100^{th} ciclo. Duas rotas pós-síntese foram aplicadas para recobrir e misturar o $Al_2W_3O_{12}$ com diferentes fases de carbono, fornecendo, assim, um mecanismo adicional para ajustar a energia fornecida pela BIL utilizando o $Al_2W_3O_{12}$ como material ativo. A primeira rota para adição de carbono considerou a mistura mecânica do pó cerâmico obtido com grafite, alcançando uma capacidade de descarga de 240 mA h g^{-1} no 100^{th} ciclo. Na segunda abordagem, utilizou-se impregnação com sacarose seguida de uma etapa de desidratação em meio ácido forte como fonte de carbono, e a capacidade de descarga desse material foi de 230 mA h g^{-1} no 100^{th} ciclo. O desempenho eletroquímico dos três materiais foi amplamente estudado.

A presença do revestimento de carbono foi confirmada por espectroscopia Raman, análise termogravimétrica e microscopia eletrônica de transmissão de varredura e espectroscopia (MEV) de raios X dispersiva de energia. Difração de raios X de pó (DRXP), espectroscopia de fotoelétrons de raios X e microscopia eletrônica de varredura foram utilizadas para estudar o $Al_2W_3O_{12}$ antes e depois da litiação.

Por outro lado, alguns membros da família cerâmica $A_2M_3O_{12}$ de rede aberta contendo vacâncias de oxigênio (VO), têm sido investigados como candidatos para aplicações fotocatalíticas e para aquelas que exigem alta resistência a choque térmico, devido à sua expansão térmica negativa ou próxima de zero. Além disso, as VO podem aumentar a capacidade, melhorar o desempenho em altas taxas e promover a difusão de Li^+ em BILs. Por tanto, este estudo também compara as propriedades eletroquímicas de eletrodos à base de $Al_2W_3O_{12}$ com e sem VO como um novo ânodo em BIL. VO extrínsecas foram introduzidas no $Al_2W_3O_{12}$ por meio de tratamento térmico em atmosfera de hidrogênio, e o pó cerâmico resultante foi utilizado como material ativo. A ressonância paramagnética eletrônica confirmou a presença de VO na cerâmica de $Al_2W_3O_{12}$. O eletrodo contendo VO apresentou capacidade de descarga de 110 mA h $g^{-1}100^{th}$ ciclo, inferior à do eletrodo sem VO (133 mA h g^{-1} no 100^{th} ciclo). Para explicar o desempenho reduzido do eletrodo contendo VO, DRXP e MEV foram utilizados para analisar as mudanças estruturais e morfológicas antes e depois da litiação.

Em conclusão, este estudo constatou que a adição de carbono ao $Al_2W_3O_{12}$ é uma abordagem promissora para aumentar a capacidade de armazenamento de carga e o desempenho eletroquímico de fases da família $A_2M_3O_{12}$ de rede aberta. Além disso, este trabalho revela considerações importantes para avaliar as VO como estratégia potencial para melhorar as propriedades eletroquímicas de outros eletrodos à base de $A_2M_3O_{12}$ em BILs.

Palavras-chave

Baterias recarregáveis; Desempenho eletroquímico; Capacidade de descarga; Estruturas de estrutura aberta; Amorfização.

Content

Figure list

Table list

1
Introduction

The excessive use of fossil energy sources such as coal and petroleum leads to negative environmental consequences. Governments and the academic community constantly seek alternative energy sources to find a lasting alternative to traditional energy sources [1,2]. Sun and wind are the most promising alternatives, and with the greatest energy potential, among the renewable energy sources currently available. However, these energy sources have their limitations such as energy storage since they are intermittent and need to be stored for further use.

Lithium-ion batteries (LIBs) are considered one of the most important solutions for energy storage. Some authors called them the ”holy grail” of energy storage technology due to their advantages such as long cycle life, low self-discharge, and high energy density [3,4]. Since the beginning of commercialization in 1991, LIBs have also been an important part of the vast majority of electronic devices, such as smartphones, laptops, and electric cars [5]. In addition, they have been considered for storage of surplus of energy coming from intermittent renewable sources.

Nevertheless, there is a need for new and better electrode materials with higher specific capacity compared to the commonly used graphite, and those that allow for the replacement of Co in conventional cathode material, which are plagued by the problems including price volatility, and fragile supply chain [6]. Furthermore, some issues need to be overcome related to the exothermic processes caused by the diffusion resistance of Li^+ and the intrinsic resistance of all the components in the LIBs [7]. This issue concerns to safety, since the exothermic processes in LIBs may lead to battery explosions due to component failure caused by significant volumetric changes [8]. In this context, it is necessary to develop safer materials to enhance LIBs performance.

Due to their unique crystal structure, members of the $A_2M_3O_{12}$ ceramic family have shown promising performance as electrode materials in LIBs [7,9–12]. These ceramics are well known for their unique properties, including negative thermal

expansion or near zero thermal expansion [13]. Therefore, some of their potential applications have been focused on resolving thermal shock resistance-related issues [14,15]. However, their peculiar thermal expansion can be utilized beneficially to mitigate the volumetric changes caused by exothermic processes that take place within LIBs [7,8,16,17], assuming the crystal structure remains intact during cycling. The $A_2M_3O_{12}$ ceramics consist of MO_4 and AO_6 polyhedral connected through 2-folded oxygen linkers to form *A*-O-*M* bridges, where *A* is a trivalent cation, form Al and Dy, and *M* is either W^{6+} or Mo^{6+} [18,19]. This vertex connected polyhedral structure can form either orthorhombic or monoclinic phases. The phase stable at room temperature depends on the chemical composition and electronegativity of cations [20]. When orthorhombic, it is an open framework structure with channels with sufficient space to allow for diffusion and storage of lithium ions, which could increase Li^+ storage capacity and increase the lifespan of LIBs [10,11,21] .

To improve the performance of these poorly electrically conductive materials as electrodes in LIBs, one of the strategies is the carbon coating or modification of the active material [22–25]. The presence of carbon in certain ceramics can enhance electrical conductivity by serving as a conductive network for electrons [26]. This favors kinetics optimization, accelerates electron transfer, provides mechanical stabilization, and aids in thermal dissipation during charging and discharging processes [27].

Different studies on carbon content and its influence on the electrochemical performance was conducted on specific members of the $A_2M_3O_{12}$ ceramic family, including $Cr_2Mo_3O_{12}$ [12] and $Y_2W_3O_{12}$ [9]. The $Cr_2Mo_3O_{12}$ nanorods in graphene composite was used as anode exhibiting a significant reversible capacity of 988 mA h g^{-1} after 50 cycles at a current density of 100 mA g^{-1}, along with excellent rate capability. The other one, $Y_2W_3O_{12}$, was synthesized using a conventional solid-state synthesis method, followed by carbon addition using sucrose as a carbon source. The resultant carbon-coated ceramic exhibited excellent rate performance and notable long-term cycling stability, keeping a high capacity of 140 mA h g^{-1} after 2000 cycles.

However, previous research [11] has not extensively explored carbon addition (coating or mixing) onto $Al_2W_3O_{12}$ phase, although this procedure represents an opportunity to potentially improve its electrochemical properties. Considering

lower cost of $Al_2W_3O_{12}$, compared to other members of the $A_2M_3O_{12}$ family [15], and its low-positive thermal expansion coefficient (1.5 x 10^{-6} K^{-1}) [13], our study employed graphite and sucrose as the carbon precursors to investigate the influence of carbon addition (mixing and coating) on the $Al_2W_3O_{12}$-based electrode and its potential application in LIBs.

On the other hand, point defects such as oxygen vacancies (OV) have been used as an alternative to improve electrode performance in LIBs [28–32]. The introduction of OV in the active material can modify the electronic structure of the metal oxide, resulting in improved electrical conductivity and reduced ion diffusion barrier [33]. Furthermore, the formation of OV creates new active sites that can be utilized for ion storage, leading to enhanced efficiency [34]. Lastly, ion transfer can be favored since the presence of OV may lead to an imbalanced charge distribution and the formation of an electric field [35].

However, the majority of the studies of OV in the members of the $A_2M_3O_{12}$ family have focused on tailoring the coefficient of thermal expansion (CTE) [36–39] or, recently, as efficient visible-light-driven photocatalysts [40]. For example, Moreno et al. [41] synthesized $Al_2W_3O_{12}$ with OV showing that OV can cause a reduction of CTE as high as 40 %. Furthermore, they observed a slight enlargement of unit-cell volumes when OV were formed. Recently, Gil et al. [42] studied the influence of OV on electrical properties in $Al_2W_3O_{12}$. The authors demonstrated that improvement in electrical conductivity is linked with the presence of OV, and suggested that this type of defect could be beneficial for applications in energy storage. Therefore, OV could enhance the intrinsic electrochemical properties of members of $A_2M_3O_{12}$.

Despite progress in understanding the influence of OV on some properties of $Al_2W_3O_{12}$, the role of OV in their electrochemical performance remains poorly understood. In this study, we investigate the effect of OV in $Al_2W_3O_{12}$ ceramics on their electrochemical properties to evaluate their potential as electrode materials for LIBs.

This doctoral thesis aims to demonstrate potential application of $Al_2W_3O_{12}$ phase with OV, and the carbon modification as active material for electrodes in LIBs.

Thus, the doctoral thesis proposal is organized as follows:

Chapter 1: Introduction

Chapter 2: Literature review, which presents the fundamentals and parts of LIBs, the potential use of the $Al_2W_3O_{12}$ as active material in electrodes for LIB, and the effects of incorporating OV, and carbon in $Al_2W_3O_{12}$. This section intends to elucidate two new methods for improving $Al_2W_3O_{12}$ as an active material for LIBs.

Chapter 3: Objetives;

Capítulo 4: Materials and methods;

Chapter 5: Effects of carbon and OV in $Al_2W_3O_{12}$ based electrodes;

Chapter 6: Conclusions and future works;

Chapter 7: Bibliography;

2
Literature review

2.1
Lithium-ion battery (LIB) overview

The first commercially used lithium-ion batteries (LIBs) in electronic devices date back to 1991, and since then, their use has considerably increased [43]. LIBs make up 63% of the sales value of electronic devices, as they offer the best balance between high energy density and design flexibility. The most commonly used designs for LIBs are cylindrical, coin, prismatic, and pouch cells [44]. Additionally, lithium can deliver a large amount of energy despite per weight and volume, as shown in Figure 1. Therefore, lithium is the best option so far to be used as the primary source in rechargeable batteries.

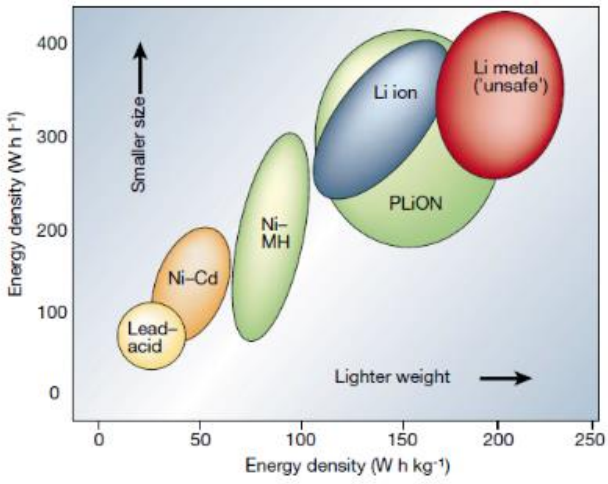

Figure 1: Comparison of the different battery technologies by the amount of electrical energy per unit of weight and per unit of volume that rechargeable batteries can deliver [44].

Batteries can be classified into two types: primary and secondary. Primary batteries can only be used once, while secondary batteries, also known as rechargeable batteries, can be discharged and charged (*i.e.*, cycled) multiple times

[45]. The most basic unit of a battery is called a "*cell*," with a nominal voltage of around ~3.2 V per cell for LIBs. A battery may comprise numerous cells connected in series or/and parallel to increase the delivery voltage and specific energy [46].

2.1.1 LIB components

Each battery cell comprises of two electrodes, an electrolyte, a separator, and current collectors. The schematic representation of the components of the LIB is shown in Figure 2.

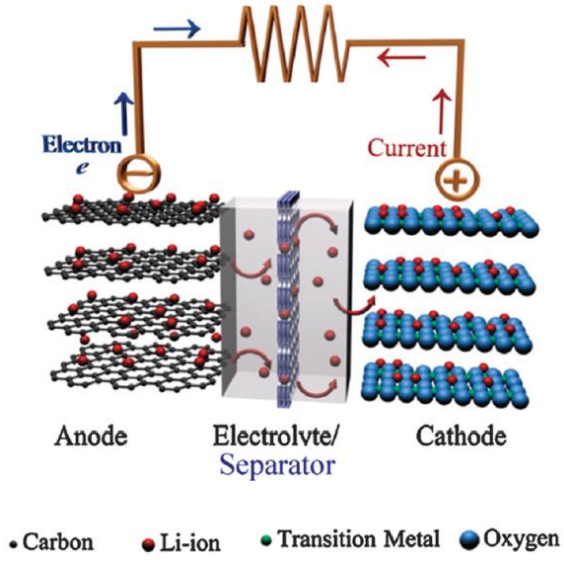

Figure 2: Schematic representation of the components of a LIB [47]**.**

Electrodes are based on active materials capable of storing Li ions. The positive electrode is called the cathode and is typically composed of LiMO_2, where *M* represents a transition metal. The negative electrode is known as the anode and is commonly made of graphite [48].

The components that do not store ions are referred to as inactive materials, including the separator, electrolyte, carbon additives, binder and current collector. The separator is typically a microporous polymer membrane that selectively permits the passage of ions. Its primary function is to prevent direct contact between the electrodes, thereby avoiding a short circuit [49].

Most of electrolytes used in batteries are in the form of electrolytic solutions, which consist of salts dissolved in organic solvents. Additionally, the electrolyte

demonstrates good ionic conductivity while having poor electronic conductivity. Consequently, the electrolyte facilitates the movement of ions within the cell [50].

The current collector serves two main functions: it supports the active material and facilitates the collection of electrons generated during the electrochemical reaction. These electrons are then transported through the current collector to the external circuit, completing the electrical pathway [51].

Modern LIBs are typically composed of a composite electrode that incorporates a carbon additive and a binder. The commonly employed additives for this purpose are carbon super P and other carbon nanoparticles. Carbon additives are crucial for the ion/electron transport process and the electrochemical reaction, ensuring the electrode stability under various operating conditions such as extended cycle life and fast charging processes [27]. The binders traditionally used in LIBs are composed of a polymer, which adheres to the active materials and other additives and play an essential role in mechanical stabilization of electrode. This part of the battery should enable the transport of electrons and ions and enhance the dispersion of the active particles [52].

2.1.2 Fundamentals of LIB

The energy delivery process occurs when the electrodes are externally connected, forming a closed circuit. When the device is plugged in (charging) lithium ions are released from the cathode to the anode. During battery discharge, (converting chemical energy into electric energy), the anode releases lithium ions to the cathode, generating, at the same time, a flow of electrons from anode to cathode through external circuit. During this cycle, Li^+ ions intercalate into the cathode, and store either in the crystal voids of the cathode lattice or between atomic planes, such as in the case of layered transition oxides, $LiMO_2$ [47,53]. The discharge cycle of LIB is illustrated in Figure 3.

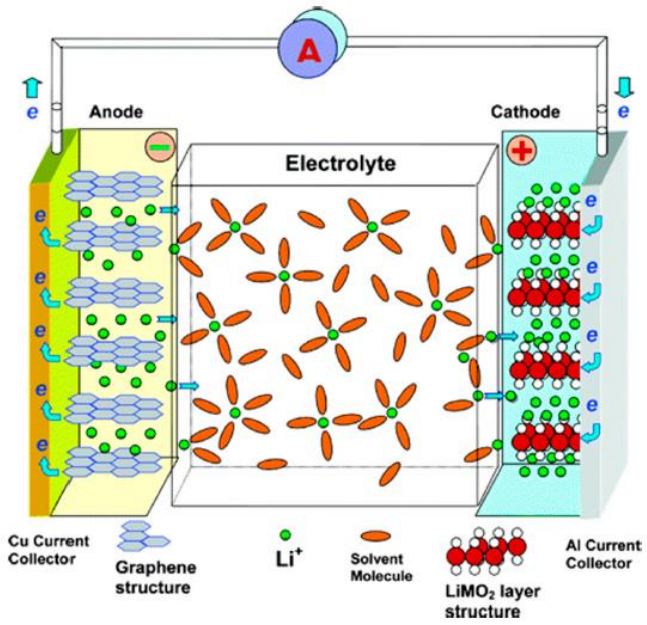

Figure 3: Schematic representation of the discharge process within LIB [45].

Thermodynamic principles that take place when the battery is undergoing a chemical reaction within a LIB can be explained by utilizing the change in Gibbs free energy (Δ*G)*. Equation 1 represents the Gibbs free energy in a battery:

Equation 1: Gibbs free energy in a battery.

$$\Delta G = -nFE$$

where *n* is the number of electrons transferred per mole of reactants, *F* is the Faraday constant, and *E* is the cell potential (electrical driving force of the cell).

A negative ΔG indicates a spontaneous process, meaning it can occur without any external intervention. On the other hand, a positive ΔG indicates a non-spontaneous process, which requires an external event to start. Therefore, to release electrons from the anode to the cathode, the ΔG value must be negative. This last is obtained when the cell potential E (the potential difference between the cathode and anode) is positive between two points in an electric circuit [54].

When the battery reaches thermodynamic conditions, the electrochemical reactions that take place at the electrodes are [55]:

At the cathode:

$$LiMO_2 \leftrightarrow Li_{1-x}MO_2 + xLi^+ + xe^-$$

At the anode:

$$C + xLi^+ \leftrightarrow Li_xC$$

Finaly, the overall reactions in the cell:

$$LiMO_2 \leftrightarrow Li_{1-x}MO_2 + xLi^+ + xe^-$$

2.2 Overview of the Electrochemical Properties in LIB

LIBs are characterized by several key electrochemical properties that determine their performance and applicability. These properties include specific capacity, coulombic efficiency, rate capability, and cycle life. Understanding these parameters is essential for evaluating the behavior of active materials and optimizing battery performance. Electrochemical techniques such as galvanostatic charge–discharge testing, and cyclic voltammetry are commonly employed to probe these characteristics.

2.2.1 Specific capacity

Specific capacity, commonly expressed in milliampere-hours per gram (mAh g^{-1}), measures the amount of charge a battery material can store per unit mass. It is a critical parameter for assessing the potential of new battery materials, as it directly correlates with the energy density of a battery system. The calculation of specific capacity considers the mass of the battery components, including the anode, cathode, and separator [56].

2.2.2 Coulombic efficiency

Coulombic efficiency (CE) in LIB refers to the percentage of the charge that can be recovered during discharge relative to the total charge supplied during charging. CE reflects the efficiency of the charge–discharge process and indicates how much of the input charge is available for practical use [57].

A CE value close to 100 % indicates that nearly all the charge introduced into the battery can be recovered, implying minimal side reactions and energy losses. Under ideal operating conditions, LIBs typically exhibit CE values above 99 %, although factors such as rapid charging, temperature variations, and battery aging can lower this efficiency. CE is a key parameter for assessing battery performance, as higher values are associated with improved cycle life and better capacity retention.

2.2.3 Rate capability

The rate capability of a battery refers to its ability to deliver a certain amount of capacity (charge) at different charging or discharging rates. A battery with high rate capability can provide considerable power with minimal voltage loss even at high current loads, meaning it can charge or discharge quickly without significant drop in performance. On the other hand, a battery with low rate capability will experience greater voltage loss and reduced capacity at higher rates, making it more suitable for slower, energy-optimized applications.[58]

2.2.4 Cycle life

The cycle life of a battery refers to the number of full charge and discharge cycles it can go through before its capacity drops to a set limit, usually about 80% of its initial value. It shows how many times the battery can be used before its performance starts to decline considerably. Cycle life matters because it defines how long a battery remains useful. A longer cycle life means the battery can be used more times, lowering replacement needs and costs while keeping performance stable over time. This is particularly important in areas such as electric vehicles, portable devices, and energy storage systems, where battery durability strongly affects both cost and sustainability [59].

2.3
Overview of Cathodes in LIB

Cathodes play a crucial role in LIB by storing and releasing lithium ions during the charge and discharge processes, respectively. The cathode materials commonly employed in LIB include layered lithium transition metal oxides LiMO_2 (where *M* represents elements such as Fe, Mn, Co, Ni, Ti, V, etc.), spinel lithium transition metal oxides, polyanion compounds encompassing phosphates, silicates, fluorophosphates, fluorosilicates, and borates [47].

Traditional cathodes in LIBs typically exhibit three characteristic structures: layered, spinel, and olivine, as depicted in Figure 4.

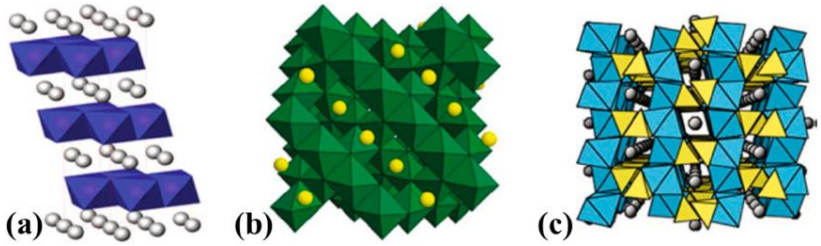

Figure 4: The traditional cathode structure for LIBs can be classified into three main types: (a) layered oxide $LiCoO_2$, (b) spinel $LiMn_2O_4$, and (c) olivine $LiFePO_4$ [45]**.**

Among the cathode materials available in the market, 2D $LiCoO_2$ compound has emerged as the most successful choice for portable devices, finding extensive utilization in smartphones. However, it is worth noting that commercial $LiCoO_2$ exhibits a maximum capacity of approximately 148 mAh g^{-1}, which is considered relatively moderate compared to other cathode materials, such as $LiN_{i0.33}Mn_{0.33}Co_{0.33}O_2$ with 170 mAh g^{-1} or $LiNi_{0.8}Co_{0.15}Al_{0.05}O_2$ with 200 mAh g^{-1} [60–62]. In addition, the $LiCoO_2$ chemistry presents challenges for large-scale applications due to its high cost, mainly attributed to the limited availability of cobalt sources. Furthermore, cobalt is a toxic substance, and the development of environmentally friendly recycling technologies on a commercial scale is still pending [63–65].

The traditional spinel cathode, such as $LiMn_2O_4$, belongs to the LiM_2O_4 family of cathodes and is characterized by a 3D network structure. The presence of a 3D network in the crystal structure of spinel oxides allows for the rapid diffusion

of lithium ions through multiple channels, facilitating easy insertion and extraction from the structure. As a result, spinel oxides exhibit exceptional reversible capacity for Li intercalation and prolonged cycling stability. However, one of the issues with this cathode is the dissolution of Mn, resulting in phase transformation and a decrease in storage capacity. To prevent the dissolution of Mn ions, the cathode is often doped with other metals; however, this can increase the production costs [45,47].

The last class of traditional cathodes is the $Li_xM_y(XO_4)_z$ family, where *M* can be Fe, Mn, Co, or Ni, and X can be P, S, Si, Mo, W, etc. Despite the versatility of elements that can be part of this type of cathode, the most notable one is $LiFePO_4$ [66]. This cathode exhibits great stability and wide cycle life, and Fe is one of the most abundant elements, making its synthesis more cost-effective. However, it only has one ion intercalation channel, limiting its capacity [45,47]. Table 1 presents the experimental and theoretical specific capacities of the principal cathodes used in LIBs.

Table 1: The typical capacities of the three traditional types of cathodes.

Traditional cathode material	Theoretical specific capacity (mAh g^{-1})	Experimental specific capacity (mAh g^{-1})	Ref.
$LiCoO_2$	248	148	[67]
$LiMn_2O_4$	148	120	[68]
$LiFePO_4$	170	165	[69]

2.4 Overview of Anodes in LIB

The anode is a critical component of secondary batteries and, due to its properties and morphology, has a significant impact on the overall performance of the device. Graphite is widely employed in commercial anodes because of its unique layered crystal structure, which provides intercalation sites for lithium ions and helps prevent shape and size changes during charge–discharge cycles. In addition, graphite demonstrates excellent cyclic stability [70]. However, despite these advantages, graphite anodes also present important limitations. They suffer from low capacity and safety concerns, such as lithium deposition. Moreover, they

exhibit limited specific capacity and rate capability, and their use is further associated with safety risks [71].

While graphite remains the most common anode material, its limitations have prompted the exploration of alternative candidates. Alloy-based anodes, such as those made from Si, Sn, Ge, or Sb, offer specific capacities 2 to 10 times higher than those of carbon materials [72]. Furthermore, they exhibit excellent processing qualities and high charge–discharge capacity. However, their main drawbacks include massive volumetric expansion during new phase formation, which compromises LIB performance, poor electrical conductivity, significant variations in material volume, irreversible capacity loss during the first cycle, and rapid capacity fading in subsequent cycles [73].

Given these limitations, alternative anode materials have also been explored. Among them, Si is regarded as an exceptional candidate due to its high gravimetric and volumetric capacity, natural abundance, low cost, and the absence of safety risks commonly associated with graphite electrodes [74]. Despite its remarkable potential, Si anodes face significant challenges, primarily large volume variations (up to 400%) during cycling, which cause irregular electrical contact and particle cracking [75]. These issues ultimately lead to reduced practical capacity and poor cyclability.

The study of new active materials is essential to improve the performance of LIBs. Therefore, investigating the $A_2M_3O_{12}$ ceramic family and its potential use as an electrode material could be an alternative. Although $A_2M_3O_{12}$ materials are primarily recognized for their low-positive, near-zero, and negative thermal expansion (NTE) characteristics, only a few studies have investigated their electrochemical properties [9–12].

2.5 Mechanisms of NTE

The increase in the volume of material is typically associated with temperature increases. Most solids exhibit this behavior, known as positive thermal expansion (PTE) [76]. However, some materials exhibit anomalous behavior when heated. Several thermomiotic (those which reduce their dimension when heated) materials show a reduction in volume or do not present significant volume changes

when temperature increases. These behaviors are known as NTE or near-zero thermal expansion (NZTE), respectively [77].

One way to explain this anomalous behavior, *i.e.*, NZTE and NTE, is through atomic vibrations. A quantized lattice vibration in a crystal is commonly referred to as a phonon, which can exist in either longitudinal form (as shown in Figure 5a) or transverse form (as seen in Figures 5b and 5c) [19]. The latter can be further divided into high-energy optical or low-energy acoustic categories [78].

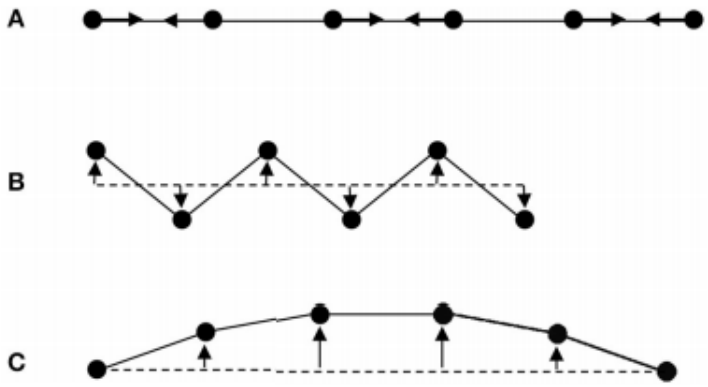

Figure 5: Schematic representation of (a) longitudinal vibrations (b) optical transverse vibrations, and (c) acoustic transverse vibrations [78]**.**

The schematic depiction shown in Figure 6 illustrates the vibrational interactions between two metals connected by a 2-folded oxygen linker (M-O-M). When longitudinal motion occurs due to the asymmetry of the potential well, the connected chain of atoms tends to elongate as the temperature increases, which can result in PTE. However, in cases where transverse vibrations dominate, the angular movement of oxygen atoms tends to compress the distance between M-M atoms in the chain, leading to a decrease in volume and, consequently NTE, if this transverse vibration contribution outweighs the longitudinal bond lengthening [13,17].

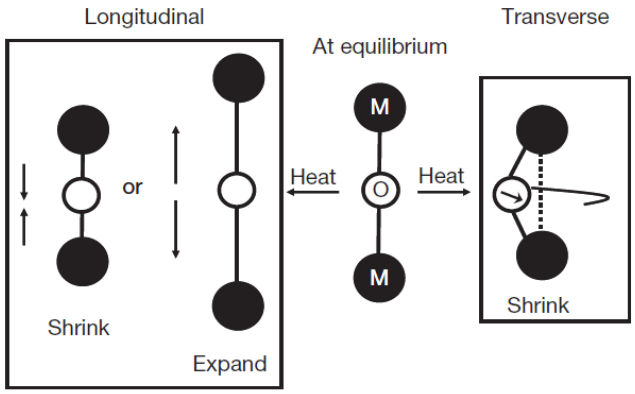

Figure 6: Longitudinal vibrations increase the interatomic distance. The angle formed by transverse vibrations shortens the distance between the atoms [19].

2.6 Overview of the $A_2M_3O_{12}$ ceramic family

Some ceramic families exhibit NTE or NZTE, such as AM_2O_8, AM_2O_7, $A_2M_4O_{15}$, and $A_2M_3O_{12}$. The $A_2M_3O_{12}$ family is particularly interesting due to its exceptional chemical flexibility while maintaining an orthorhombic, low-density, crystal structure. Within this family, there are numerous crystalline phases, where *A* is a trivalent cation, and *M* being either W^{6+} or Mo^{6+} [77].

Certain characteristics, such as the size of the cation A, influence the thermal expansion properties of the orthorhombic phase. On one hand, due to its relatively small ionic radius of 0.54 Å, Al^{3+} is effective in forming small channels within the crystal structure blocking the entry of water molecules, preserving the orthorhombic structure [77,79,80]. As a result, the phase with Al^{3+} is not negatively affected by humidity. On the other hand, a larger atomic radius, such as that of Y^{3+} (1.01 Å) [81] tends to favor larger channels within the crystal structure, enabling the entry of molecules like water. When water molecules are present within the orthorhombic phase, they can impede the contribution of transverse motions through steric hindrance. As a result, the NTE or NZTE can be impacted while the material can also be amorphized.

The $A_2M_3O_{12}$ ceramics, also known as *"thermomiotic ceramics"* (from the Greek, 'thermo' for 'heat' and 'mio' for 'contract') have a unique structure where the atoms are arranged in tetrahedra and octahedra that are connected by vertices to create an open framework with low density. The low density of the orthorhombic

structure facilitates the transverse movement of two-folded linkers (oxygen anions). An open framework structure is ideal for NTE or NZTE because it allows transverse movements without being constrained by neighboring atomic species' steric effect [76,77].

Another characteristic of the $A_2M_3O_{12}$ family contributing to the NTE is strong A-O and M-O bonds [76] with a less asymmetric potential well. An example of this type of crystal structure is the orthorhombic structure found in materials in the $A_2M_3O_{12}$ family, such as $Al_2W_3O_{12}$, as shown in Figure 7.

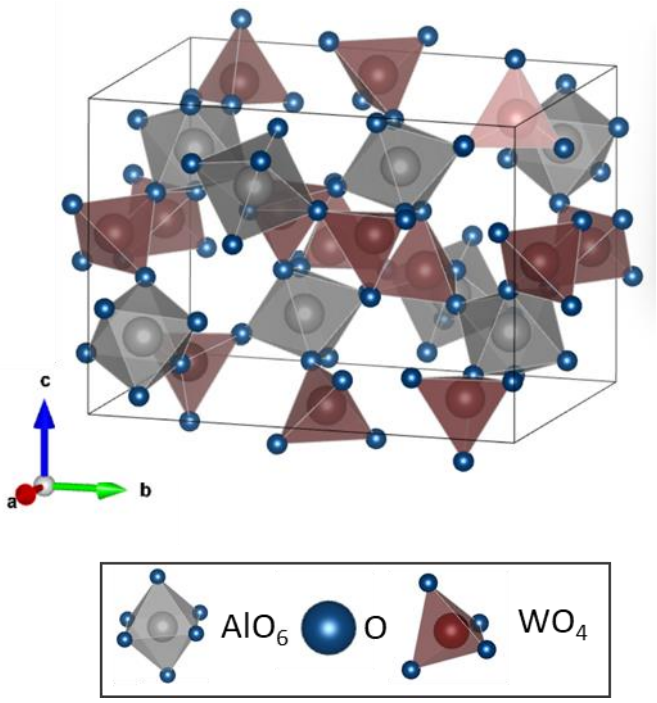

Figure 7: Orthorhombic crystal structure of $Al_2W_3O_{12}$ belonging to the $A_2M_3O_{12}$ family of ceramic [41].

2.6.1 $A_2M_3O_{12}$–based electrodes

The structure of $A_2M_3O_{12}$ includes inflexible polyhedra, which possess vast structural gaps that could conceivably accommodate Li-ions with minimum strain during the insertion/extraction of the ions [7,10,11]. This might be a relevant feature for $A_2M_3O_{12}$ ceramics to become candidates for electrodes in LIBs.

For instance, the performance of $Cr_2Mo_3O_{12}$ as an electrode in LIBs was investigated in 2015 by Guo et al. [12], making it one of the first ceramics from the $A_2M_3O_{12}$ family to undergo such evaluation. It was observed that the anode exhibited a remarkable reversible capacity of 988 mA h g^{-1} after 50 cycles at a current density of 100 mA g^{-1}.

Mittal et al. [9] studied the behavior of $Y_2W_3O_{12}$ as a new electrode material in LIBs, considering its low toxicity and cost. The ceramic was synthesized via a solid-state route, resulting in single phase. Nonetheless, the electrodes produced from $Y_2W_3O_{12}$ powder exhibit inadequate capacity, which could be attributed to its inherently low conductivity and the resulting reduction in conduction pathways during cycling.

Some research evaluated how the M cation from the $A_2M_3O_{12}$ ceramic family affects the ion storage properties of lithium, sodium, and potassium ions. For example, Liu et al. [10] synthesized and evaluated the ceramic $Sc_2W_xMo_{3-x}O_{12}$ ($0 \leq x \leq 3$). The authors concluded that $Sc_2W_xMo_{3-x}O_{12}$ was not a good candidate as a cathode in sodium and potassium ion-based batteries. However, the ceramic evaluated by Liu et al. presented itself as a potential candidate for lithium-ion-based batteries. Additionally, the research concluded that the species $Sc_2Mo_3O_{12}$ was a better candidate than the species $Sc_2W_3O_{12}$ because $Sc_2Mo_3O_{12}$ has a reversible capacity of approximately 150 mA h g^{-1} after 100 cycles compared to a reversible capacity of approximately 100 mA h g^{-1} after 100 cycles for the species $Sc_2W_3O_{12}$.

On the other hand, Schulz et al. [11] found that the electrode based on $Al_2W_{3-x}Mo_xO_{12}$ ceramic ($0 \leq x \leq 3$) experienced amorphization due to the insertion and deinsertion of lithium ions. A noteworthy observation was that increasing the W content led to a decrease in electrode capacity. As a result, they concluded that the $Al_2Mo_3O_{12}$ ceramic is a promising candidate for use as a active material in LIBs because its electrochemical cell performance falls within the expected range (136 mA h g^{-1}).

Given the versatility of the $A_2M_3O_{12}$ family, the research field is extensive. As far as the author is aware, there is only one study on the $Al_2W_3O_{12}$ material as a possible active material for LIB, which was carried out by Schulz et al. [11]. However, their research was conducted without attempting to improve the efficiency of this ceramic as an electrode, as the objective of this study was solely to evaluate the

change in electrochemical properties by altering the stoichiometry of the metal W and Mo.

2.7 $Al_2W_3O_{12}$: A short overview

$Al_2W_3O_{12}$ pertains to the $A_2M_3O_{12}$ family [82] and are composed from WO_4 and AO_6 polyhedra interconnected through oxygen linkers forming *A*-O-W bridges. At room temperature, $Al_2W_3O_{12}$ exhibits the orthorhombic *Pbcn* (*Pnca)* space group [41,81]. Thanks to its structural characteristics, $Al_2W_3O_{12}$ meets the conditions of NZTE behavior and possesses sufficient space to accommodate lithium ions, resulting in a theoretical capacity of 202 mA h g^{-1} [11,77].

One of the potential application of $Al_2W_3O_{12}$ was documented by Mirsadeghi et al. [83]. They synthesized 40 nm nanoparticles of $Al_2W_3O_{12}$ for photocatalytic purposes for the reduction of imatinib mesylate, an anticancer drug. The researchers demonstrated that $Al_2W_3O_{12}$ nanoparticles effectively degraded this drug under UV light irradiation.

Nevertheless, due to its thermal properties and simple chemistry, $Al_2W_3O_{12}$ proves to be a compelling material in operations where severe temperature gradients are the issue. For instance, $Al_2W_3O_{12}$ exhibits potential as a replacement for sapphire in infrared windows requiring resistance to thermal shock [15]. Additionally, it is noteworthy that the high coefficient of thermal expansion (CTE) of thermoplastics imposes limitations on their utilization in industries such as aerospace and microelectronics. Therefore, $Al_2W_3O_{12}$ can serve as a filler in thermoplastic matrices to mitigate their CTE [84].

2.7.1 Defects in $Al_2W_3O_{12}$

Several studies have demonstrated the ability to alter the properties of $Al_2W_3O_{12}$ by modifying its structure and composition. Costa et al. [85] conducted a study in which Al^{3+} was substituted for Ga^{3+} in $Al_2W_3O_{12}$ to investigate the effects on thermal shock properties. However, due to the limited solid solubility of Ga^{3+} in $Al_{2-x}Ga_xW_3O_{12}$, it was not possible to form a phase with NZTE. As a result, $Al_{2-x}Ga_xW_3O_{12}$ is not considered a suitable candidate for thermal shock resistance. Similarly, Ceron et al. [86] examined the substitution defects in $Al_{2-x}In_xW_3O_{12}$

ceramics and found that they do not lead to the formation of materials with thermal expansion close to zero.

In other research by Li et al. [87], $Al_{2-2x}(ZrMg)_xW_3O_{12}$ was synthesized to lower the phase transition temperature of $Al_2W_3O_{12}$. The inclusion of $(ZrMg)^{6+}$ into the crystal lattice of $Al_2W_3O_{12}$ decreases orthorhombic-to-monoclinic phase transition temperature.

Dasgupta et al. [88] studied optical properties of $Al_{2-x}Sc_xW_3O_{12}$ as a potential candidate for infrared transmission window materials with low thermal expansion. They achieved a high transmittance index in the infrared spectrum and observed a low thermal expansion within the 25 - 700 °C temperature range. Yanase et al. [89] investigated the impact of substituting Al^{3+} with B^{3+} in $Al_2W_3O_{12}$ and observed that the metal doping led to a modification of the material's color.

Recently, Moreno et al. [41] investigated the effect of oxygen vacancies (OV) on the optical and thermal properties of $Al_2W_3O_{12}$. Their study examined and compared the formation of oxygen vacancies in the structure of $Al_2W_3O_{12}$ under the influence of reducing in inert atmospheres. They found that samples subjected to reducing atmospheres at 400°C for 2 h exhibited the highest concentration of oxygen vacancies, resulting in an expansion of the crystal lattice. This expansion of the crystal lattice is a direct result of the formation of oxygen vacancies.

However, until now and despite their impact on the physical properties, the investigation of OV, or the addition of carbon in $Al_2W_3O_{12}$ as an active material has not been conducted, as far as the author is aware.

2.8 Point defects in ceramics

A diverse range of defects existing in ceramics can be classified according to their dimensionality, namely 0D, 1D, 2D, and 3D. Table 4 presents the classification of crystal defects based on their dimensionality.

Table 2: Classification of crystalline defects according to their dimensions [90]**.**

Dimensional	Type of defect
0-dimensional (0D)	Point defects (vacancies, interstitials, substitutional defects)

1-dimensional (1D)	Dislocations
2-dimensional (2D)	Stacking faults, twins, grain and phase boundaries, surface
3-dimensional (3D)	Precipitates, inclusions voids, dislocation clusters

Point defects in ceramics represent a deviation in the periodicity of the crystal lattice and these are considered in classification as 0D defects [90,91]. These defects manifest as vacancies, where atoms are missing from their regular positions in the crystal lattice, interstitials, which are additional atoms occupying originally empty spaces between lattice sites, or substitutional defects, where original atomic species are replaced by other chemical species [92].

When an atom is displaced from its original position within the crystal structure and occupies an interstitial site in the same crystal structure, a cationic or anionic vacancy is generated, classified as a Frenkel defect or anti-Frenkel respectively. In adition, when both anionic and cationic vacancies are simultaneously formed in ionic ceramics, it is referred to as a Schottky defect [91,93,94]. A schematic representation of point defects is shown in Figure 8.

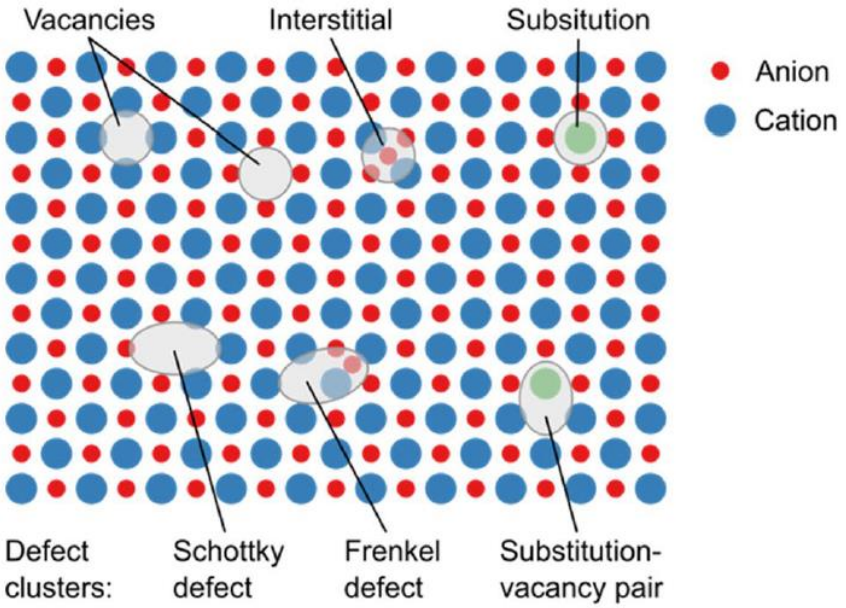

Figure 8: Schematic representation of point defects in a crystal lattice [92]**.**

2.8.1 Charge compensation

In accordance with Pauling's second rule, the total charges of the cations in a crystal structure must equal the charge of the anions. If the second rule of Pauling is not satisfied, the crystal would lose its charge neutrality. Thus, charge compensation mechanisms are present in order to maintain the charge balance within the crystal.

As an example, in the case of OV in WO_3, ionic charge compensation occurs through the valence change of W^{6+} to either W^{5+} or W^{4+} [95,96]. Wang et al. [97] generated OV in WO_3 and confirmed their presence by X-ray photoelectron spectroscopy (XPS) through the reduction of W^{6+} to W^{5+}.

Another interesting relevant example for this doctoral project is taken from the research of Moreno et al. [41]. They confirmed that the ionic charge compensation, resulting from the formation of OV in $Al_2W_3O_{12}$ corresponds to the change from W^{6+} to W^{5+}. These authors also determined the presence of W^{5+} by XPS.

2.8.2 Kröger-Vink notation

A methodology to denote the type of charge compensation due to the presence of defects within the crystal structure is through the utilization of Kröger-Vink notation. It helps to describe and understand defects in ceramics. In Kröger-Vink notation, the atom or vacancy (S), the crystal site ($_p$), and the effective charge (^{C}) are considered. The effective charge can be represented as negative ($^/$), positive ($^\bullet$), or neutral (^{x}) and this is calculated by summing the charges of each ion present in the crystal. The overall structure can be described as follows:

$$S_p^c$$

The presence of anionic and cationic vacancies can be described using Kröger-Vink notation. In the case of an anionic vacancy (for instance, OV), it can be represented in Kröger-Vink notation as shown in Equation 4.

Equation 4: Kröger-Vink notation for the formation of an ionized oxygen vacancy.

$$O_o^x \rightarrow \frac{1}{2} O_2(g) + V_o^{\bullet\bullet} + 2e^{'}$$

On the left side of equation 4 in the perfect lattice, it can be observed that oxygen has a neutral charge, and according to the Kröger-Vink notation this is written as O_o^x. On the other hand, on the right side of this equation, representing defective lattice, the formation of an OV is expressed as $V_o^{\bullet\bullet}$, and to maintain charge neutrality, 2 electrons (2e´) are added to the expression. Finally, to maintain mass balance, it can be observed that oxygen is released in the gaseous state.

Finally, Kröger-Vink notation can be used to write Schottky defect formation from a perfect crystal (null) of $Al_2W_3O_{12}$ as shown in Equation 5.

Equation 5: Kröger-Vink notation for Schottky defect in $Al_2W_3O_{12}$.

$$null \rightarrow 2V_{Al}^{'''} + 3V_W^{''''''} + 12\, V_o^{\bullet\bullet}$$

2.9 Ionic vacancies

Equation 6 mathematically demonstrates the influence of temperature on the vacancy formation process. According to statistical thermodynamics, the number of vacancies *(ns)* can be estimated using this equation, where *N* represents the site density, ΔE_f is the energy required for vacancy formation, k is the Boltzmann constant, and *T* denotes the temperature. It is noteworthy that the term $\exp(-\Delta E_f/2kT)$ represents the probability of Schottky pair formation [98].

Equation 6: Relation between the number of Schottky pairs, their energy of formation and temperature

$$n_s = N \exp\left(\frac{-\Delta E_f}{2kT}\right)$$

Based on the type of missing ion at specific lattice sites, the vacancy defect can be categorized into two types: anion vacancies and cation vacancies. The presence of vacancies can significantly modify the characteristics of a material [91].

The vacancies deeply impact various physical properties, making them relevant in diverse applications such as catalytic, optical, conduction, fuel cells, batteries, sensitive solar cells, water treatment, energy storage, and resistive devices [91,98–100]. For example, OV were created in Bi_2WO_6 to enhance its photocatalytic properties. The improvement in its optical properties is attributed to the electrons trapped by the OV [101].

2.9.1 Anion vacancy and its influence on the active materials

Anionic vacancies can be obtained through calcination in vacuum or in inert and/or reducing atmospheres composed of nitrogen, argon, hydrogen, or their combinations. Hydrogen is commonly employed in this technique [102].

When OV is present within the electrode structure, it can enhance the diffusion of Li-ions, decrease the resistance to charge transfer, and improve LIB's capacity and rate performance [35]. OV offers a highly effective means to finely adjust the electronic structure, charge capacity, electrical conductivity, cation diffusion, surface structure, and stability of cathode materials. As a result, it significantly contributes to LIB's longevity and overall performance [29,103].

With the introduction of OV in the active material, the electronic structure of the metal oxide can be modified, resulting in improved electrical conductivity and reduced ion diffusion barrier [104]. Furthermore, the formation of OV leads to new active sites that can be utilized for ion storage, resulting in enhanced efficiency. Lastly, ion transfer can be facilitated since the presence of OV may lead to an imbalanced charge distribution and the formation of an electric field [35].

The influence of OV has been tested in other types of ionic batteries. OV in the structure of the electrode is beneficial for Sodium-ion batteries (SIB) according to Xu et al. [105]. They demonstrated that the presence of OV in the MoO_3 electrode in SIB increases the electric conductivity and Na-ion diffusion coefficient. In addition, Bia et al. [106] used core-shell anatase TiO_2 spheres with abundant oxygen vacancies and a surface coating of nitrogen-doped carbon as an electrode in SIB. They demonstrated the impact of OV on the storage properties of SIB. Zhang et al. [107] studied the electrode based on $Na_2Ti_3O_7$ with OV showing superior electrochemical performance against the same anode without OV in SIB.

Shin et al. [32] studied the influence of OVs on the alternative electrode of LIBs based on TiO_{2-x}. In their research, they successfully enhanced the electrical conductivity of the electrode by incorporating OVs. Regarding traditional cathodes of LIBs, Sun et al. [108] introduced OVs in Li_2MnO_{3-x} and observed an increase in capacity and improved cycling performance. The Li_xCoO_2 cathode improvement in electrical conductivity and ion conduction, was attributed to the presence of OVs [109].

As demonstrated in this section of the document, OV has been shown to enhance the electrical properties of anodes and cathodes in ionic batteries. Therefore, one can hypothesize that OV inside $Al_2W_3O_{12}$ would be a suitable pathway to improve its efficiency as a novel active material in LIB.

2.10 Influence of carbon content on the electrodes

Carbonaceous materials have a rich background as an additive to electrode materials across various battery technologies owing to their exceptional chemical stability, electrical conductivity, substantially high specific surface area, and distinctive porosity [110]. Thus, one pathway to improve the electrical properties of the active materials (anode and cathode) is through surface treatment using carbon content that modifies the inherent characteristics of this material.

As the carbon source is often used citric acid, glucose, or sucrose [110]. In most cases, the carbon content is added after the synthesis of the active phase [111].

Wu et al. [112] improved the capacity of the $LiCoPO_4$ cathode by adding carbon content onto the material's surface. The discharge capacity of the carbon-free cathode increased from 83.3 mAh g^{-1} to 120.3 mAh g^{-1} with the addition of carbon, thus demonstrating the influence of carbon on the cathode.

Studies on carbon content have also been conducted on certain members of the $A_2M_3O_{12}$ ceramic family. For instance, $Y_2W_3O_{12}$ was synthesized *via* the solid-state route and subsequently carbon-coated. The carbon-coated $Y_2W_3O_{12}$ demonstrated excellent rate performance and long-term cycling stability, keeping a high capacity of 140 mA h g^{-1} after 2000 cycles [9].

3
Objectives

3.1
General Objective

Study the impact of OV, and carbon addition on the electrochemical performance and structural and microstructural properties of $Al_2W_3O_{12}$-based ceramic as an active material in LIB, to understand their influences on lithium ion capacity, cycling stability, and overall efficiency.

3.2
Specific objectives

1. Study of the conditions to produce OV, and add carbon to $Al_2W_3O_{12}$ active phase.
2. Study of the conditions and formation of OV through thermal excitation under reducing atmospheres in $Al_2W_3O_{12}$.
3. Study of different methods and conditions for the addition of carbon to $Al_2W_3O_{12}$.
4. Characterization of the as-formed materials to determine the presence of OV, and carbon content in $Al_2W_3O_{12}$.
5. Study of electrochemical properties of $Al_2W_3O_{12}$-based electrode in LIBs.

4
Materials and methods

4.1
Materials

$Al(NO_3)_3\ 9H_2O$ (Alfa Aesar, purity≥ 99%) and $Na_2WO_4\ 2H_2O$ (Sigma-Aldrich, purity ≥ 99%) were used as reagents in the co-precipitation method to synthesize $Al_2W_3O_{12}$. To coat the $Al_2W_3O_{12}$ powder with carbon, sucrose (Anedra) and graphite (Sigma-Aldrich, purity ≥ 95%) were used.

4.2
Synthesis of $Al_2W_3O_{12}$

$Al(NO_3)_3\ 9H_2O$ and $Na_2WO_4\ 2H_2O$ were used as reagents in the co-precipitation method to synthesize $Al_2W_3O_{12}$. Initially, 0.1 M solutions of each reagent were mixed at room temperature to form a white amorphous precipitate precursor for $Al_2W_3O_{12}$. Specifically, 150 mL of 0.1 M $Na_2WO_4\ 2H_2O$ solution and 100 mL of 0.1 M $Al(NO_3)_3\ 9H_2O$ solution were mixed. This precipitate was then centrifuged at 4000 rpm for 6 min, washed with anhydrous ethanol, and dried overnight at 80 °C in a conventional oven. The as-dried amorphous powder was ground in an agate mortar and calcined in air at 800 ºC for 10 h in a horizontal tube furnace (Maitec-NTI FET 1600/H, São Carlos, Brazil) for crystallization. The resulting crystalline white powder was labeled as S800. The co-precipitation process is described schematically in Figure 9.

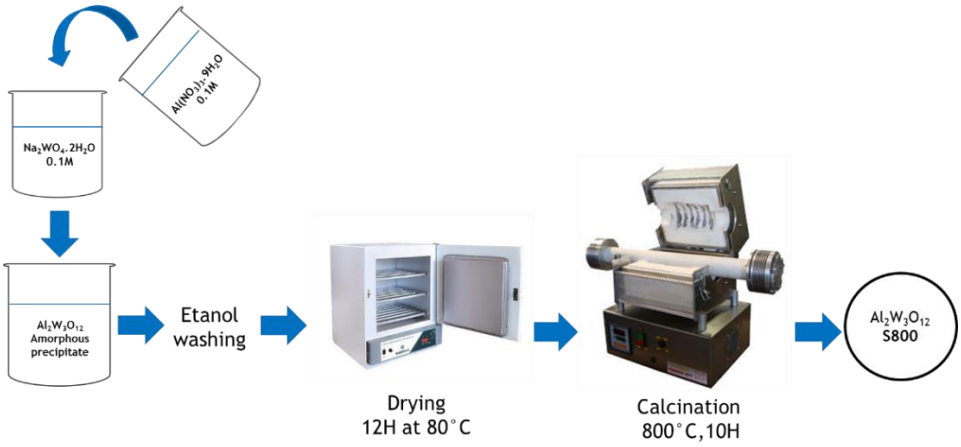

Figure 9: Schematic representation of the synthesis of $Al_2W_3O_{12}$ through co-precipitation by mixing reactants.

4.3 Synthesis of $Al_2W_3O_{12}$ with OV

To investigate the impact of OV on the electrochemical performance of $Al_2W_3O_{12}$, the S800 sample was calcined in pure hydrogen (Linde, 99.9%) at 400°C for 2 h, resulting in a dark gray powder, denoted SH400.

4.4 Synthesis of $Al_2W_3O_{12}$ with carbon

To coat the S800 powder with carbon, two independent post-synthesis treatments were undertaken. In the first one, the sample was mixed with graphite (Sigma-Aldrich, purity ≥ 95%) at a weight ratio of 3:5 (S800:graphite) by high-energy mechanical milling in a planetary ball mill (Fritsch Pulverisette 7-Premium line). The mixture (1.5 g) was processed in a mill cylinder containing three stainless steel balls with diameters of 6 mm (2.64 g). The milling process was conducted under an argon atmosphere (purity ≥ 99.99%) at 300 rpm for 30 min with intervals every 10 min. The final black powder was labeled S800G(3:5).

For the second post-synthesis approach, 1 g of the S800 sample was immersed in a solution containing 1.5 g of sucrose (Anedra), 5.77 mL of deionized water, and 0.126 mL of sulfuric acid (Anedra, purity ≥ 96%). The solution was stirred for 2 h at room temperature and then dried in an oven at 80 °C until liquid was completely removed. Finally, the as-obtained solid was calcined in a tubular oven at 700 °C for

5 h (heating rate of 2 °C min^{-1}) with a flow of argon gas. The resulting black powder was named SC700.

4.5 Battery assemblage

The electrodes were prepared by mixing the active material (S800, SH400, SC700, or S800G(3:5)), Carbon Super P (Timcal Graphite), and polyvinylidene difluoride (Sigma-Aldrich) in an 80:10:10 ratio, respectively. Then, a small amount of N-Methyl-2-Pyrrolidone (Sigma-Aldrich) was added as a solvent and mixed in a planetary ball mill at 300 rpm for 10 min until obtaining a homogeneous final slurry. These slurries were, then, coated onto a copper foil using the doctor blade method (150 μm), and dried for 4 h at 80 °C in a vacuum oven. Subsequently, the copper foil was cut into electrodes with a diameter of 12 mm with the loadings of active material of around 4 mg cm^{-1}.

CR2032 Coin cells assembly were undertaken in an argon-filled glove box. Lithium metal (Alfa Aesar, purity ≥ 99.9%) was utilized as the counter and reference electrode, while Whatman GF/F (CYTIVA) served as the separator. The electrolyte consisted of 1.2 M lithium hexafluorophosphate (Alfa Aesar, purity≥ 99%) dissolved in a mixture of ethylene carbonate (Sigma-Aldrich) and dimethyl carbonate (DMC) (Sigma-Aldrich, purity≥ 99%) in a 1:3 ratio.

4.6 Materials characterization

4.6.1 X-ray powder diffraction (XRPD)

The influence of oxygen vacancies, and carbon coating, on the crystal structure will be characterized by XRPD using a D8 Advance diffractometer (Bruker, Germany), using Cu Kα radiation. The diffractograms were analyzed using the Rietveld and Le bail method, with Topas 4.2 software.

Room temperature diffractograms were obtained for S800, SC700, S80G(3:5), and SH400 samples in the range from 10 ° to 80 ° (2 theta) with a step of 0.01 ° (2 *s* per step).

4.6.2
Electronic paramagnetic resonance (EPR)

The presence of oxygen vacancies in the samples were characterized by electronic paramagnetic resonance (EPR). EPR measurements were conducted using a Bruker Elexsys E500 spectrometer operating at the X-band (9.85 GHz) with a high-sensitivity resonant cavity. The experimental setup included a DC magnetic field ranging from 338 to 346 mT, an AC magnetic field at 100 kHz with modulation amplitude of 0.2 mT, and microwave power of 0.5 mW. Each sample underwent fifteen scans, each lasting 60 s. To calibrate the Landé g-factor, a $MgO:Cr^{+3}$ standard sample (g=1.9797) was utilized. EPR simulations were performed using EasySpin package (MATLAB) The experiments were carried out at room temperature using 4 mm quartz tubes, which were suitable for placement inside the resonant cavity.

4.6.3
Raman spectroscopie

The presence and the degree of disorder of the carbon structure were verified by Raman spectroscopy, using a Horiba micro-Raman microscope (XploRA), in the range of 200 to 1800 cm^{-1} at the excitation wavelength of 532 nm.

4.6.4
X-ray excited photoelectron spectroscopy (XPS)

XPS measurements were performed at room temperature using a Thermo Scientific K-Alpha+ spectrometer under a vacuum pressure of 1.0×10^{-6} Pa. Non-monochromatized Al-Kα radiation (1200 W) was used for excitation, and a 180° double-focus hemispherical analyzer with a 200 µm sampling area was employed. Measurements were taken at a normal electron emission angle (take-off angle: 90°). Each sample was mounted in duplicate on copper tape and placed in a dedicated powder sample holder. Survey spectra and tungsten (W 4f) core-level spectra were collected. The pass energy and step energy were set at 100 eV and 0.5 eV, respectively, for survey scans, and at 20 eV and 0.05 eV for W 4f core-level scans. Data analysis was performed using Avantage™ V5 and Igor PRO 6 (WaveMetrics) software, with spectral deconvolution based on Voigt functions. Binding energy

calibration was referenced to graphitic carbon at 284.4 eV, from which W 4f binding energies were determined. To mitigate the effects of conductivity variations in the samples, charge compensation was applied using a flood gun supplying both ions and electrons.

4.6.5 Thermogravimetric analysis (TGA)

Thermogravimetric analysis (TGA) was carried out on STA 449 F3 Jupiter, (Netzsch, Germany) at a heating rate of 10 ºC min^{-1} from 40 to 1000 ºC in air to measure the percentage of carbon in the samples.

4.6.6 Scanning electron microscopy (SEM)

The morphology of the electrode was assessed using SEM, the HITASHI TM-3000 equipment was used, which works at 15 kV. For *ex-situ* measurements after cycling, the electrodes were extracted from the coin cells inside the glovebox, washed with DMC, and dried.

4.6.7 Scanning transmission electron microscopy (STEM), energy dispersive X-ray spectroscopy (EDS)

STEM images and EDS mapping images was collected using ThermoFisher Talos F200X G2, operating at 200 kV. For sample preparation, a small quantity of each of the powders (S800, SC700, and S800G(3:5)) was dispersed in isopropyl alcohol using ultrasonic treatment for 30 min, and then deposited onto a holey carbon film mounted on a copper grid.

4.6.8 Low-temperature nitrogen adsorption/desorption

In order to explore the textural features of the synthesized samples, low-temperature nitrogen adsorption/desorption technique was employed (Quantachrome, NOVAtouch LX2).

4.7
Electrochemical measurements

The electrochemical measurements, such as galvanostatic charge-discharge cycles (GCD) and rate capability (RC) experiments, were carried out in Arbin Instruments (Model BT 2043). GCD were performed using a voltage range of 0.01 V to 3 V for 100 cycles at a current density of 20 mA g^{-1}. RC experiments were conducted at different current densities. Cyclic voltammetry (CV) of $Al_2W_3O_{12}$ electrodes were measured using different scan rates from 0.1 mV s^{-1} to 1 mV s^{-1} in a voltage range of 0.01-3 V in Gamry Potentiostat-Galvanostat. All tests were performed at room temperature.

5
Results and Discussion

5.1
Effect of carbon in $Al_2W_3O_{12}$ based electrodes

5.1.1
Structural characterization before cycling

5.1.1.1
XRPD patterns

Figure 10 presents the XRPD patterns of the S800, SC700, and S800G(3:5) samples. The sharp and intense diffraction lines correspond, in all three samples, to the orthorhombic phase with the space group *Pbcn*, the stable one for $Al_2W_3O_{12}$ at room temperature, in agreement with previous reports [14,41,81]. Therefore, the post-synthesis carbon-coating procedures had not affected $Al_2W_3O_{12}$ crystal structure. Besides, diffraction lines located at 14.05º (a prominent one) and 32.56º (2θ), which can be attributed to WO_3 [113,114] and/or WO_{3-x} [115] phases, were identified in the S800 sample.

In contrast to the white color S800 sample (Figure S1A), the black color SC700 powder (Figure S1B) shows additional diffraction lines situated at 14.33º, 19.47°, 27.16º, and 33.26° (2θ). The diffraction lines at 19.47º and 27.16º (2θ) might be associated with some of the carbon-rich phases [116,117]. Furthermore, the two additional diffraction lines at 14.33º and 33.26º (2θ) can be attributed to WS_2, in the hexagonal space group R3m [118]**.** The presence of hexagonal WS_2 resulted from the post-synthesis treatment with sucrose, used for preparation of the SC700 sample. As such, the sulfuric acid used in the post-synthesis may react with the WO_3 or WO_{3-x} phases, leading to the formation of the WS_2 phase, as reported by other authors [119].

In Figure 10, the 26.59° (2θ) diffraction line in the black color S800G(3:5) sample (Figure S1C) is attributed to graphite [120]. The representative diffraction lines of orthorhombic $Al_2W_3O_{12}$ show a significant attenuation in the S800G(3:5)

sample. This could occur due to the strong preferential orientation of (0002) crystallographic plane of the graphite phase.

The average crystallite size of orthorhombic $Al_2W_3O_{12}$ in S800 sample was estimated at 530 nm through Rietveld method. The diffraction pattern of the orthorhombic $Al_2W_3O_{12}$ of sample S800 refined by Rietveld method for orthorhombic $Al_2W_3O_{12}$ is presented in Figure S2A.

In addition, diffraction pattern of S800G(3:5) has been adjusted by LeBail method for the orthorhombic $Al_2W_3O_{12}$, while peak phase approach has been used for graphite to estimate mean crystallite size of graphite along c-direction (Figure S2B), since the dominant diffraction line of graphite, at 26.59° (2θ) is (0002). As expected the mean crystallite size along c-direction was much lower (0.57 μm) when compared to the mean lateral dimensions, estimated by SEM at 15 μm (Figure S3). On the other hand, the average crystallite size of orthorhombic $Al_2W_3O_{12}$ was almost identical (560 nm) to the one measured for S800, showing that ball milling did not affect mean crystallite size of this phase, but possibly only their deagglomeration.

The presence, and percentage, of carbon in the SC700 and S800G(3:5) samples were also confirmed and estimated through TGA (Figure S4). In the S800G(3:5) sample, a loss of 64 wt.% was recorded between 550 and 860 °C. In comparison, the SC700 sample exhibited a loss of 34 wt.% between 500 and 600 °C. The difference in the temperature ranges related to carbon loss confirms that the two samples possess different carbon-rich phases, which is consistent with the XRPD analysis [121,122].

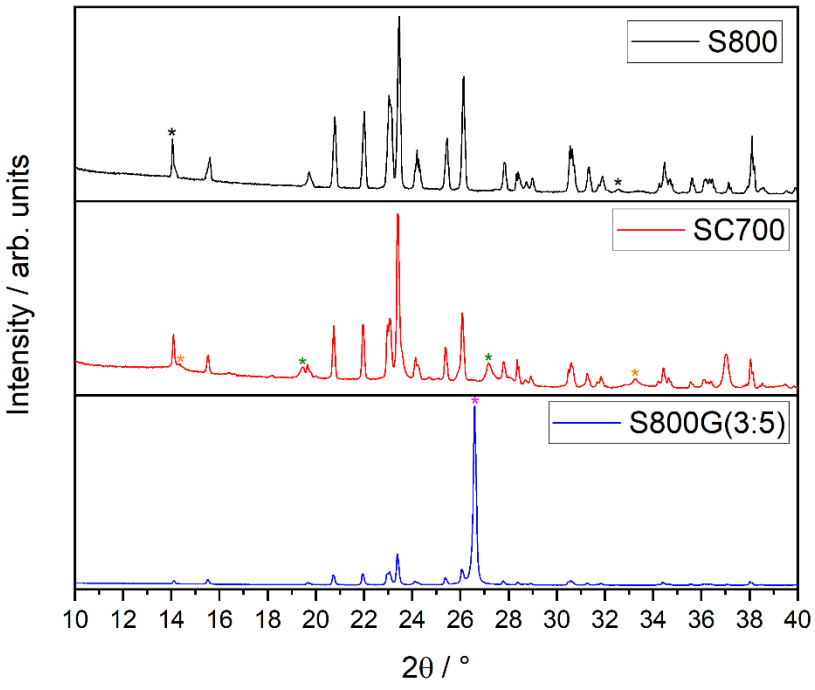

Figure 10: The XRPD patterns of the S800, SC700, and S800G(3:5) samples. *,*,*, and * stand for diffraction lines of carbon-rich phases, hexagonal WS_2, monoclinic and hexagonal polymorph WO_3 or WO_{3-x}, and graphite, respectively.

5.1.1.2 STEM images and EDS mapping

STEM images and EDS mapping of the S800, SC700, and S800G(3:5) samples are exhibited in Figure 11. Figures 11A and 11E illustrate agglomeration of $Al_2W_3O_{12}$ particles in the S800 and SC700 samples, respectively. Figure 11K presents graphite sheets together with deagglomerated $Al_2W_3O_{12}$ particles. This latter suggests that the post-synthesis treatment, high-energy milling, applied for preparation of S800G(3:5) sample caused particle deagglomeration. S800 sample has been used as a reference to distinguish between the type of carbon addition (mixture or coating) into other two materials (SC700, and S800G(3:5)).

The presence of O (Figure 11B, F and L), Al (Figure 11C, G and M), and W (Figure 11D, H and O), corresponding to $Al_2W_3O_{12}$ phase, was confirmed in all three samples using EDS mapping. In addition, sulfur was identified only in the

SC700 sample (Figure 11J), localized to a few regions which correspond to WS_2 particles, in accordance with XRPD analysis (Figure 1).

Figures 11I and 11O demonstrate the presence of carbon phases in the SC700 and S800G(3:5) samples, respectively. EDS mapping of carbon in SC700 sample (Figure 11I), illustrates that it is localized over several regions of $Al_2W_3O_{12}$ agglomerate, suggesting that carbon coating over $Al_2W_3O_{12}$ agglomerate is not completely homogeneous. In contrast, EDS mapping of the S800G(3:5) (Figure 11O), confirmed that carbon signal is not associated to $Al_2W_3O_{12}$ particles (Figure 11K) but principally to graphite sheets, strongly indicating a mixing of $Al_2W_3O_{12}$ and graphite.

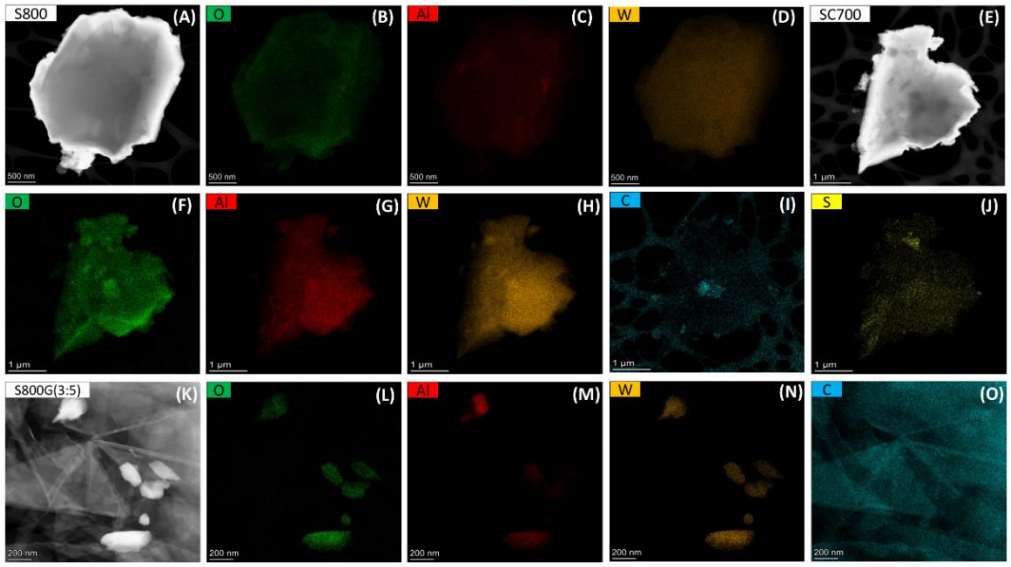

Figure 11: STEM images of S800 (A), SC700 (E), and S800G(3:5) (K); EDS mapping images of S800 (B-D), SC700 (F-J), and S800G(3:5) (L-O).

5.1.1.3 Raman spectra

Raman spectra of the S800, SC700, and S800G(3:5) samples are shown in Figure 12. The existence of carbon phases in the SC700 and S800G(3:5) samples has been corroborated by Raman spectra. Both samples exhibit the characteristic graphite-like D- and G-bands. The D-band corresponds to structural disorder (bond-angle disorder, bond-length disorder) of carbon phases and has a lower wavenumber than the G-band, this one associated with the stretching vibrations of

C-C in the basal plane of crystalline graphite [123]. The S800G(3:5) material shows two narrow bands centered at 1335 and 1570 cm^{-1}, while the SC700 sample exhibits broad peaks centered at 1344 and 1581 cm^{-1} (Figure 12).

The ratio between the intensities of the two bands (I_D/I_G) is used to quantify the degree of perfect, imperfect, and disordered structures of a carbon material [124,125]. For comparison, the Raman spectrum of pristine graphite (Figure S5) was acquired, resulting in an I_D/I_G ratio of 0.13.

According to the Raman spectra (Figure 12), the I_D/I_G ratio for the S800G(3:5) and SC700 samples is 0.153 and 0.787, respectively. These ratios suggest a much higher degree of an order carbon phase (graphite) in the S800G(3:5) sample, compared with the samples SC700, in accordance to XRPD patterns (Figures 10) from which the presence of crystalline graphite phase is only evidenced in S800G(3:5). In contrast, the SC700 sample shows a much higher disorder of carbon material presented in the coating. The prominent differences in I_D/I_G ratio in S800G(3:5) and SC700 samples corroborate the presence of different carbon phases in the two samples, in agreement with XPRD findings (Figure 10). In addition, as expected, the S800 material does not exhibit the characteristic signals of the carbon D- or G-bands (Figure 12).

In Figure 12, the vibration modes of $Al_2W_3O_{12}$ can be identified for the S800 and SC700 samples. Bands in the range 900-1050 cm^{-1} belong to symmetric stretching vibration of W-O in WO_4; those in the range 700-900 cm^{-1} were assigned to an asymmetric stretching vibration of W-O in WO_4; the bands in the 300-500 cm^{-1} range belong to bending vibrations of O-W-O in WO_4, and those below 300 cm^{-1} was assigned to lattice vibrations of WO_4 [89,126]. In the SC700 sample, additional bands were identified between 340 and 420 cm^{-1}. These may correspond to the vibration modes of WS_2 [127], in accordance to the XRPD analysis (Figure 10). For S800G(3:5) sample, the signals corresponding to $Al_2W_3O_{12}$ are strongly attenuated, as it occurred in XRPD pattern (Figure 10), due to the higher concentration of graphite in this sample.

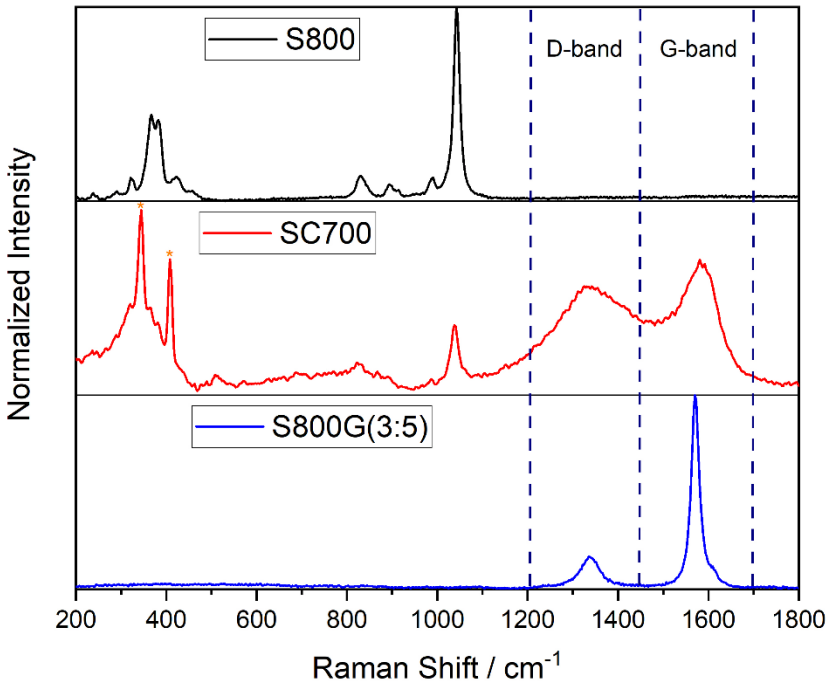

Figure 12: Raman spectra of the S800, SC700, and S800G(3:5) samples within 200-1800 cm^{-1} region. D and G-bands of carbon phases are indicated in the Figure. * stands for bands of WS_2.

5.1.1.4 XPS measurements

XPS measurements were performed to investigate the composition of the S800, SC700, and SG800G(3:5) materials before their assembly into the electrochemical cell. To determine the composition of the different samples, the survey spectra were acquired (Fig. S6), and the presence of oxygen, aluminum, tungsten, and carbon was confirmed. Sulphur is additionally identified in SC700 spectrum (Fig. S6). As expected, the carbon content in samples S800G(3:5) and SC700 is higher than in S800, accompanied by a decrease in the relative amounts of the other three elements.

The XPS spectra of the W 4f core level for the three studied samples are shown in Figure 13. The W 4f spectrum of S800 consists of two spin–orbit doublets corresponding to W^{6+} at a binding energy of 35.9 and 38.2 eV for the W $4f_{7/2}$ and W $4f_{5/2}$, respectively [128–130]. It was not possible to corroborate the presence of

additional 4f doublets accounting for reduced W species or oxygen vacancy-related compounds, within the resolution of the equipment and the fitting process, in agreement to a few other reports [41,42,131]. In addition, a small doublet corresponding to the W 5p core level of W^{+6} centered at 39.9 (W $5p_{3/2}$) and 41.5 eV (W $5p_{1/2}$) was identified. This strongly suggests that the S800 ceramic contains only W^{6+} species.

The same analysis was performed for S800G(3:5). As expected, no new features were observed, which means that only one W 4f doublet was found, corresponding to W^{6+} species, along with the W 5p doublet. However, despite these similarities, it was found that the fitting process for S800G(3:5) spectrum could not accommodate the same fitting parameters as-used for the S800 sample. Instead, a slightly broader pair of peaks were required (full width at the half maximum - FWHM of 1.71 eV for S800 and 1.95 eV for S800G(3:5)). While this effect cannot be attributed to the presence of new species, such as reduced W species or oxygen vacancies, it is likely a consequence of a different chemical environment, rich in carbon, coating $Al_2W_3O_{12}$ phase in S800G(3:5), leading to an increase in the FWHM of the peaks.

Figure 13 presents also the W 4f XPS spectrum of the SC700 sample. Contrary to the other two spectra (S800, and S800G(3:5)), the SC700 spectrum can be deconvoluted into four doublets related to the W 4f level, corresponding to different tungsten valence states. A dominant W^{4+} doublet (W $4f_{7/2}$ binding energy at ~32.61 eV, FWHM ~0.85 eV) is identified, indicative of WS_2, with an estimated S/W atomic ratio of ~4/3 as based on survey spectra (Figure S6). Regarding to tungsten from $Al_2W_3O_{12}$, a W^{6+} doublet (W $4f_{7/2}$ at ~35.9 eV) was identified, along with a minor W^{5+} doublet with $4f_{7/2}$ at ~ 33.7 eV. A weak W^{x+} doublet (W $4f_{7/2}$ at ~31.6 eV) also appears, indicating the presence of sulfur-deficient environments at lower binding energies relative to WS_2, which suggests that W is in a more reduced chemical environment, *i.e.*, with a lower oxidation state than W^{4+} [128,132]. Also, as in the other two materials, a low-intensity doublet, corresponding to the W5p core level of W^{6+}centered at 39.9 eV (W$5p_{3/2}$), was identified.

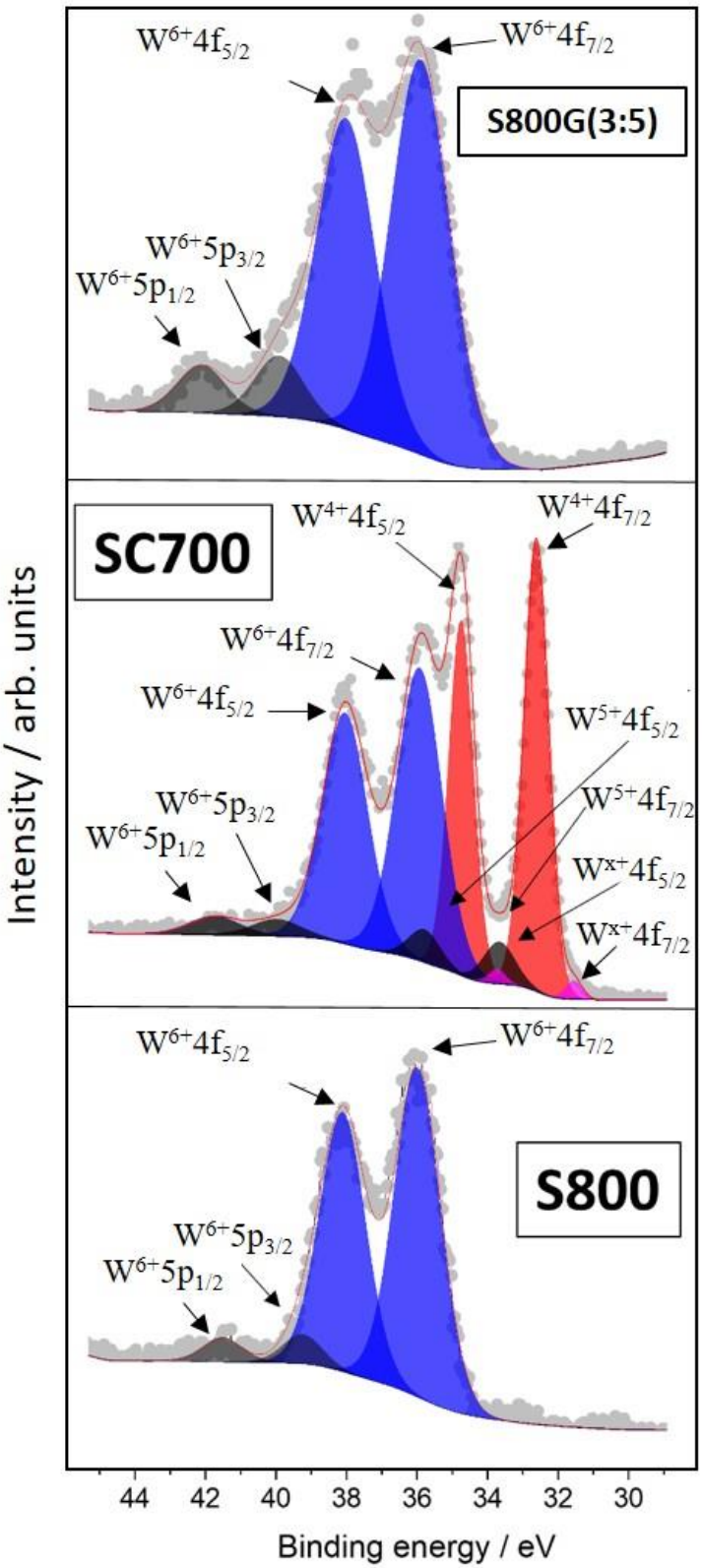

Figure 13: A part of XPS spectra of S800, SC700, and S800G(3:5) samples characteristic for W 4f and W 5p core levels.

5.1.2
Electrochemical performance

5.1.2.1
Galvanostatic charge/discharge

The charge and discharge curves for the 1st, 2nd, 6th, and 8th cycles for S800, SC700, and S800G(3:5) at 20 mA g^{-1} are shown in Figure 14 A, B, and C, respectively. The voltage-capacity profiles for the three samples are very different.

In the S800 and SC700 samples, the characteristic voltage plateau of the lithium-ion intercalation process cannot be identified, in the electrochemical profile [133]. As a matter of fact, the voltage–capacity curves of the S800 sample are similar to those reported in a previous study on $Al_2W_3O_{12}$ synthesized *via* a conventional solid-state route [11]. Therefore, the soft-chemical synthesis route employed here does not appear to affect the electrochemical properties of the $Al_2W_3O_{12}$.

On the other hand, for the S800G(3:5) sample, three plateaus have been identified in both the discharge and charge curves, which is a characteristic of lithium-ion intercalation into the graphite structure present in this sample [134,135]. Therefore, there are no indications, from the charge-discharge curves, of a lithium-ion intercalation process in the $Al_2W_3O_{12}$ open-framework structure. The absence of any plateau in the S800 and SC700 samples and only the plateaus of lithium-ion intercalation into the graphite structure in S800G(3:5) suggests that the charge storage in the $Al_2W_3O_{12}$ ceramic occurred dominantly through some other processes, such as formation of solid solutions, surface-based reactions, or alloying/conversion-type reactions [9,21].

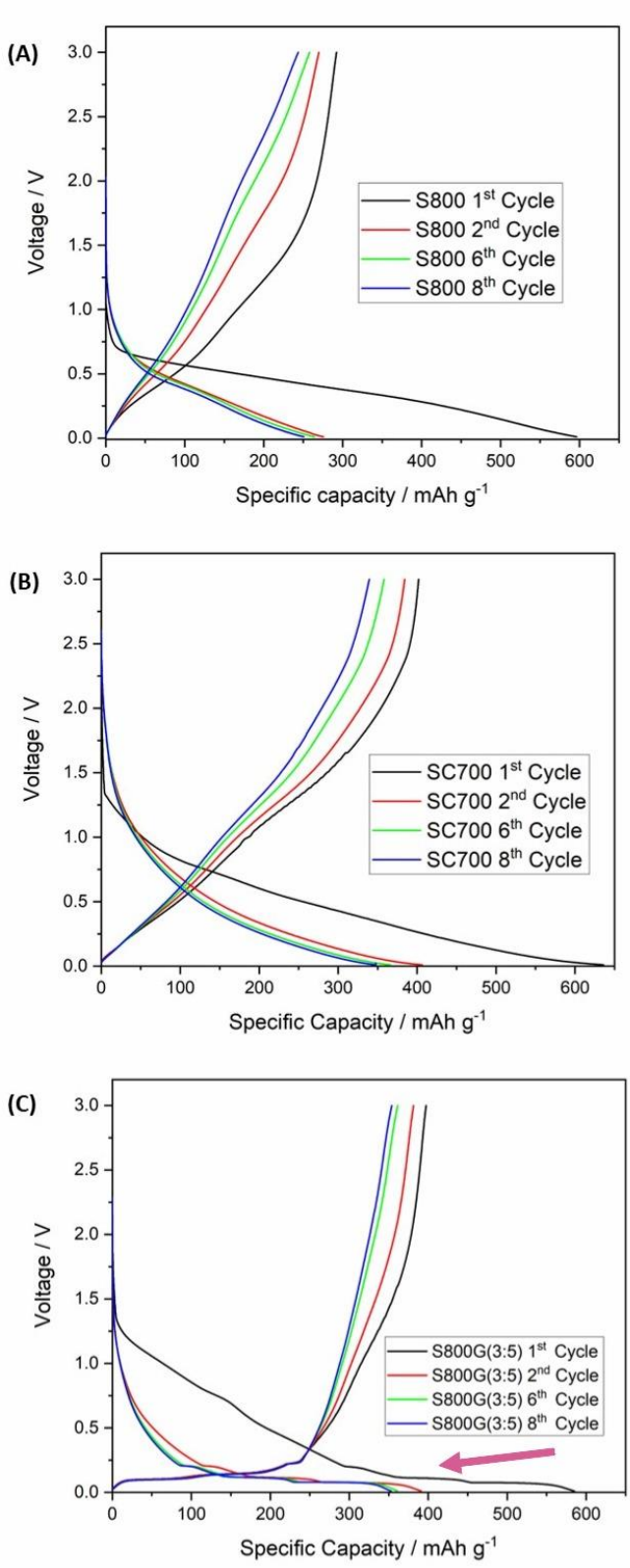

Figure 14: Comparison of galvanostatic charge/discharge (GCD) curves in the 1st, 2nd, 6th, and 8th cycles for S800 (A), SC700 (B), and S800G(3:5) (C) samples. Red arrow shows the plateaus that are characteristic of lithium-ion intercalation in the graphite structure presented in S800G(3:5).

Figure 15 shows the specific capacity between the 1st and 100th cycle at 20 mA g^{-1} for S800, SC700, and S800G(3:5) materials. The first discharges of $Al_2W_3O_{12}$ without carbon (S800 material) against lithium delivered a capacity of 596 mA h g^{-1}, which promptly dropped to below 275 mA h g^{-1}, followed by a continuous drop to around 130 mA h g^{-1} up to the 70th cycle, when stabilized close to this value up to the 100th cycle. The capacity lost after the first discharge process mainly comes from the irreversible consumption of Li^+ in LIBs, caused by electrolyte decomposition and the formation of the solid electrolyte interface (SEI) [136]. From the CE graphs (Figure 15), it is possible to observe an efficiency close to 100% in all cases, except during the first cycle, where the CE was considerably lower, which is directly related to the formation of the SEI.

Notably, the cycling performance of $Al_2W_3O_{12}$ with carbon content (SC700 and S800G(3:5)) improved significantly. The S800G(3:5) and SC700 samples exhibited 34% and 52% capacity drops by the 100th cycle, respectively. However, the mechanical mixture of $Al_2W_3O_{12}$ and graphite reaches 240 mA h g^{-1} at the 44th cycle, maintaining stability throughout the 100th cycle. In contrast, while the SC700 sample initially delivered a higher specific capacity, *i.e.*, 500 mA g^{-1}, its fall was steeper, and reached a specific capacity of 230 mA g^{-1} by the 80th cycle, keeping it stable up to the 100th cycle.

In comparison, silicon-based anodes can reach very high capacities (up to ~ 4200 mA h g^{-1}) [137], SnO_2-based anodes achieve several hundred mA h g^{-1} (e.g., 336 mA h g^{-1} after 50 cycles) [138], and transition metal oxide (TMO) compounds vary widely, with capacities ranging from 200 to over 1000 mA h g^{-1} depending on the specific TMO and carbon modification [139–143]. Therefore, carbon-coated and graphite mixed with $Al_2W_3O_{12}$ offers lower absolute capacity than Si, SnO_2, or many TMOs but provides stable and reproducible cycling.

Furthermore, S800G(3:5) maintains its capacity over 100 cycles, demonstrating good stability. In contrast, Si [144] and SnO_2 [137] anodes experience pronounced volume expansion during cycling, resulting in capacity loss unless strategies such as carbon composites or nanostructuring are applied. TMOs often face pulverization and conductivity limitations, which can also compromise long-term stability [137]. Thus, $Al_2W_3O_{12}$ with graphite exhibits comparatively simple and inherently stable cycling behavior.

Therefore, SC700 and, in particular, S800G(3:5) samples provide a combination of moderate gravimetric capacity, and stable cycle life. While their gravimetric capacities are lower than those of high-capacity materials such as Si, SnO_2, and some TMOs, their excellent stability and simple electrode architecture make them attractive candidates for applications requiring long-term cycling. In addition, volumetric capacities of S800, SC700, and S800G(3:5) have been discussed, which is rather meaningful due to high density of $Al_2W_3O_{12}$ (*vide infra*).

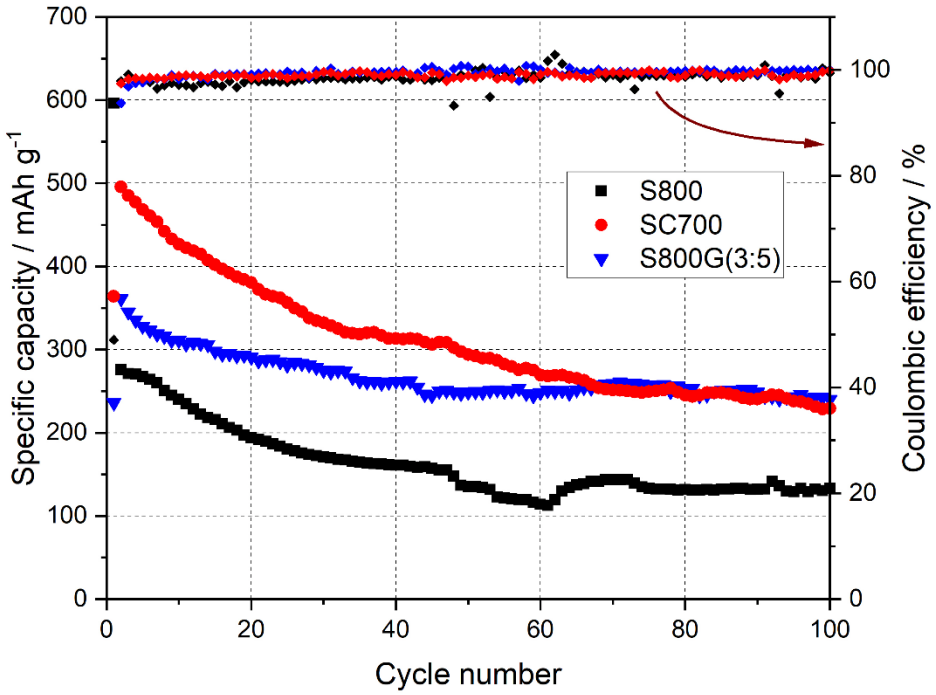

Figure 15: Comparison of the electrochemical performance of cells with S800, SC700, and S800G(3:5) electrodes, cycled between 0.01 and 3.0 V at a constant current density of 20 mA g^{-1}.

5.1.2.2 Cyclic voltammetry (CV)

Figure 16 shows cyclic voltammograms of the three samples at a scan rate from 0.1 to 1 mV s^{-1}. The GCD curves (Figure 14) are consistent with those observed in the CV. The charge and discharge plateaus in the voltage–capacity profiles correspond to the peak positions observed in the CV curves [145]. Therefore,

Figure 16A (S800) shows a very weak peak around 1 V, which increases proportionally with the increase in the scan rate. However, based on the relationship between the CV and GDC curves, the intensity of the observed peak at 1 V is not sufficient to form plateaus in the GDC curve of the S800 sample (Figure 14A), which confirm that charge/discharge in the $Al_2W_3O_{12}$ ceramic occurred dominantly through different processes, although not through intercalation. Therefore, the presence of the very weak peak at 1 V in Figure 16A helps to explain why the charge–discharge profile of the S800 sample is more linear compared to that of the SC700 sample.

On the other hand, in CV curves of the SC700 sample (Figure 16B), the profile could explain the parabolic-type slope without the presence of plateaus observed in Figure 14B. The two small peaks found around 1.9 and 2.4 V have already been reported by other authors [146] and correspond to the lithiation and delithiation of the secondary WS_2 phase present in the SC700 sample. Therefore, the results in Figure 16B suggest that the WS_2 secondary phase also takes part as an active material in the SC700-based electrode.

In the S800G(3:5) sample, the profile observed in Figure 16C shows a strong signal between 0.2 and 0.4 V, which corresponds to the plateau observed in Figure 5C, associated with the lithiation in the graphite, present in the S800G(3:5) sample. As for the S800 sample (Figure 16A), it is possible also to observe a faint peak around 1 V in the CV curves of the S800G(3:5) sample (Figure 16C). Therefore, it could be suggested that this peak belongs to the active $Al_2W_3O_{12}$ material, indicating that the material is undergoing a redox reaction caused by its interaction with lithium [33,147].

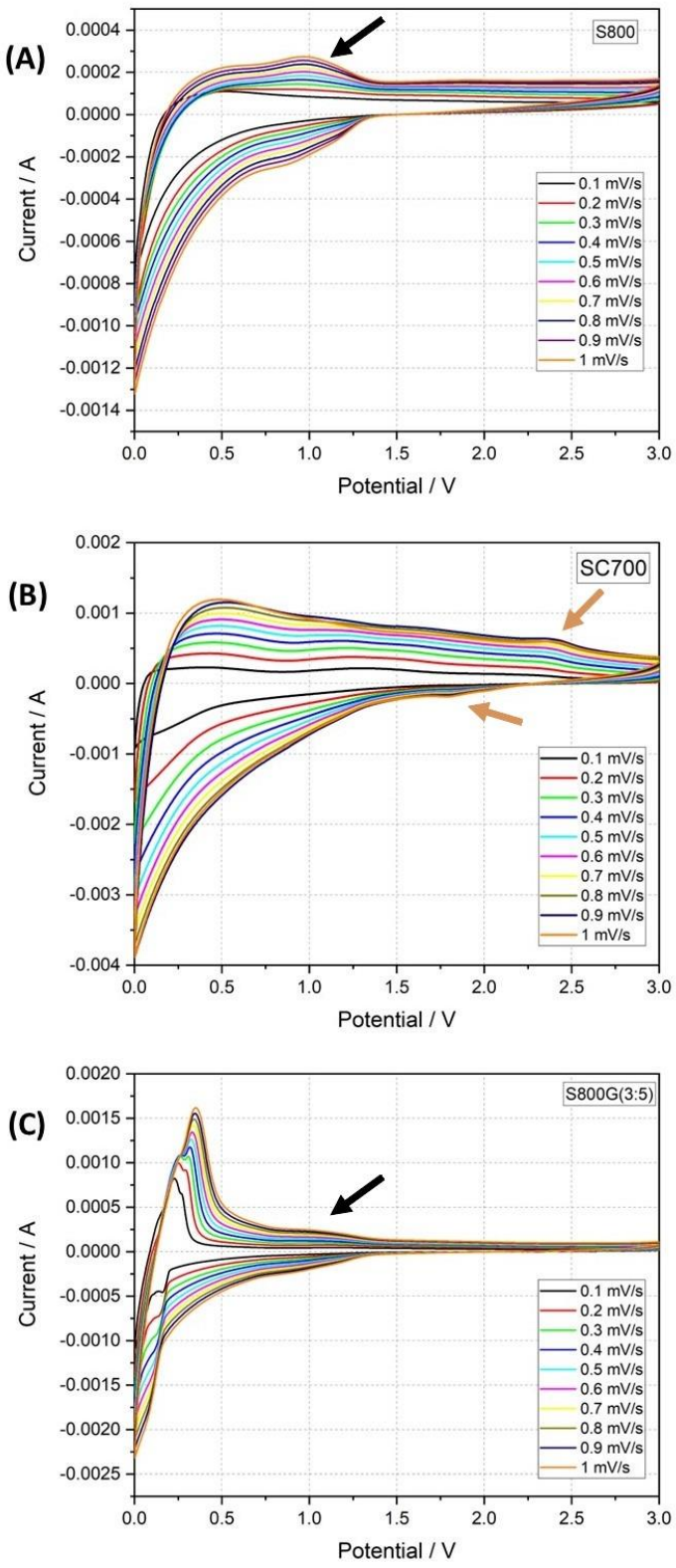

Figure 16: Cyclic voltammograms of the S800 (A), SC700 (B), and S800G(3:5) (C) samples at a scan rate from 0.1 to 1 mV s^{-1}. → and → stand for the reduction and oxidation peak of $Al_2W_3O_{12}$ and WS_2, respectively.

Based on the active material densities of the S800 ($Al_2W_3O_{12}$, 5.085 g cm^{-3}), SC700 (considering mainly $Al_2W_3O_{12}$, 5.085 g cm^{-3} as the active phase), and S800G(3:5) (a mixture of graphite, 2.854 g cm^{-3}, and $Al_2W_3O_{12}$) samples, the volumetric capacities (VC) at the 100^{th} cycle were estimated at 661.05, 1169.55, and 684.96 mAh cm^{-3}, respectively. The comparison among the samples in terms of VC reveals a similar performance between S800 and S800G(3:5). However, S800G(3:5) exhibits a slight improvement (around 4%), suggesting that the incorporation of graphite into the $Al_2W_3O_{12}$ ceramic contributes to an enhancement of VC.

In contrast, the SC700 sample shows a significantly higher VC than both S800 and S800G(3:5), highlighting the beneficial effect of carbon coating. This improvement could be attributed to the better interfacial contact provided by the carbon coating, as shown in Figure 11E and 11I, which facilitates lithium-ion transport during cycling in $Al_2W_3O_{12}$.

On the other hand, the volumetric capacity of fully lithiated graphite (719 mA h cm^{-3}) [148] is higher than that of the S800 and S800G(3:5) samples. In contrast, the VC of the SC700 sample is greater than that of graphite, confirming the importance of carbon coating as an effective strategy to improve the capacity of $Al_2W_3O_{12}$. However, compared with the volumetric capacity of some other materials, such as silicon-based anodes (2190 mA h cm^{-3}) [149], the three samples remain significantly lower.

These findings emphasize the importance of electrode architecture, demonstrating that strategies such as carbon coating or the incorporation of conductive additives not only influence gravimetric performance but also play a critical role in optimizing VC, a parameter of practical relevance for battery design.

5.1.2.3 Rate capability (RC)

Figure 17 shows the charge and discharge capacity of the samples at different current densities, such as 20, 50, 100, 150, 200, and once again 20 mA g^{-1}. At high current densities, the carbon coating in the SC700 sample enhances energy delivery compared to its carbon free counterpart (S800). This suggests that the presence of carbon coating improves the ceramic's reversibility during and after operation under high current densities. However, it is also evident from the rate capacity that there

is a constant and more pronounced drop across cycles and different current densities, which influences the material's recovery capacity. The S800 and SC700 samples exhibited a significantly lower recovery capacity, losing 23% of their capacity from cycle 10 to cycle 60. Therefore, despite the SC700 sample delivering higher energy capacity compared to the S800 sample, the capacity loss is similar in both materials. This suggests that the material's structure destabilizes like its carbon-free counterpart, although under different current densities.

On the other hand, similar to the SC700 sample, the S800G(3:5) sample exhibits a good specific capacity during and after operation under high current densities compared to the S800 sample. After 60^{th} cycles and at 20 mA g^{-1}, the capacities of the S800, SC700, and S800G(3:5) samples were 174, 314, and 292 mA h g^{-1}, respectively. Even after high current densities, the samples with carbon coating and graphite mixing exhibit good reversibility compared to their counterpart without carbon.

Furthermore, the S800G(3:5) sample exhibited a higher recovery than its counterparts, losing only 3% of its capacity from cycle 10 to cycle 60. As expected, the S800G(3:5) sample also shows a decline in energy delivery as current density increases. However, the reduction in capacity across different densities is relatively minor compared to its counterparts. It's worth noting that the diminishing of the SC700 sample between cycles 50 and 60 shows a more pronounced negative trend, bringing its capacity close to that of the S800G(3:5) sample. Additionally, the SC700 sample lacked a constant specific capacity in the final 10 cycles, indicating that it continued to lose energy capacity, making it the sample with the worst recovery performance. The data shown in Figure 17 suggest that carbon in the graphite phase benefits $Al_2W_3O_{12}$ more effectively, since the S800G(3:5) sample demonstrates better recovery after cycling at high current densities.

The enhanced energy delivery observed in the S800G(3:5) and SC700 samples is attributed, for two main reasons, to the presence of carbon. First, the sp^2 hybridization of carbon in the coating creates additional pathways for electronic conductivity, as demonstrated in previous studies [150]. Second, carbon coating provides better interfacial contact between the particles, which in turn enables more efficient electron and ion transport [151,152]. Therefore, the presence of carbon in the $Al_2W_3O_{12}$ electrodes for lithium-ion batteries significantly improves the intrinsic energy storage properties of this material.

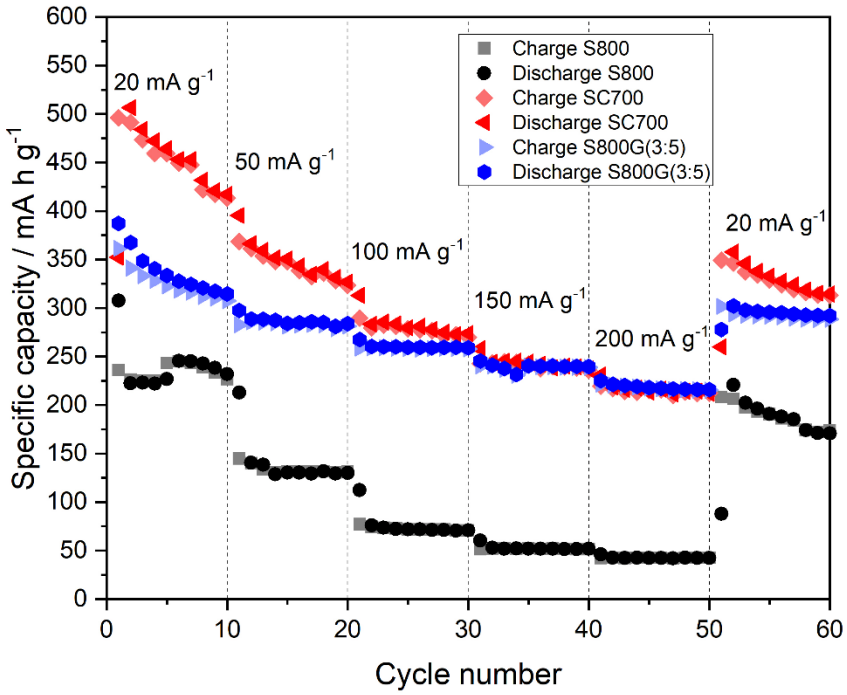

Figure 17: Rate capacity (RC) performance at 20, 50, 100, 150 200 and 20 mA g^{-1} rates for S800, SC700, and S800G(3:5).

5.1.3
Structure characterization after 100th cycles of charge-discharge

5.1.3.1
The *ex-situ* XRPD patterns

Figure 18 shows the *ex-situ* XRPD patterns of the three types of electrodes (S800, SC700, and S800G(3:5)) after the 100th charge-discharge cycle. All three samples exhibit broad humps in comparison to the initial highly crystalline $Al_2W_3O_{12}$ orthorhombic phase (Figure 10). Additionally, in the S800G(3:5) sample, a shift of ~ 0.41º (2θ) towards lower angles, is identified for the characteristic graphite diffraction lines, such as (0002), which may correspond to the intercalation of lithium ions inside the graphite layers [153].

The broad humps suggest that the orthorhombic $Al_2W_3O_{12}$ phase became amorphous during the cycling. This may indicate that the insertion of Li^+ into the

active material (orthorhombic $Al_2W_3O_{12}$) induces strain in the framework, causing its amorphization. The loss of crystallinity due to the incorporation of molecules into the framework structure has been reported in other members of the $A_2M_3O_{12}$. For instance, in $Y_2Mo_3O_{12}$, water molecules enter through the material´s microchannels, causing partial amorphization of this phase [154].

In the case of $A_2M_3O_{12}$ ceramics used as active materials in LIBs, the loss of crystallinity has been previously reported for $Sc_2W_xMo_{x-3}O_{12}$ [10], $Al_2W_{3-x}Mo_xO_{12}$ [11], and $Cr_2Mo_3O_{12}$ [12]. No crystalline peaks were observed after full charge-discharge cycling for $Sc_2W_xMo_{x-3}O_{12}$ [10] and $Cr_2Mo_3O_{12}$ [12]. In contrast to our results, Schulz et al. [11] reported a reduction but not a complete disappearance of diffractions lines of the orthorhombic $Al_2W_3O_{12}$. On the other hand, their sample delivered a lower capacity at the 100th cycle (96 mA h g^{-1}) compared to the $Al_2W_3O_{12}$ reported in this study (130 mA h g^{-1} for S800 sample), likely due to the higher current density applied in their tests (30 mA g^{-1}) relative to the conditions used in this work (20 mA g^{-1}).

These results indicate that the amorphization observed in the samples is largely irreversible under the applied cycling conditions and can permanently compromise performance by reducing structural stability and long-range Li^+ diffusion pathways.

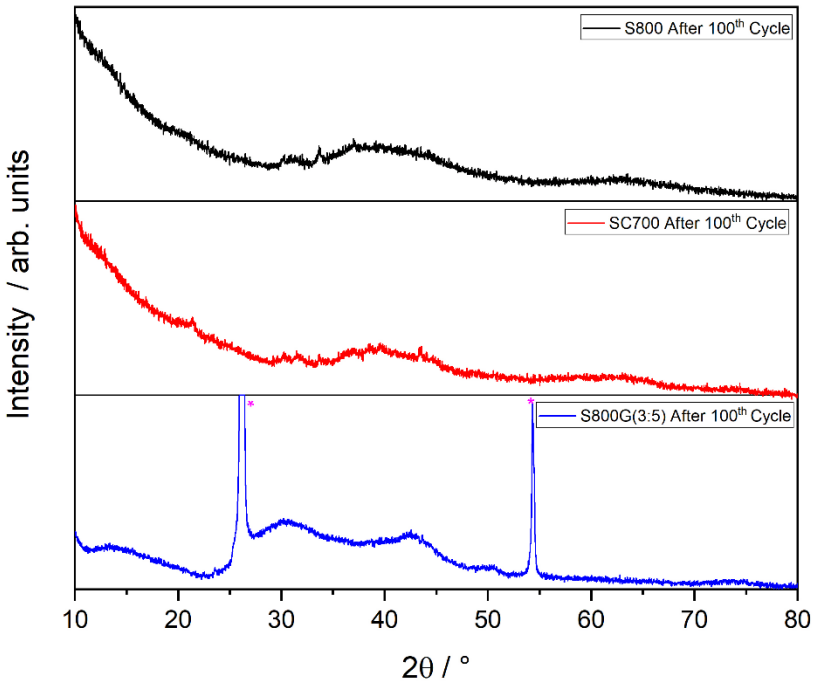

Figure 18: The XRPD patterns of the S800, SC700, and S800G(3:5) electrodes after the 100th cycle. * stands for the diffraction lines of graphite.

5.1.3.2 SEM images

SEM images of the S800, SC700, and S800G(3:5) electrodes before cycling are presented in Figure 19A, C, and E, respectively. In addition, SEM images of electrodes after 100th cycles are presented in Figure 19 B, D, and F for the same samples.

Figure 19A shows the agglomerated grain structure of $Al_2W_3O_{12}$, while in the samples with carbon coating and graphite mixing (Figures 19 C and E), the oxide particles are well mixed within the carbon matrix. It is possible to identify sharp facets in Figures 19A, 19C, and 19E, which are characteristic of crystalline solids. Notably, in Figure 19C (SC700), the $Al_2W_3O_{12}$ grains appear to be more connected than in Figure 19E (S800G(3:5)), where more voids between particles can be observed. Therefore, the carbon coating present in the SC700 samples promotes better contact between particles, allowing good conductivity for Li^+ transport. This

is consistent with the results shown in Figure 15, where the SC700 sample delivered more energy than its two counterparts up to the 60th cycle.

Morphological and structural changes occur in the three electrode materials after cycling, as shown in Figures 19 B, 19D, and 19F, corroborating the XRPD amorphous patterns shown in Figure 18.

During the charge-discharge processes, the lithium interacting with the crystalline structure of $Al_2W_3O_{12}$ causes, probably, volumetric changes within the structure and induces stress. This can lead to the amorphization of $Al_2W_3O_{12}$ structure and formation of cracks in microstructure, as observed in Figures 19 B and 19D. The cracks in the S800 and SC700 samples after cycling are a consequence of the volume change between cycles caused by the diffusion of Li^+ within the material [155].

The faster decrease in capacity of sample SC700 compared to sample S800G(3:5) is primarily due to the lower structural integrity and electrical stability of the carbon coating formed by sucrose pyrolysis. While this carbon coating initially improves the connectivity of the $Al_2W_3O_{12}$ particles, it has a higher tendency to fracture during repeated lithiation and delithiation cycles. This promotes crack formation (as shown in Figure 19D), resulting in the loss of interparticle contact and disruption of electron and lithium ion transport pathways, as reflected in the pronounced capacity decrease observed in Figure 15.

In contrast, the graphite in S800G(3:5) provides a continuous and more ordered conductive network [156], which buffers microstructural changes, prevents crack formation (not observed in Figure 19F), and maintains electrical connectivity during cycling (as shown in Figure 15). These characteristics explain the superior long-term electrochemical stability and higher specific capacity retention of S800G(3:5).

Li^+ ions can be reversibly intercalated and deintercalated from graphite with little structural distortion thanks to its stable layered structure [157]. This stability reduces mechanical stress and inhibits the formation of cracks in the electrodes with S800G(3:5) sample by buffering the volume changes of the active material agglomerates during cycling. Consequently, unlike the SC700 sample, where these pathways are disrupted, in the S800G(3:5) continuous pathways for Li^+ insertion and extraction are preserved due to the presence of graphite.

This is confirmed by the measurements presented in Figures 15 and 17, which correspond to the GDC and RC results, respectively. Considering the gravimetric capacity, these results indicate that the sample with graphite exhibits superior performance compared to its two counterparts, demonstrating higher specific capacity and greater electrochemical stability.

Furthermore, the RC (Figure 17) shows an improved response for the S800G(3:5) sample, which is attributed to the presence of graphite. Therefore, it seems that the S800G(3:5) does not present cracks after cycling. The absence of cracks in this sample after complete charge-discharge cycling (Figure 19 F), along with the results of GCD and RC shown in the Figures 15 and 17, respectively, demonstrates that graphite enhances the storage properties of the $Al_2W_3O_{12}$-based electrode buffering the changes in the microstructure and increasing the conductivity.

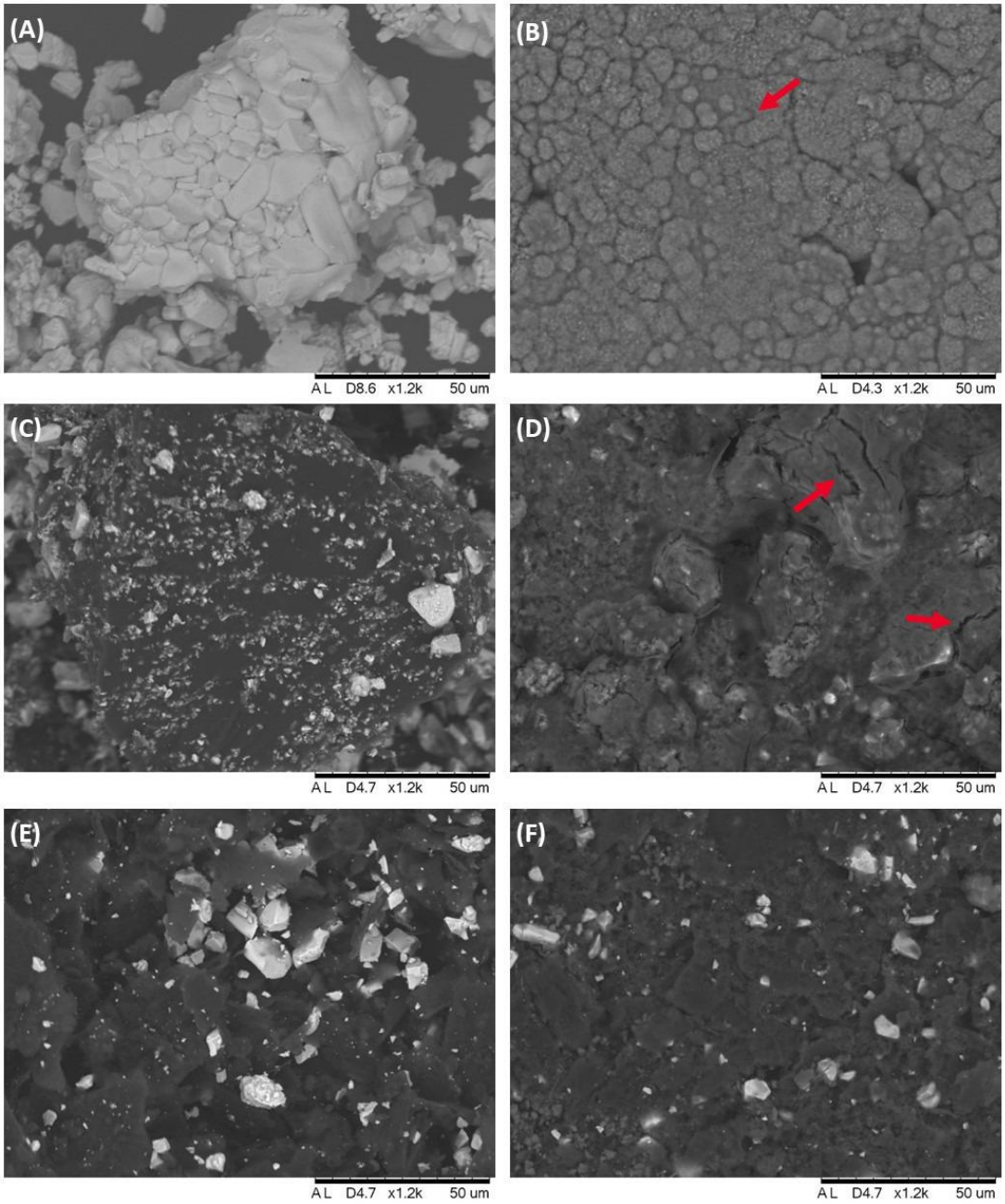

Figure 19: SEM images of S800, SC700 and S800G(3:5) electrodes before cycling (A, C, E respectively, left column) and after 100th cycles (B, D, F, right column).

5.2
Effect of OV in $Al_2W_3O_{12}$ based electrodes

5.2.1
Structural characterization before cycling

5.2.1.1
XRPD patterns and SEM images

The XRPD patterns and SEM image of electrodes prepared with SH400 are presented in Figure 20A and B, respectively. As shown in Figure 20A, the electrode with the SH400 sample before cycling exhibits sharp and intense diffraction lines, indicating its high crystallinity. The diffraction pattern corresponds to the orthorhombic phase of $Al_2W_3O_{12}$ at room temperature with the *Pbcn* space group [81]. Traces of secondary phases, such as WO_3 [113] and/or WO_{3-x} [115], are also observed. Additionally, the strong peaks at 42.96º, 50.10º, and 73.82º (2θ) correspond to cubic Cu [158,159], characteristic of the Cu foil used as a support of active material. The pattern in Figure 20A is consistent with the orthorhombic phase of $Al_2W_3O_{12}$ without OV (sample S800), which exhibits the same space group and secondary phases [41].

Figure 20B shows the SEM image of the electrode before cycling, made of SH400 powder as active material. It is possible to observe that the morphology of SH400 sample has agglomerated $Al_2W_3O_{12}$ grains with sharp borders and plane faces, which are characteristics of crystalline materials. Furthermore, Figure 20B shows no visible cracks or other three-dimensional defects. Super P carbon material, surrounding the $Al_2W_3O_{12}$ grains, represented by dark regions, is also visible.

Additionally, the $Al_2W_3O_{12}$ materials with and without OV (SH400 and S800, respectively) are ceramics with negligible or low porosity, as confirmed by nitrogen adsorption/desorption analyses (Figures S7A and S7B). Moreover, both samples display a type II isotherm with low specific surface areas of 1.91 $m^2 g^{-1}$ for S800 and 4.66 $m^2 g^{-1}$ for SH400.

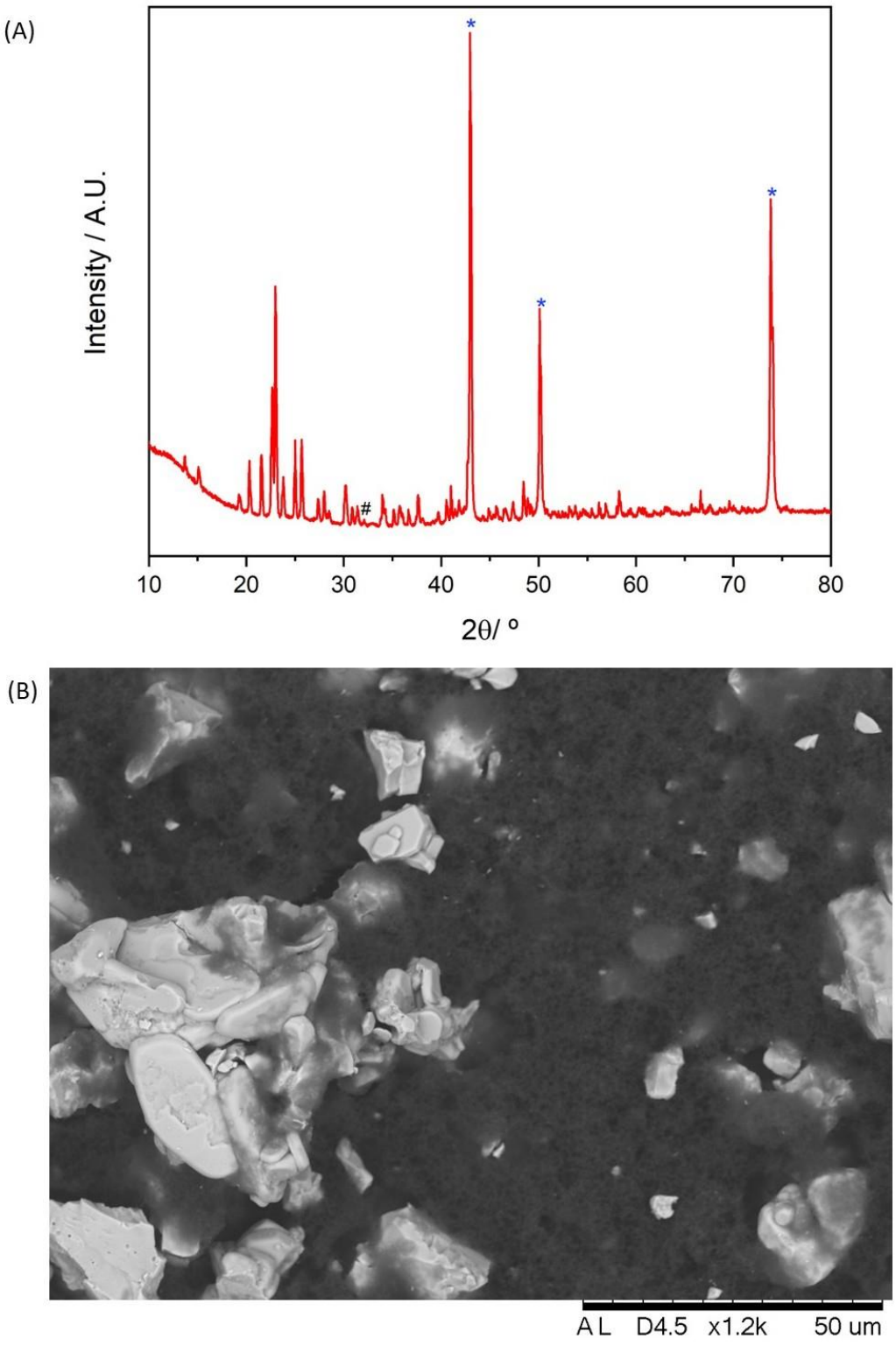

Figure 20: The XRPD pattern (A) and SEM image (B) of the SH400 sample before cycling; * and # stand for diffraction lines of Cu foil and monoclinic WO_3 or WO_{3-x}, respectively; white particles in SEM image belong to $Al_2W_3O_{12}$.

5.2.1.2 EPR

OV in SH400 was identified and quantified using EPR. Unlike the EPR spectra of $Al_2W_3O_{12}$ without post-synthesis treatment [41], the spectrum shown of SH400 powder in Figure 21 reveals an EPR signal. This signal, observed at Landé g-factor of 2.0035, suggests the presence of a single-electron-trapped oxygen vacancy (SETOV) inside the $Al_2W_3O_{12}$ crystal structure [160–163]. The concentration of SETOV in the SH400 sample was estimated at 8.8×10^{14} cm $^{-3}$ and was calculated from double integration of the simulated curve Figure 2, and compared to a standard $CuSO_4$ sample.

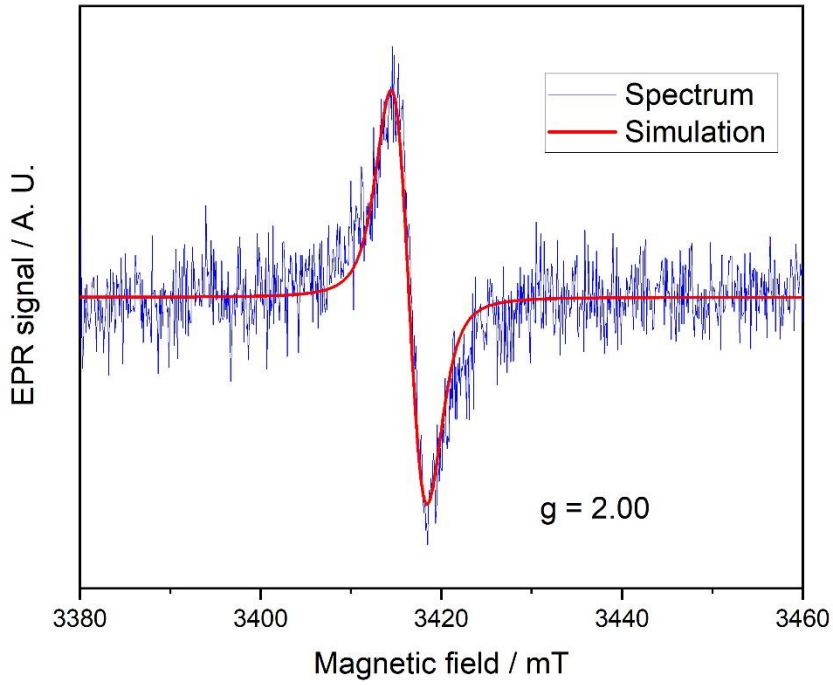

Figure 21: EPR spectrum and its simulation (Full red line) for $Al_2W_3O_{12}$ (SH400). The Landé g-factor of 2.0035 is attributed to SETOV.

5.2.2
Electrochemical performance

5.2.2.1
Cyclic voltammetry (CV)

Figures 16A and 22 show the CV of S800 and SH400 samples, respectively. The two voltammograms are similar in form and present one anodic peak around 1 V, which decreases proportionally with the decrease in the scan rate. The data acquired by CV suggested that OV in the SH400 ceramic did not significantly influence the material's electrochemical properties. Additionally, neither voltammogram shows the Gaussian-like peaks typically observed in reversible systems [145], which suggests limited reversibility.

Moreover, based on Figures 16A and 22, the Randles-Sevick equation [164] (Figures S8 and S9, supporting information) was employed to estimate the lithium diffusion coefficient (D_{Li}) in the both electrodes. D_{Li} values for the S800 and SH400 samples have been estimated at 4.12 $x10^{-17}$ m^2 s^{-1} and 2.65 x 10^{-17} m^2 s^{-1}, respectively. Contrary to expectation, the presence of OV in the $Al_2W_3O_{12}$ ceramic did not enhance the D_{Li} in this particular case. Instead, it was reduced by 36% compared to the sample without OV (S800).

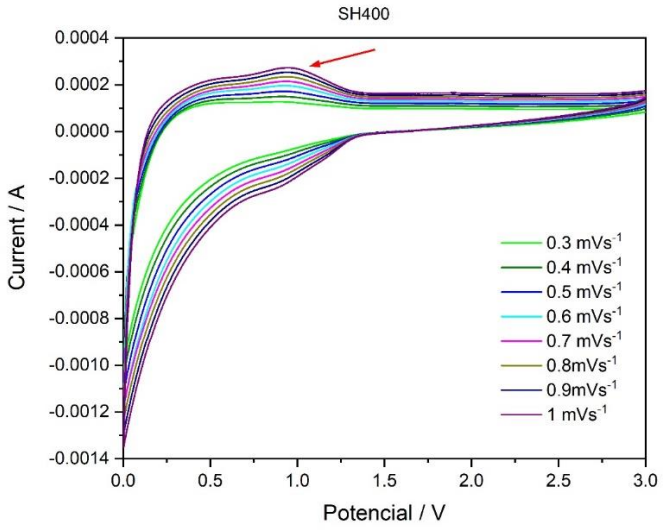

Figure 22: Cycle Voltammograms of SH400 samples at a scan rate from 0.3 to 1 mV s^{-1}. Red arrow stands for anodic peak around 1 V.

5.2.2.2
Galvanostatic charge/discharge

The difference in D_{Li} is coherent with the difference in the specific capacity shown in Figures 23A and 23B for S800 and SH400 electrodes, respectively. For instance, the specific capacity at the 10^{th} cycle was 240 mA h g^{-1} for the S800 sample (without OV) and 219 mA h g^{-1} for the SH400 sample (with OV). By the 100^{th} cycle, the trend remained similar, with 133 mA h g^{-1} for the S800 sample and 110 mA h g^{-1} for the SH400 sample.

On the other hand, Figures 23A and 23B show a change in the slope around ~0.68 V and ~1.13 V in the first cycle for S800 and SH400 samples, respectively. This suggests that the presence of OV in the $Al_2W_3O_{12}$ electrode initially improves the working voltage. However, this advantage disappears in the second cycle. The working voltage in subsequent cycles (*i.e.*, cycles 2, 10, and 100) in the SH400 electrode is practically the same as that of the sample without OV (S800), which suggests that the lithiation and delithiation processes inside initially crystalline $Al_2W_3O_{12}$ eliminate the potential advantage of the presence of OV. Furthermore, none of the GCD curves (Figure 23A and 23B) shows the characteristic plateau of lithium-ion intercalation [133]. Consequently, it can be inferred that the OV in this compound do not produce any enhancement in the electrochemical performance.

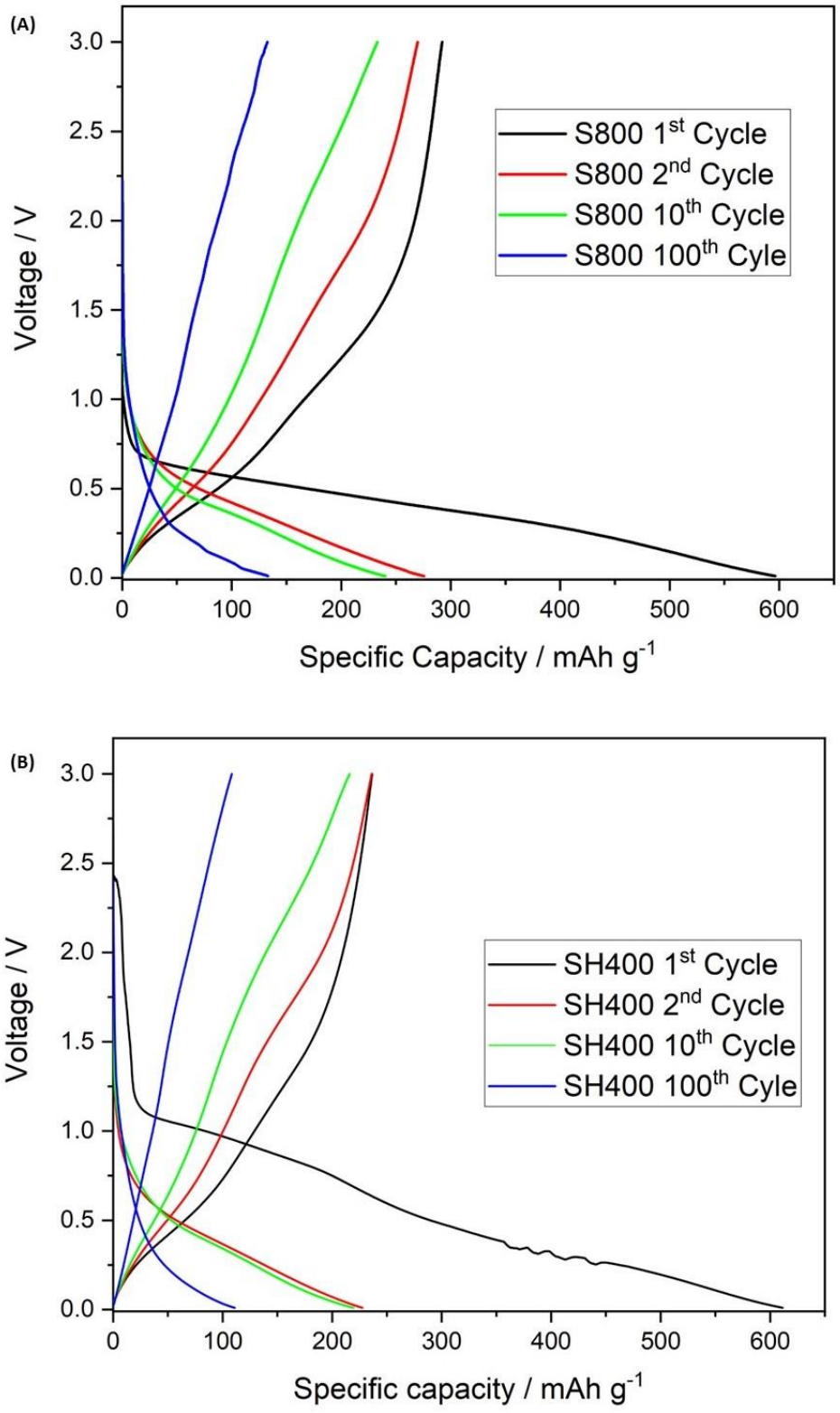

Figure 23: GCD curves of cells with S800 (A) and SH400 (B) of 1st, 2nd, 10th, and 100th cycles between 0.01 and 3.0 V at a current density of 20 mA g^{-1}.

Figures 24 A and B illustrate the cycling performance of the S800 and SH400 samples. In the first cycle, both samples exhibited high specific capacity at 20 mA g^{-1}, achieving 596 mA g^{-1} for S800 and 611 mA g^{-1} for SH400. However, the initial Coulombic efficiency (CE) was only 48% for S800 and 38% for SH400, indicating that a significant portion of the lithium ions present in the cell was consumed during the first cycle and not recovered in subsequent cycles, most probably due to the formation of the solid electrolyte interface (SEI) [136].

In the second cycle, the specific capacity decreased to 275 mA h g^{-1} for S800 and 227 mA h g^{-1} for SH400, corresponding to 46% and 37% of the first cycle, respectively. No sharp drop in specific capacity was further observed in the subsequent cycles, although a slight and consistent decrease was recorded throughout the following cycles, with CE values varying between 96% and 99%.

The charge/discharge cyclability of both samples is practically the same. It is relevant to note that between the cycles 50 and 60 (Figure 24A) the S800 sample shows an interruption in the trend caused by a temperature fluctuation in the laboratory due to environmental conditions. However, after the 60^{th} cycle, the trend aligns with the behavior observed in previous cycles.

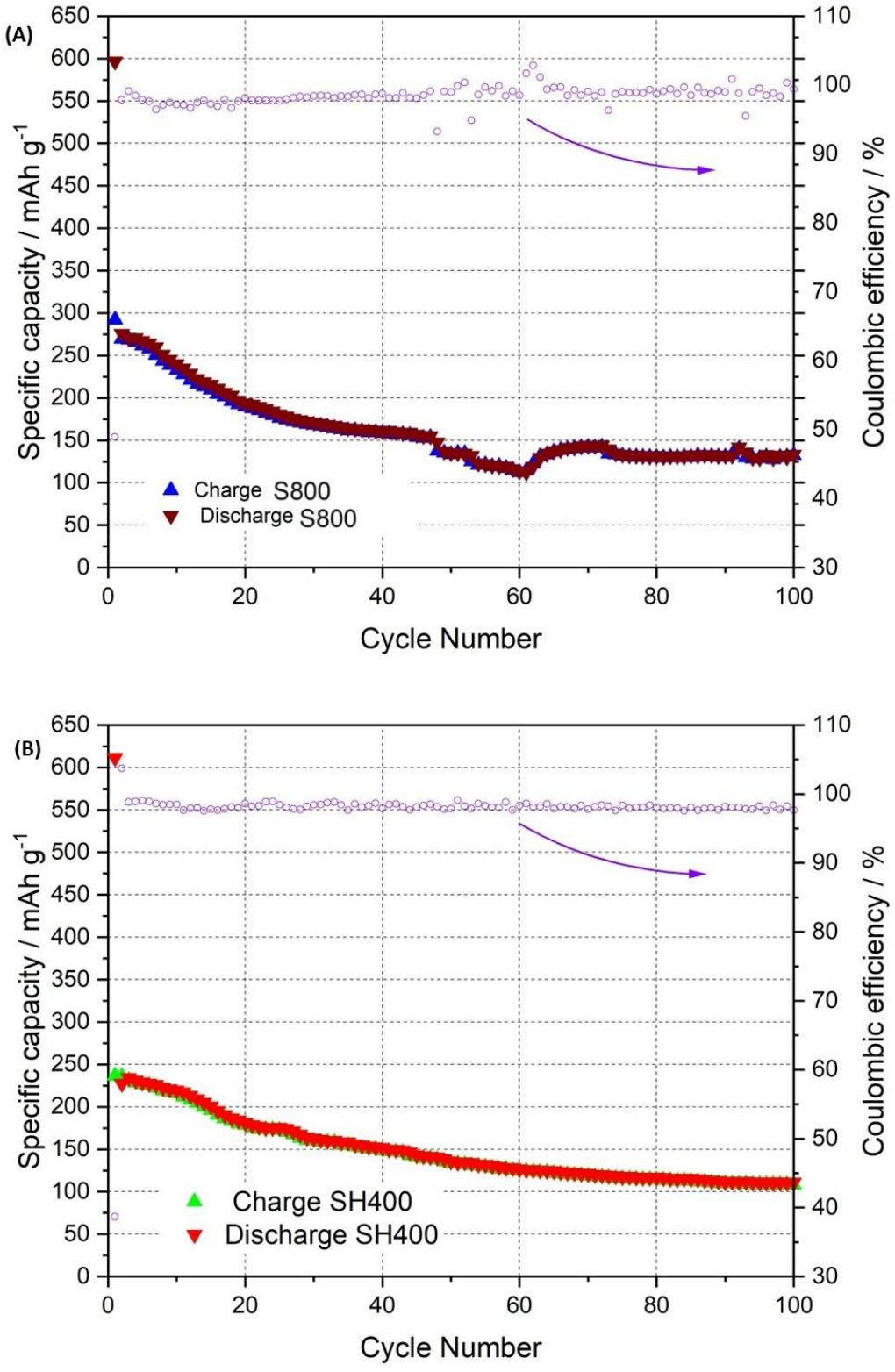

Figure 24: Electrochemical performance and CE of cells with S800(A) and SH400(B) electrodes cycled between 0.01 and 3.0 V at a current density of 20 mA g^{-1}.

5.2.2.3
Rate capability (RC)

Figure 25 compares the RC of the S800 and SH400 electrodes at charge/discharge rates of 20, 50, 100, 150, 200, and 20 mA g^{-1}. Except for the first 10 cycles, the profiles displayed in Figure 25 are almost identical. Contrary to expectations, even at high current densities, the specific capacity remains the same for both samples between the 10th and 60th cycles at all current rates. At the 52nd cycle, for a current density of 20 mA g^{-1}, both electrodes lost 8% of their energy delivery capacity compared to the 10th cycle. These results show that there is no electrochemical enhancement due to the OV in the sample SH400.

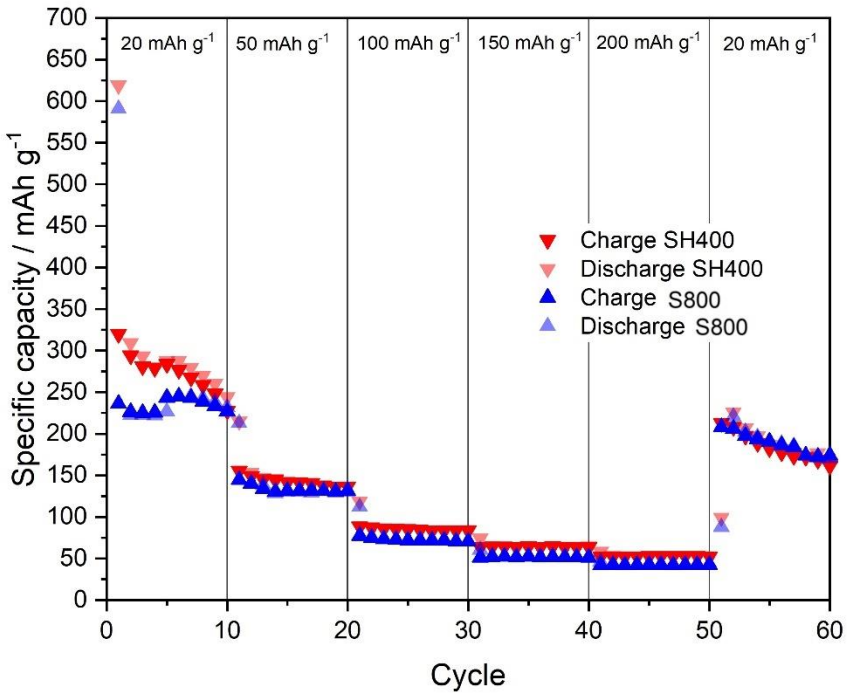

Figure 25: Discharge capacity *vs.* cycle number of S800 and SH400 electrodes at 20, 50, 100, 150, 200, and 20 mA g^{-1}.

Our results found that oxygen vacancies do not appear to have a positive effect on the electrochemical properties of the electrode based on $Al_2W_3O_{12}$ ceramic. In fact, there is no significant change in the electrochemical response of $Al_2W_3O_{12}$ with or without OV. This is consistent with the D_{Li} values and with the findings from the 100th GCD cycle (Figure 23), where the sample without OV, *i.e.*, S800, performed even better than the one with OV. Additionally, as observed in

Figure 25 (results of the RC), the performance at high current densities did not reveal any advantage from the presence of OV in the $Al_2W_3O_{12}$-based electrode, in contrast to some other studies, where the influence of oxygen vacancies and phase transformations enhances the energy capacity delivered at high current densities [28,147].

On the one hand, electrodes with a high surface area and porous structure typically exhibit improved specific capacity, as the electrolyte can have better contact with the active material. This enhances lithium-ion storage and increases the diffusion pathways for lithium ions, which results in greater specific capacity [165]. Several studies have demonstrated that high surface area and porosity improve the electrochemical performance [166,167]. However, as confirmed by the nitrogen adsorption/desorption analyses (Figure S7A and S7B), the S800 and SH400 samples are non-porous materials with low specific surface areas, and the post-synthesis treatment used to obtain the SH400 sample does not affect the material's porosity. Therefore, the influence of the contact between the active material and the electrolyte should not be considered.

5.2.3
Structure characterization after 2nd cycles of charge-discharge

5.2.3.1
XRPD patterns and SEM imagens

The structural characterization of the SH400 sample after the second cycle is shown in Figure 26. Figure 26A presents the *ex-situ* XRPD pattern of the electrode cycled up to the 2nd cycle. Similar to the XRPD pattern of S800 after the 2nd cycle (Figure S11A), the characteristic diffraction lines of $Al_2W_3O_{12}$ crystalline structures in the SH400 sample have disappeared, and no crystalline phase can be identified (besides the diffraction lines from Cu foil).

XRPD pattern of SH400 shows broad humps compared to the sharp peaks observed in Figure 20A, due to crystalline, orthorhombic, $Al_2W_3O_{12}$. This data suggested a rapid transformation of crystalline $Al_2W_3O_{12}$ into an amorphous phase, likely induced by the insertion of lithium ions during the first GCD cycle. The amorphization of the $A_2M_3O_{12}$ ceramic family after electrochemical cycling has also been reported by other researchers and is attributed to the insertion of Li^+ ions into

the crystal structure [10–12]. For instance, $Cr_2Mo_3O_{12}$ becomes amorphous after the first cycle and maintains amorphous form after full charge/discharge cycles [12].

Figure 26B shows the morphology of the electrode with SH400 as active material after the second cycle, where the presence of $Al_2W_3O_{12}$ is evident as white particles. However, based on the XRPD pattern in Figure 26A and in contrast to the initial result shown in Figure 20A, these particles already corresponded to amorphized $Al_2W_3O_{12}$, as also observed in the SEM image of the OV-free S800 sample (Figure S11B). Additionally, cracks can be observed on the electrode surface, which are attributed to volumetric changes caused by the insertion and extraction of lithium ions within the active material's structure. These volumetric changes may generate internal stress in the carbon material surrounding the $Al_2W_3O_{12}$ particles. The stress is released as long cracks within the carbon coating, instead of in the active material with OV, as suggested by some studies [168,169], which instead suffered amorphization.

According to Figure 26A, the $Al_2W_3O_{12}$ electrode with OV exhibits a quick loss of crystallinity and shows signs of irreversible phase transformation to an amorphous phase. Amorphization phenomenon at atmospheric pressure has already been reported by Marinkovic et al. [154] for $A_2M_3O_{12}$ ceramic family. These authors observed that the entry of water molecules through the intrinsic microchannels of the structure causes partial amorphization of the $Y_2Mo_3O_{12}$ phase. A more recent study [39] suggests that $Al_2W_3O_{12}$ with OV is more flexible and undergoes a phase transition under relatively low pressures, in comparison to its OV-free counterpart. In addition, the amorphization phenomenon has been previously reported in other studies with the members of the $A_2M_3O_{12}$ family as electrodes in LIBs [10–12].

As demonstrated in some previous studies, active materials in electrodes based on more classical phases such as $LiNi_{0.5}Co_{0.2}Mn_{0.3}O_2$ or $LiCoO_2$ retain their original crystal structure during and after the cycling process [170,171], which is essential for preserving the intrinsic electrochemical properties of the material. In contrast, the structural characterization after the 2nd cycle, shown in Figure 26, suggests that the $Al_2W_3O_{12}$-based electrode is unable to maintain original or acquire a new crystalline structure. This irreversible amorphization could suppress the beneficial effects typically associated with OV in the material. As a consequence of the amorphization, the lithium-ion transport pathways could be disrupted or

obstructed, which decreases ion mobility and consequently reduces the diffusion coefficient, as calculated by Randles-Sevick equation.

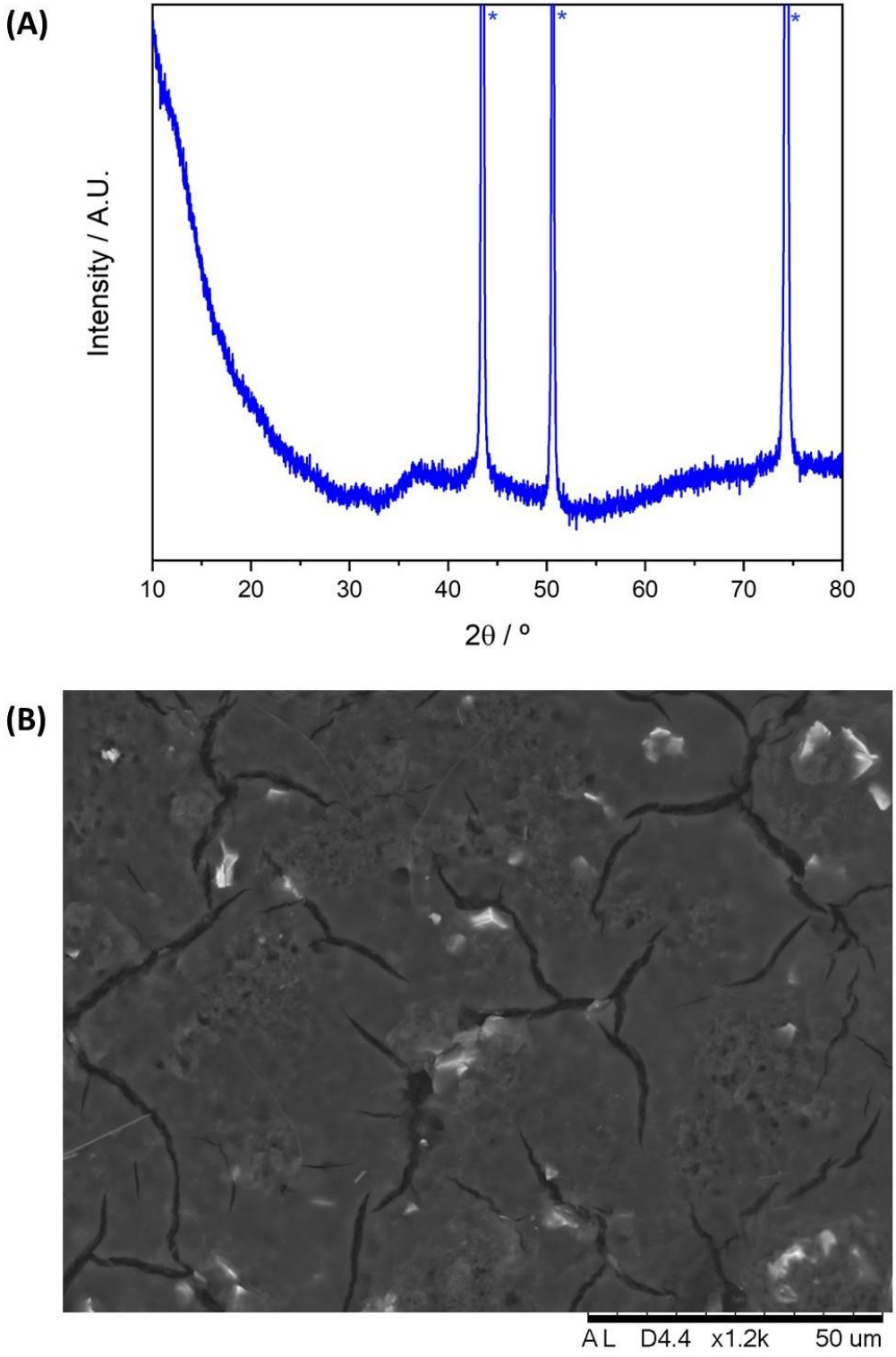

Figure 26: XRPD pattern and SEM image of the SH400 sample after the 2nd cycle. * stands for diffraction lines of Cu foil (support of active material, SH400).

6
Conclusions

The $Al_2W_3O_{12}$ ceramic was successfully synthesized, coated, and mixed with carbon using two different post-synthesis routes. It was confirmed that the orthorhombic crystal structure of the ceramic was not affected by the mechanical or chemical treatments applied in post-synthesis.

$Al_2W_3O_{12}$ was successfully evaluated as an active material for electrodes in LIBs. According to the GCD test at 20 mA h g^{-1}, the electrode using $Al_2W_3O_{12}$ without a carbon coating or graphite mixing (S800 sample) delivered a specific capacity of 130 mA h g^{-1} at the end of the test. Furthermore, the absence of a characteristic plateau for Li^+ intercalation inside $Al_2W_3O_{12}$ suggests that the charge-discharge process in the $Al_2W_3O_{12}$ ceramic occurs predominantly through multiple mechanisms, which do not involved intercalation.

Lithium electrochemical cells using SC700 and S800G(3:5) materials as the active material, which are $Al_2W_3O_{12}$ ceramics with carbon coating or graphite mixing, showed superior performance compared to their carbon-free counterpart (S800). The addition of carbon by both routes proves to be a simple and relatively effective method for improving the electrochemical response.

The S800G(3:5) material (a mixture of $Al_2W_3O_{12}$ and crystalline graphite) delivered the highest discharge capacity of 240 mA h g^{-1} in the 100^{th} cycle, which is significantly higher than the 130 mA h g^{-1} delivered by the S800 sample. Additionally, the GCD and RC measurements indicate that the graphite mixing is more effective in enhancing electrochemical properties and storage capacity than the carbon coating applied in the SC700 sample.

The orthorhombic $Al_2W_3O_{12}$ phase became amorphous in all three materials (S800, SC700, and S800G(3:5)) as observed for the samples submitted to 100 charge-discharge cycles. However, despite their inability to return to a crystalline phase after cycling, the preparation method used for the S800G(3:5) material proved to be a promising approach for enhancing the electrochemical properties of $Al_2W_3O_{12}$ as an electrode material for LIBs.

On the other hand, it was found that the incorporation of OV in orthorhombic $Al_2W_3O_{12}$ has little relevance to the electrochemical performance of $Al_2W_3O_{12}$-based electrodes in LIB, probably due to the material's inability to sustain an open framework crystal structure during cycling.

As a matter of fact, amorphization of $Al_2W_3O_{12}$ with OV was evidenced by XRPD as soon as the second cycle of the GCD process is concluded. Therefore, although OV are generally considered a promising strategy to enhance the electrochemical properties of LIB electrodes, the loss of structural integrity in the $Al_2W_3O_{12}$ prevents the material from benefiting from the presence of OV. In fact, the electrochemical results suggest that the presence of OV does not enhance the electrochemical performance of $Al_2W_3O_{12}$-based material.

This study, therefore, provides evidence that highlights the importance of maintaining an open framework crystal structure in members of the $A_2M_3O_{12}$ family for its application in LIB as electrodes. The findings presented here should serve as a basis for further investigation of the influence of OV in other $A_2M_3O_{12}$ compounds to be considered as active material in electrodes for secondary batteries that employ ions other than lithium.

7
References

(1) Song, K.; Agyeman, D. A.; Park, M.; Yang, J.; Kang, Y. M. High-Energy-Density Metal–Oxygen Batteries: Lithium–Oxygen Batteries vs Sodium–Oxygen Batteries. *Advanced Materials*. **2017**. https://doi.org/10.1002/adma.201606572.

(2) Primo, E. N.; Eroles, F.; Rojas, M. del C.; Cometto, F.; Leiva, E.; Barraco, D. E.; Luque, G. L. Mechanical Properties vs. Interaction Strength: Comprehensive Understanding of Aqueous Binders' Formulation on Si-Based Anodes for Lithium-Ion Batteries. *J. Power Sources.* **2023**. https://doi.org/10.1016/j.jpowsour.2023.232800.

(3) Amici, J.; Calderón, C. A.; Versaci, D.; Luque, G.; Barraco, D.; Leiva, E.; Francia, C.; Bodoardo, S. Composite Polymer Electrolyte with High Inorganic Additive Contents to Enable Metallic Lithium Anode. *Electrochim. Acta*. **2022**. https://doi.org/10.1016/j.electacta.2021.139772.

(4) Pan, Y.; Xu, K.; Wang, R.; Wang, H.; Chen, G.; Wang, K. Lithium-Ion Battery Condition Monitoring: A Frontier in Acoustic Sensing Technology. *Energies*. **2025**. https://doi.org/10.3390/en18051068.

(5) Yoshino, A. The Birth of the Lithium-Ion Battery. *Angewandte Chemie - International Edition*. **2012**. https://doi.org/10.1002/anie.201105006.

(6) Lee, S.; Manthiram, A. Can Cobalt Be Eliminated from Lithium-Ion Batteries? *ACS Energy Letters*. **2022**. https://doi.org/10.1021/acsenergylett.2c01553.

(7) Ge, X.; Yuan, B.; Xu, S.; Xu, P.; Shi, Y.; Liu, Y.; Li, Z.; Sun, Q.; Guo, J.; Liang, E.; Li, B. Anodic Lithium Ion Battery Material with Negative Thermal Expansion. *Ceram. Int.* **2020**. https://doi.org/10.1016/j.ceramint.2020.04.248.

(8) Wang, M.; Wei, Y.; Xu, S.; Jing, N.; Hao, H.; Yang, L.; Wang, Z.; Wang, G. Simultaneously Adjusting Deformation and Heat Using a Negative Thermal Expansion Material to Enhance Electrochemical Performance and Safety of

Lithium-Ion Batteries. *Chem. Eng. J.* **2021**. https://doi.org/10.1016/j.cej.2021.131434.

(9) Mittal, U.; Teusner, M.; Brand, H. E. A.; Mata, J.; Kundu, D.; Sharma, N. Effect of Post-Synthesis Processing on the Electrochemical Performance of $Y_2W_3O_{12}$. *Energy and Fuels.* **2023**. https://doi.org/10.1021/acs.energyfuels.2c04089.

(10) Liu, J.; Johannessen, B.; Brand, H. E. A.; Andersen, H. L.; Sharma, N. The $Sc_2W_xMo_{3-x}O_{12}$ series as Electrodes in Alkali-Ion Batteries. *CrystEngComm* **2021**. https://doi.org/10.1039/d1ce00318f.

(11) Schulz, B.; Andersen, H. L.; Al Bahri, O. K.; Johannessen, B.; Liu, J.; Primig, S.; Sharma, N. Electrochemical Performance and Structure of $Al_2W_{3-x}Mo_xO_{12}$. *CrystEngComm.* **2018**. https://doi.org/10.1039/c7ce01707c.

(12) Guo, L.; Wang, Y. New $Cr_2Mo_3O_{12}$-Based Anodes: Morphology Tuning and Li-Storage Properties. *J. Mater. Chem. A.* **2015**. https://doi.org/10.1039/c5ta03256c.

(13) Marinkovic, B. A.; Pontón, P. I.; Romao, C. P.; Moreira, T.; White, M. A. Negative and Near-Zero Thermal Expansion in $A_2M_3O_{12}$ and Related Ceramic Families: A Review. *Frontiers in Materials*. **2021**. https://doi.org/10.3389/fmats.2021.741560.

(14) Jardim, P. M.; Garcia, E. S.; Marinkovic, B. A. Young's Modulus, Hardness and Thermal Expansion of Sintered $Al_2W_3O_{12}$ with Different Porosity Fractions. *Ceram. Int.* **2016**. https://doi.org/10.1016/j.ceramint.2015.12.045.

(15) Prisco, L. P.; Pontón, P. I.; Guamán, M. V.; Avillez, R. R.; Romao, C. P.; Johnson, M. B.; White, M. A.; Marinkovic, B. A. Assessment of the Thermal Shock Resistance Figures of Merit of $Al_2W_3O_{12}$, a Low Thermal Expansion Ceramic. *J. Am. Ceram. Soc.* **2016**. https://doi.org/10.1111/jace.14160.

(16) Hao, H.; Xu, S.; Jing, N.; Wang, M.; Wang, Z.; Yang, L.; Chen, J.; Wang, G.; Wang, G. Negative Thermal Expansion Material: Promising for Improving Electrochemical Performance and Safety of Lithium-Ion Batteries. *J. Phys. Chem. Lett.* **2021**. https://doi.org/10.1021/acs.jpclett.1c01332.

(17) Xu, S.; Jing, N.; Hao, H.; Wang, M.; Wang, Z.; Yang, L.; Wang, G.; Chen, J.; Wang, G. Enhanced Electrochemical Performance of $LiNi_{0.6}Co_{0.2}Mn_{0.2}O_2$ by a Negative-Thermal-Expansion Material at Elevated Temperature.

Energy Technol. **2021**. https://doi.org/10.1002/ente.202100183.

(18) Evans, J. S. O.; Mary, T. A. Structural Phase Transitions and Negative Thermal Expansion in $Sc_2(MoO_4)_3$. *Inorganic Materials.* **2000**. https://doi.org/10.1016/S1466-6049(00)00012-X.

(19) Romao, C. P.; Miller, K. J.; Whitman, C. A.; White, M. A.; Marinkovic, B. A. Negative Thermal Expansion (Thermomiotic) Materials. *Comprehensive Inorganic Chemistry II.* **2013**. https://doi.org/10.1016/B978-0-08-097774-4.00425-3.

(20) Lind, C. Two Decades of Negative Thermal Expansion Research: Where Do We Stand? *Materials*. **2012**. https://doi.org/10.3390/ma5061125.

(21) Liu, J.; Sharma, N. Thermal Evolution and Phase Transitions in Electrochemically Activated $Sc_2(MoO_4)_3$. *Inorg. Chem.* **2019**. https://doi.org/10.1021/acs.inorgchem.9b01116.

(22) Shi, Y.; Wen, L.; Pei, S.; Wu, M.; Li, F. Choice for Graphene as Conductive Additive for Cathode of Lithium-Ion Batteries. *J. Energy Chem.* **2019**. https://doi.org/10.1016/j.jechem.2018.03.009.

(23) Song, J.; Sun, B.; Liu, H.; Ma, Z.; Chen, Z.; Shao, G.; Wang, G. Enhancement of the Rate Capability of $LiFePO_4$ by a New Highly Graphitic Carbon-Coating Method. *ACS Appl. Mater. Interfaces.* **2016**. https://doi.org/10.1021/acsami.6b02567.

(24) Huang, X.; Du, Y.; Qu, P.; Liang, F.; Dai, Y.; Yao, Y. Effect of Carbon Coating on the Properties and Electrochemical Performance of $LiFePO_4$ /C Composites by Vacuum Decomposition Method. *Int. J. Electrochem. Sci.* **2017**. https://doi.org/10.20964/2017.08.77.

(25) Qian, L.; Lan, J. Le; Xue, M.; Yu, Y.; Yang, X. Two-Step Ball-Milling Synthesis of a Si/SiO_x/C Composite Electrode for Lithium Ion Batteries with Excellent Long-Term Cycling Stability. *RSC Adv.* **2017**. https://doi.org/10.1039/c7ra06671f.

(26) Chauque, S.; Oliva, F. Y.; Lener, G.; Cámara, O. R. Enhanced Energy Storage of Alkali (Li, Na) Titanates by Sucrose Carbonization. *J. Solid State Electrochem.* **2020**. https://doi.org/10.1007/s10008-020-04567-5.

(27) Xiao, J.; Han, J.; Zhang, C.; Ling, G.; Kang, F.; Yang, Q. H. Dimensionality, Function and Performance of Carbon Materials in Energy Storage Devices. *Advanced Energy Materials*. **2022**.

https://doi.org/10.1002/aenm.202100775.

(28) Jin, Y. C.; Lin, C. Y.; Duh, J. G. Improving Rate Capability of High Potential $LiNi_{0.5}Mn_{1.5}O_{4-x}$ Cathode Materials via Increasing Oxygen Non-Stoichiometries. *Electrochim. Acta.* **2012**. https://doi.org/10.1016/j.electacta.2012.02.022.

(29) Tang, Z. K.; Xue, Y. F.; Teobaldi, G.; Liu, L. M. The Oxygen Vacancy in Li-Ion Battery Cathode Materials. *Nanoscale Horizons*. 2020. https://doi.org/10.1039/d0nh00340a.

(30) Armstrong, A. R.; Holzapfel, M.; Nová, P.; Johnson, C. S.; Kang, S.-H.; Thackeray, M. M.; Bruce, P. G. Demonstrating Oxygen Loss and Associated Structural Reorganization in the Lithium Battery Cathode $Li[Ni_{0.2}Li_{0.2}Mn_{0.6}]O_2$. **2006**. https://doi.org/10.1021/ja062027.

(31) Lu, Z.; Dahn, J. R. Understanding the Anomalous Capacity of $Li/Li/Ni_xLi_{(1/3-2x/3)}Mn_{(2/3-x/3)}O_2$ Cells Using In Situ X-Ray Diffraction and Electrochemical Studies. *J. Electrochem. Soc.* **2002**. https://doi.org/10.1149/1.1480014.

(32) Shin, J. Y.; Joo, J. H.; Samuelis, D.; Maier, J. Oxygen-Deficient $TiO_{2-\delta}$ Nanoparticles via Hydrogen Reduction for High Rate Capability Lithium Batteries. *Chem. Mater.* **2012**. https://doi.org/10.1021/cm2031009.

(33) Li, Y.; Chang, K.; Tang, H.; Li, B.; Qin, Y.; Hou, Y.; Chang, Z. Preparation of Oxygen-Deficient WO_{3-x} Nanosheets and Their Characterization as Anode Materials for High-Performance Li-Ion Batteries. *Electrochim. Acta* **2019**. https://doi.org/10.1016/j.electacta.2018.12.137.

(34) Wang, S.; Wang, Y.; Song, Y.; Jia, X.; Yang, J.; Li, Y.; Liao, J.; Song, H. Immobilizing Polysulfide via Multiple Active Sites in $W_{18}O_{49}$ for Li-S Batteries by Oxygen Vacancy Engineering. *Energy Storage Mater.* **2021**. https://doi.org/10.1016/j.ensm.2021.09.020.

(35) Wei, R.; Lu, Y.; Xu, Y. The Role of Oxygen Vacancies in Metal Oxides for Rechargeable Ion Batteries. *Science China Chemistry*. 2021. https://doi.org/10.1007/s11426-021-1103-6.

(36) Li, Y.; Zhang, Y.; Zhang, N.; Li, Y.; Wu, Y. Negative Thermal Expansion Property of $Sm_{1-X}Cu_xMnO_{3-\delta}$. *J. Mater. Res. Technol.* **2021**. https://doi.org/10.1016/j.jmrt.2021.04.027.

(37) Zhang, N.; Zhou, W.; Chao, M.; Mao, Y.; Guo, J.; Li, Y.; Feng, D.; Liang,

E. Negative Thermal Expansion, Optical and Electrical Properties of $HfMnMo_2PO_{12-\delta}$. *Ceram. Int.* **2015**. https://doi.org/10.1016/j.ceramint.2015.08.090.

(38) Cheng, Y.; Mao, Y.; Yuan, B.; Ge, X.; Guo, J.; Chao, M.; Liang, E. Enhanced Negative Thermal Expansion and Optical Absorption of $In_{0.6}(HfMg)_{0.7}Mo_3O_{12}$ with Oxygen Vacancies. *Phys. Lett. Sect. A Gen. At. Solid State Phys.* **2017**. https://doi.org/10.1016/j.physleta.2017.05.002.

(39) Marinkovic, B. A.; Moreno, E.; Almeida, T.; Johnson, M. B.; Paraguassu, W.; White, M. A. Enhanced Structure Flexibility in Oxygen-Deficient Open Framework $Al_2W_3O_{12}$: Evidence from Heat Capacity and High-Pressure Raman Spectroscopy. *J. Solid State Chem.* **2025**. https://doi.org/10.1016/j.jssc.2025.125478.

(40) Gil-Londoño, J.; Krambrock, K.; Magno Paiva, V.; Cremona, M.; R. J. Barreto, A.; D'Elia, E.; Marinkovic, B. A. Uncovering Photocatalytic Mechanisms of $Al_2W_3O_{12}$: From a Low-Positive Thermal Expansion Ceramic to an Efficient Visible-Light-Driven Photocatalyst. *Ind. Eng. Chem. Res.* **2025**. https://doi.org/10.1021/acs.iecr.5c01399.

(41) Moreno Diaz, E. C.; Maia Da Costa, M. E.; Paraguassu, W.; Krambrock, K.; Dosen, A.; Johnson, M. B.; White, M. A.; Marinkovic, B. A. Extrinsic Point Defects in Low-Positive Thermal Expansion $Al_2W_3O_{12}$ and Their Effects on Thermal and Optical Properties. *Inorg. Chem.* **2022**. https://doi.org/10.1021/acs.inorgchem.2c02113.

(42) Gil-Londoño, J.; Cremona, M.; Krambrock, K.; Rossi, A. L.; Pires Gonçalves, R.; Barreto, A. R. J.; Morais Sinimbu, L. I.; Paiva de Araújo, M. E.; Mančić, L.; Mello, A.; Marinkovic, B. A. Unraveling the Role of F-Type Color Centers on the Optical and Electrical Properties of $Al_2W_3O_{12}$ Nanoparticles with Different Content of Oxygen Vacancies. *J. Phys. Chem. C.* **2025**. https://doi.org/10.1021/acs.jpcc.4c06098.

(43) Vaalma, C.; Buchholz, D.; Weil, M.; Passerini, S. A Cost and Resource Analysis of Sodium-Ion Batteries. *Nat. Rev. Mater.* **2018**. https://doi.org/10.1038/natrevmats.2018.13

(44) Tarascon, J.-M.; Armand, M. Issues and Challenges Facing Rechargeable Lithium Batteries. **2001**. https://doi.org/10.1038/35104644.

(45) Demirocak, D. E.; Srinivasan, S. S.; Stefanakos, E. K. A Review on

Nanocomposite Materials for Rechargeable Li-Ion Batteries. *Appl. Sci.* **2017**. https://doi.org/10.3390/app7070731.

(46) Väyrynen, A.; Salminen, J. Lithium Ion Battery Production. *J. Chem. Thermodyn.* **2012**. https://doi.org/10.1016/j.jct.2011.09.005.

(47) Bhatt, M. D.; O'Dwyer, C. Recent Progress in Theoretical and Computational Investigations of Li-Ion Battery Materials and Electrolytes. *Phys. Chem. Chem. Phys.* **2015**. https://doi.org/10.1039/c4cp05552g.

(48) Winslow, K. M.; Laux, S. J.; Townsend, T. G. A Review on the Growing Concern and Potential Management Strategies of Waste Lithium-Ion Batteries. *Resour. Conserv. Recycl.* **2018**. https://doi.org/10.1016/j.resconrec.2017.11.001.

(49) Chagnes, A.; Pospiech, B. A Brief Review on Hydrometallurgical Technologies for Recycling Spent Lithium-Ion Batteries. *J. Chem. Technol. Biotechnol.* **2013**. https://doi.org/10.1002/jctb.4053.

(50) Aravindan, V.; Gnanaraj, J.; Madhavi, S.; Liu, H. K. Lithium-Ion Conducting Electrolyte Salts for Lithium Batteries. *Chem. - A Eur. J.* **2011**. https://doi.org/10.1002/chem.201101486.

(51) Yang, W.; Huang, R.; Ni, Z.; Cheng, H.; Zhou, S.; Wang, Y.; Li, X.; Zhang, Y.; Zhang, Y. Application and Research of Current Collector for Lithium-Sulfur Battery. *Ionics (Kiel).* **2022**. https://doi.org/10.1007/s11581-022-04461-2.

(52) Shi, Y.; Zhou, X.; Yu, G. Material and Structural Design of Novel Binder Systems for High-Energy, High-Power Lithium-Ion Batteries. *Acc. Chem. Res.* **2017**. https://doi.org/10.1021/acs.accounts.7b00402.

(53) Li, H.; Wang, Z.; Chen, L.; Huang, X. Research on Advanced Materials for Li-Ion Batteries. *Advanced Materials*. **2009**. https://doi.org/10.1002/adma.200901710.

(54) Winter, M.; Brodd, R. J. What Are Batteries, Fuel Cells, and Supercapacitors? *Chem. Rev.* **2004**. https://doi.org/10.1021/cr020730k.

(55) Jabbour, L.; Bongiovanni, R.; Chaussy, D.; Gerbaldi, C.; Beneventi, D. Cellulose-Based Li-Ion Batteries: A Review. *Cellulose*. **2013**. https://doi.org/10.1007/s10570-013-9973-8.

(56) Eftekhari, A. On the Theoretical Capacity/Energy of Lithium Batteries and Their Counterparts. *ACS Sustain. Chem. Eng.* **2019**.

https://doi.org/10.1021/acssuschemeng.7b04330.

(57) Liu, Y.; Wu, L. Recent Advances of Cathode Materials for Zinc-Ion Hybrid Capacitors. *Nano Energy*. **2023**. https://doi.org/10.1016/j.nanoen.2023.108290.

(58) Eftekhari, A. Lithium-Ion Batteries with High Rate Capabilities. *ACS Sustain. Chem. Eng.* **2017**. https://doi.org/10.1021/acssuschemeng.7b00046.

(59) Borah, R.; Hughson, F. R.; Johnston, J.; Nann, T. On Battery Materials and Methods. *Mater. Today Adv.* **2020**. https://doi.org/10.1016/j.mtadv.2019.100046.

(60) Liu, Q.; Su, X.; Lei, D.; Qin, Y.; Wen, J.; Guo, F.; Wu, Y. A.; Rong, Y.; Kou, R.; Xiao, X.; Aguesse, F.; Bareño, J.; Ren, Y.; Lu, W.; Li, Y. Approaching the Capacity Limit of Lithium Cobalt Oxide in Lithium Ion Batteries via Lanthanum and Aluminium Doping. *Nat. Energy* **2018**. https://doi.org/10.1038/s41560-018-0180-6.

(61) Nitta, N.; Wu, F.; Lee, J. T.; Yushin, G. Li-Ion Battery Materials: Present and Future. *Materials Today*. **2015**. https://doi.org/10.1016/j.mattod.2014.10.040.

(62) Martha, S. K.; Haik, O.; Zinigrad, E.; Exnar, I.; Drezen, T.; Miners, J. H.; Aurbach, D. On the Thermal Stability of Olivine Cathode Materials for Lithium-Ion Batteries. *J. Electrochem. Soc.* **2011**. https://doi.org/10.1149/1.3622849.

(63) Xu, J.; Thomas, H. R.; Francis, R. W.; Lum, K. R.; Wang, J.; Liang, B. A Review of Processes and Technologies for the Recycling of Lithium-Ion Secondary Batteries. *Journal of Power Sources*. **2008**. https://doi.org/10.1016/j.jpowsour.2007.11.074.

(64) Gaines, L. The Future of Automotive Lithium-Ion Battery Recycling: Charting a Sustainable Course. *Sustain. Mater. Technol.* **2014**. https://doi.org/10.1016/j.susmat.2014.10.001.

(65) Soge, A. O.; Willoughby, A. A.; Dairo, O. F.; Onatoyinbo, O. O. Cathode Materials for Lithium-Ion Batteries: A Brief Review. *Journal of New Materials for Electrochemical Systems*. **2021**. https://doi.org/10.14447/jnmes.v24i4.a02.

(66) Masquelier, C.; Croguennec, L. Polyanionic (Phosphates, Silicates, Sulfates) Frameworks as Electrode Materials for Rechargeable Li (or Na) Batteries.

Chemical Reviews. **2013**. https://doi.org/10.1021/cr3001862.

(67) Cho, J.; Kim, Y.; Kim, B.; Lee, J.; Park, B. A Breakthrough in the Safety of Lithium Secondary Batteries by Coating the Cathode Material with $AlPO_4$ Nanoparticles. *Angew. Chemie.* **2003**. https://doi.org/10.1002/ange.200250452.

(68) Lee, M. J.; Lee, S.; Oh, P.; Kim, Y.; Cho, J. High Performance LiMn2O4 Cathode Materials Grown with Epitaxial Layered Nanostructure for Li-Ion Batteries. *Nano Lett.* **2014**. https://doi.org/10.1021/nl404430e.

(69) Yamada, A.; Chung, S. C.; Hinokuma, K. Optimized $LiFePO_4$ for Lithium Battery Cathodes. *J. Electrochem. Soc.* **2001**. https://doi.org/10.1149/1.1348257.

(70) Osiak, M.; Geaney, H.; Armstrong, E.; O'Dwyer, C. Structuring Materials for Lithium-Ion Batteries: Advancements in Nanomaterial Structure, Composition, and Defined Assembly on Cell Performance. *J. Mater. Chem. A.* **2014**. https://doi.org/10.1039/c4ta00534a.

(71) Nzereogu, P. U.; Omah, A. D.; Ezema, F. I.; Iwuoha, E. I.; Nwanya, A. C. Anode Materials for Lithium-Ion Batteries: A Review. *Appl. Surf. Sci. Adv.* **2022**. https://doi.org/10.1016/j.apsadv.2022.100233.

(72) Speirs, J.; Contestabile, M.; Houari, Y.; Gross, R. The Future of Lithium Availability for Electric Vehicle Batteries. *Renew. Sustain. Energy Rev.* **2014**. https://doi.org/10.1016/j.rser.2014.04.018.

(73) Su, L.; Jing, Y.; Zhou, Z. Li Ion Battery Materials with Core-Shell Nanostructures. *Nanoscale.* **2011**. https://doi.org/10.1039/c1nr10550g.

(74) Li, X.; Kersey-Bronec, F. E.; Ke, J.; Cloud, J. E.; Wang, Y.; Ngo, C.; Pylypenko, S.; Yang, Y. Study of Lithium Silicide Nanoparticles as Anode Materials for Advanced Lithium Ion Batteries. *ACS Appl. Mater. Interfaces* **2017**. https://doi.org/10.1021/acsami.6b16773.

(75) Raić, M.; Mikac, L.; Marić, I.; Štefanić, G.; Škrabić, M.; Gotić, M.; Ivanda, M. Nanostructured Silicon as Potential Anode Material for Li-Ion Batteries. *Molecules.* **2020**. https://doi.org/10.3390/molecules25040891.

(76) Miller, W.; Smith, C. W.; MacKenzie, D. S.; Evans, K. E. Negative Thermal Expansion: A Review. *J. Mater. Sci.* **2009**. https://doi.org/10.1007/s10853-009-3692-4.

(77) Liu, H.; Sun, W.; Zhang, Z.; Lovings, L.; Lind, C. Thermal Expansion

Behavior in the $A_2M_3O_{12}$ Family of Materials. *Solids*. **2021**. https://doi.org/10.3390/solids2010005.

(78) Attfield, P. J. Mechanisms and Materials for NTE. *Front. Chem.* **2018**. https://doi.org/10.3389/fchem.2018.00371.

(79) Sumithra, S.; Umarji, A. M. Hygroscopicity and Bulk Thermal Expansion in $Y_2W_3O_{12}$. *Mater. Res. Bull.* **2005**. https://doi.org/10.1016/j.materresbull.2004.09.009.

(80) Liu, H.; Sun, W.; Zhang, Z.; Zhou, M.; Meng, X.; Zeng, X. Tailorable Thermal Expansion and Hygroscopic Properties of Cerium-Substituted $Y_2W_3O_{12}$ Ceramics. *J. Alloys Compd.* **2018**. https://doi.org/10.1016/j.jallcom.2018.04.081.

(81) Woodcock, D. A.; Lightfoot, P.; Ritter, C. Negative Thermal Expansion in $Y_2(WO_4)_3$; **2000**. https://doi.org/https://doi.org/10.1006/jssc.1999.8502.

(82) Varga, T.; Wilkinson, A. P.; Lind, C.; Bassett, W. A.; Zha, C. S. High Pressure Synchrotron X-Ray Powder Diffraction Study of $Sc_2Mo_3O_{12}$ and $Al_2W_3O_{12}$. *J. Phys. Condens. Matter*. **2005**. https://doi.org/10.1088/0953-8984/17/27/004.

(83) Mirsadeghi, S.; Zandavar, H.; Rahimi, M.; Tooski, H. F.; Rajabi, H. R.; Rahimi-Nasrabadi, M.; Sohouli, E.; Larijani, B.; Pourmortazavi, S. M. Photocatalytic Reduction of Imatinib Mesylate and Imipenem on Electrochemical Synthesized $Al_2W_3O_{12}$ Nanoparticle: Optimization, Investigation of Electrocatalytic and Antimicrobial Activity. *Colloids Surfaces A Physicochem. Eng. Asp.* **2020**. https://doi.org/10.1016/j.colsurfa.2019.124254.

(84) Pontón, P. I.; Prisco, L. P.; Marinkovic, B. A. Effects of Low Contents of $A_2M_3O_{12}$ Submicronic Thermomiotic-like Fillers on Thermal Expansion and Mechanical Properties of HDPE-Based Composites. *Polym. Compos.* **2018**. https://doi.org/10.1002/pc.24811.

(85) Costa, I. M.; Blair, V. L.; Paraguassu, W.; Marinkovic, B. A. Evaluating $Al_{2-x}Ga_xW_3O_{12}$ System for Thermal Shock Resistance. *J. Solid State Chem.* **2019**. https://doi.org/10.1016/j.jssc.2019.05.041.

(86) Cortés, A. E. C.; Dosen, A.; Blair, V. L.; Johnson, M. B.; White, M. A.; Marinkovic, B. A. Phase Transition and Coefficients of Thermal Expansion in $Al_{2-x}In_xW_3O_{12}$ ($0.2 \leq x \leq 1$). *Materials (Basel).* **2021**.

https://doi.org/10.3390/ma14144021.

(87) Li, F.; Liu, X.; Song, W.; Yuan, B.; Cheng, Y.; Yuan, H.; Cheng, F.; Chao, M.; Liang, E. Phase Transition, Crystal Water and Low Thermal Expansion Behavior of $Al_{2-2x}(ZrMg)_xW_3O_{12}\cdot n(H_2O)$. *J. Solid State Chem.* **2014**. https://doi.org/10.1016/j.jssc.2014.06.009.

(88) Dasgupta, N.; Sörge, E.; Butler, B.; Wen, T. C.; Shetty, D. K.; Cambrea, L. R.; Harris, D. C. Synthesis and Characterization of $Al_{2-x}Sc_x(WO_4)_3$ Ceramics for Low-Expansion Infrared-Transmitting Windows. *J. Mater. Sci.* **2012**. https://doi.org/10.1007/s10853-012-6548-2.

(89) Yanase, I.; Ootomo, R.; Kobayashi, H. Effect of B Substitution on Thermal Changes of UV–Vis and Raman Spectra and Color of $Al_2W_3O_{12}$ Powder. *J. Therm. Anal. Calorim.* **2018**. https://doi.org/10.1007/s10973-017-6933-9.

(90) Rudolph, P. Fundamentals and Engineering of Defects. *Prog. Cryst. Growth Charact. Mater.* **2016**. https://doi.org/10.1016/j.pcrysgrow.2016.04.004.

(91) Tuller, H. L.; Bishop, S. R. Point Defects in Oxides: Tailoring Materials through Defect Engineering. *Annu. Rev. Mater. Res.* **2011**. https://doi.org/10.1146/annurev-matsci-062910-100442.

(92) Ricca, C.; Aschauer, U. Mechanisms for Point Defect-Induced Functionality in Complex Perovskite Oxides. *Appl. Phys. A Mater. Sci. Process.* **2022**. https://doi.org/10.1007/s00339-022-06210-8.

(93) Zhao, M.; Pan, W.; Wan, C.; Qu, Z.; Li, Z.; Yang, J. Defect Engineering in Development of Low Thermal Conductivity Materials: A Review. *J. Eur. Ceram. Soc.* **2017**. https://doi.org/10.1016/j.jeurceramsoc.2016.07.036.

(94) Wang, Y.; Xiao, X.; Li, Q.; Pang, H. Synthesis and Progress of New Oxygen-Vacant Electrode Materials for High-Energy Rechargeable Battery Applications. *Small*. **2018**. https://doi.org/10.1002/smll.201802193.

(95) Liu, Q.; Wang, F.; Lin, H.; Xie, Y.; Tong, N.; Lin, J.; Zhang, X.; Zhang, Z.; Wang, X. Surface Oxygen Vacancy and Defect Engineering of WO_3 for Improved Visible Light Photocatalytic Performance. *Catal. Sci. Technol.* **2018**. https://doi.org/10.1039/c8cy00994e.

(96) TONG, H. xia; CHEN, Q. yuan; YIN, Z. lan; HU, H. ping; WU, D. xin; YANG, Y. hui. Preparation, Characterization and Photo-Catalytic Behavior of WO_3-TiO_2 Catalysts with Oxygen Vacancies. *Trans. Nonferrous Met. Soc. China.* **2009**.https://doi.org/10.1016/S1003-6326(09)60056-X.

(97) Wang, G.; Yang, Y.; Ling, Y.; Wang, H.; Lu, X.; Pu, Y. C.; Zhang, J. Z.; Tong, Y.; Li, Y. An Electrochemical Method to Enhance the Performance of Metal Oxides for Photoelectrochemical Water Oxidation. *J. Mater. Chem. A* **2016**. https://doi.org/10.1039/c5ta10477g.

(98) Li, G.; Blake, G. R.; Palstra, T. T. M. Vacancies in Functional Materials for Clean Energy Storage and Harvesting: The Perfect Imperfection. *Chem. Soc. Rev.* **2017**. https://doi.org/10.1039/c6cs00571c.

(99) Zhang, C.; Liu, G.; Geng, X.; Wu, K.; Debliquy, M. Metal Oxide Semiconductors with Highly Concentrated Oxygen Vacancies for Gas Sensing Materials: A Review. *Sensors Actuators, A Phys.* **2020**. https://doi.org/10.1016/j.sna.2020.112026.

(100) Drouilly, C.; Krafft, J. M.; Averseng, F.; Casale, S.; Bazer-Bachi, D.; Chizallet, C.; Lecocq, V.; Vezin, H.; Lauron-Pernot, H.; Costentin, G. ZnO Oxygen Vacancies Formation and Filling Followed by in Situ Photoluminescence and in Situ EPR. *J. Phys. Chem. C.* **2012**. https://doi.org/10.1021/jp307693y.

(101) Lv, Y.; Yao, W.; Zong, R.; Zhu, Y. Fabrication of Wide-Range-Visible Photocatalyst Bi_2WO_{6-x} Nanoplates via Surface Oxygen Vacancies. *Sci. Rep.* **2016**. https://doi.org/10.1038/srep19347.

(102) Ji, Q.; Bi, L.; Zhang, J.; Cao, H.; Zhao, X. S. The Role of Oxygen Vacancies of ABO_3 perovskite Oxides in the Oxygen Reduction Reaction. *Energy Environ. Sci.* **2020**. https://doi.org/10.1039/d0ee00092b.

(103) Xiong, F.; Tan, S.; Yao, X.; An, Q.; Mai, L. Crystal Defect Modulation in Cathode Materials for Non-Lithium Ion Batteries: Progress and Challenges. *Materials Today*. **2021**. https://doi.org/10.1016/j.mattod.2020.12.002.

(104) Li, Z.; Dong, Y.; Feng, J.; Xu, T.; Ren, H.; Gao, C.; Li, Y.; Cheng, M.; Wu, W.; Wu, M. Controllably Enriched Oxygen Vacancies through Polymer Assistance in Titanium Pyrophosphate as a Super Anode for Na/K-Ion Batteries. *ACS Nano.* **2019**. https://doi.org/10.1021/acsnano.9b03686.

(105) Xu, Y.; Zhou, M.; Wang, X.; Wang, C.; Liang, L.; Grote, F.; Wu, M.; Mi, Y.; Lei, Y. Enhancement of Sodium Ion Battery Performance Enabled by Oxygen Vacancies. *Angew. Chemie.* **2015**. https://doi.org/10.1002/ange.201503477.

(106) Bai, Y. L.; Xarapatgvl, R.; Wu, X. Y.; Liu, X.; Liu, Y. S.; Wang, K. X.;

Chen, J. S. Core-Shell Anatase Anode Materials for Sodium-Ion Batteries: The Impact of Oxygen Vacancies and Nitrogen-Doped Carbon Coating. *Nanoscale.* **2019**. https://doi.org/10.1039/c9nr06245a.

(107) Zhang, X.; Huang, Y.; Wu, S.; Zeng, Y.; Yu, M.; Cheng, F.; Lu, X.; Tong, Y. Engineering Oxygen-Deficient $Na_2Ti_3O_7$ Nanobelt Arrays on Carbon Cloth as Advanced Flexible Anodes for Sodium-Ion Batteries. *Wuli Huaxue Xuebao/ Acta Phys. - Chim. Sin.* **2018**. https://doi.org/10.3866/PKU.WHXB201707173.

(108) Sun, Y.; Cong, H.; Zan, L.; Zhang, Y. Oxygen Vacancies and Stacking Faults Introduced by Low-Temperature Reduction Improve the Electrochemical Properties of Li_2MnO_3 Nanobelts as Lithium-Ion Battery Cathodes. *ACS Appl. Mater. Interfaces.* **2017**. https://doi.org/10.1021/acsami.7b12080.

(109) Mizokawa, T.; Wakisaka, Y.; Sudayama, T.; Iwai, C.; Miyoshi, K.; Takeuchi, J.; Wadati, H.; Hawthorn, D. G.; Regier, T. Z.; Sawatzky, G. A. Role of Oxygen Holes in Li_xCoO_2 Revealed by Soft X-Ray Spectroscopy. *Phys. Rev. Lett.* **2013**. https://doi.org/10.1103/PhysRevLett.111.056404.

(110) Li, L.; Zhang, D.; Deng, J.; Gou, Y.; Fang, J.; Cui, H.; Zhao, Y.; Cao, M. Carbon-Based Materials for Fast Charging Lithium-Ion Batteries. *Carbon N. Y.* **2021**. https://doi.org/10.1016/j.carbon.2021.07.053.

(111) Tolganbek, N.; Yerkinbekova, Y.; Kalybekkyzy, S.; Bakenov, Z.; Mentbayeva, A. Current State of High Voltage Olivine Structured $LiMPO_4$ Cathode Materials for Energy Storage Applications: A Review. *J. Alloys Compd.* **2021**. https://doi.org/10.1016/j.jallcom.2021.160774.

(112) Wu, X.; Rohman, F.; Meledina, M.; Tempel, H.; Schierholz, R.; Kungl, H.; Mayer, J.; Eichel, R. A. Analysis of the Effects of Different Carbon Coating Strategies on Structure and Electrochemical Behavior of $LiCoPO_4$ Material as a High-Voltage Cathode Electrode for Lithium Ion Batteries. *Electrochim. Acta* **2018**. https://doi.org/10.1016/j.electacta.2018.05.067.

(113) Can, F.; Courtois, X.; Duprez, D. Tungsten-based Catalysts for Environmental Applications. *Catalysts*. **2021**. https://doi.org/10.3390/catal11060703.

(114) Gong, Y.; Zheng, F.; Dong, J.; An, P.; Yang, D.; Guo, Z.; Li, H.; Li, Y.; Li, X. Structural Changes in Hexagonal WO_3 under High Pressure. *J. Alloys Compd.* **2019**. https://doi.org/10.1016/j.jallcom.2019.05.132.

(115) Boruah, P. J.; Khanikar, R. R.; Bailung, H. Synthesis and Characterization of Oxygen Vacancy Induced Narrow Bandgap Tungsten Oxide (WO_{3-x}) Nanoparticles by Plasma Discharge in Liquid and Its Photocatalytic Activity. *Plasma Chem. Plasma Process.* **2020**. https://doi.org/10.1007/s11090-020-10073-3.

(116) Murai, M.; Iba, S.; Ota, H.; Takai, K. Azulene-Fused Linear Polycyclic Aromatic Hydrocarbons with Small Bandgap, High Stability, and Reversible Stimuli Responsiveness. *Org. Lett.* **2017**. https://doi.org/10.1021/acs.orglett.7b02729.

(117) Kaduk, J. A.; Golab, J. T. Structures of 2,6-Disubstituted Naphthalenes. *Acta Crystallogr. Sect. B Struct. Sci.* **1999**. https://doi.org/10.1107/S0108768198008945.

(118) Schutte, W. J.; De Boer, J. L.; Jellinek, F. Crystal Structures of Tungsten Disulfide and Diselenide. *journal of solid state chemistry*. **1987**.

(119) Van der Vlies, A. J.; Kishan, G.; Niemantsverdriet, J. W.; Prins, R.; Weber, T. Basic Reaction Steps in the Sulfidation of Crystalline Tungsten Oxides. *J. Phys. Chem. B.* **2002**. https://doi.org/10.1021/jp0138734.

(120) TRUCANO P.; CHEN R. Structure of Graphite by Neutron Diffraction. *Nature*. **1975**. https://doi.org/https://doi.org/10.1038/258136a0.

(121) Losic, D.; Farivar, F.; Yap, P. L.; Karami, A. Accounting Carbonaceous Counterfeits in Graphene Materials Using the Thermogravimetric Analysis (TGA) Approach. *Anal. Chem.* **2021**. https://doi.org/10.1021/acs.analchem.1c02662.

(122) Farivar, F.; Yap, P. L.; Karunagaran, R. U.; Losic, D. Thermogravimetric Analysis (TGA) of Graphene Materials: Effect of Particle Size of Graphene, Graphene Oxide and Graphite on Thermal Parameters. *J. Carbon Res.* **2021**, https://doi.org/10.3390/c7020041.

(123) Han, F. D.; Bai, Y. J.; Liu, R.; Yao, B.; Qi, Y. X.; Lun, N.; Zhang, J. X. Template-Free Synthesis of Interconnected Hollow Carbon Nanospheres for High-Performance Anode Material in Lithium-Ion Batteries. *Adv. Energy Mater.* **2011**. https://doi.org/10.1002/aenm.201100340.

(124) Guo, B.; Liu, Q.; Chen, E.; Zhu, H.; Fang, L.; Gong, J. R. Controllable N-Doping of Graphene. *Nano Lett.* **2010**. https://doi.org/10.1021/nl103079j.

(125) Robertson, J. Diamond-like Amorphous Carbon. *Reports: Areview journal*.

2002. https://doi.org/10.1016/S0927-796X(02)00005-0

(126) Paraguassu, W.; Maczka, M.; Filho, A. G. S.; Freire, P. T. C.; Melo, F. E. A.; Filho, J. M.; Hanuza, J. A Comparative Study of Negative Thermal Expansion Materials $Sc_2(MoO_4)_3$ and $Al_2(WO_4)_3$ Crystals. *Vib. Spectrosc.* **2007**. https://doi.org/10.1016/j.vibspec.2006.08.006.

(127) Sundberg, J.; Nyberg, H.; Särhammar, E.; Nyberg, T.; Jacobson, S.; Jansson, U. Influence of Composition, Structure and Testing Atmosphere on the Tribological Performance of W-S-N Coatings. *Surf. Coatings Technol.* **2014**. https://doi.org/10.1016/j.surfcoat.2014.09.061.

(128) Miakota, D. I.; Unocic, R. R.; Bertoldo, F.; Ghimire, G.; Engberg, S.; Geohegan, D.; Thygesen, K. S.; Canulescu, S. A Facile Strategy for the Growth of High-Quality Tungsten Disulfide Crystals Mediated by Oxygen-Deficient Oxide Precursors. *Materials Science*. **2022**. https://doi.org/https://doi.org/10.1039/D2NR01863B.

(129) Di Paola, A.; Palmisano, L.; Venezia, A. M.; Augugliaro, V. Coupled Semiconductor Systems for Photocatalysis. Preparation and Characterization of Polycrystalline Mixed WO_3/WS_2 Powders. *J. Phys. Chem. B.* **1999**. https://doi.org/10.1021/jp9911797.

(130) Mahler, B.; Hoepfner, V.; Liao, K.; Ozin, G. A. Colloidal Synthesis of 1T-WS_2 and 2H-WS_2 Nanosheets: Applications for Photocatalytic Hydrogen Evolution. *J. Am. Chem. Soc.* **2014**. https://doi.org/10.1021/ja506261t.

(131) Henriques, M. D. R.; Mařák, V.; Gil-Londoño, J.; Santana, V. T.; Neugebauer, P.; Drdlík, D.; Marinkovic, B. A. Extrinsic Oxygen Vacancies Formation during Crystallization of $Al_2W_3O_{12}$ by Calcination in Air. *J. Phys. Chem. C.* **2023**. https://doi.org/10.1021/acs.jpcc.3c06264.

(132) Perrozzi, F.; Emamjomeh, S. M.; Paolucci, V.; Taglieri, G.; Ottaviano, L.; Cantalini, C. Thermal Stability of WS_2 Flakes and Gas Sensing Properties of WS_2/WO_3 Composite to H_2, NH_3 and NO_2. *Sensors Actuators, B Chem.* **2017**. https://doi.org/10.1016/j.snb.2016.12.069.

(133) Yang, X. G.; Ge, S.; Liu, T.; Leng, Y.; Wang, C. Y. A Look into the Voltage Plateau Signal for Detection and Quantification of Lithium Plating in Lithium-Ion Cells. *J. Power Sources.* **2018**. https://doi.org/10.1016/j.jpowsour.2018.05.073.

(134) Schweidler, S.; De Biasi, L.; Schiele, A.; Hartmann, P.; Brezesinski, T.;

Janek, J. Volume Changes of Graphite Anodes Revisited: A Combined Operando X-Ray Diffraction and in Situ Pressure Analysis Study. *J. Phys. Chem. C* **2018**. https://doi.org/10.1021/acs.jpcc.8b01873.

(135) Fujimoto, H.; Yamaki, T.; Shimoda, K.; Fujinami, S.; Nakatani, T.; Kano, G.; Kawasaki, M.; Ogumi, Z.; Abe, T. Phase Diagram of Li-Graphite Intercalation Compound Formed by the Charge/Discharge Reaction in Li-Ion Battery. *J. Electrochem. Soc.* **2022**. https://doi.org/10.1149/1945-7111/ac7e77.

(136) Nadimpalli, S. P. V.; Sethuraman, V. A.; Dalavi, S.; Lucht, B.; Chon, M. J.; Shenoy, V. B.; Guduru, P. R. Quantifying Capacity Loss Due to Solid-Electrolyte-Interphase Layer Formation on Silicon Negative Electrodes in Lithium-Ion Batteries. *J. Power Sources* **2012**. https://doi.org/10.1016/j.jpowsour.2012.05.004.

(137) Azam, M. A.; Safie, N. E.; Ahmad, A. S.; Yuza, N. A.; Zulkifli, N. S. A. Recent Advances of Silicon, Carbon Composites and Tin Oxide as New Anode Materials for Lithium-Ion Battery: A Comprehensive Review. *J. Energy Storage* **2021**. https://doi.org/10.1016/j.est.2020.102096.

(138) Li, Z.; Tan, Y.; Huang, X.; Zhang, W.; Gao, Y.; Tang, B. Three-Dimensionally Ordered Macroporous SnO_2 as Anode Materials for Lithium Ion Batteries. *Ceram. Int.* **2016**. https://doi.org/10.1016/j.ceramint.2016.09.036.

(139) Cao, Z.; Ma, X. Encapsulated Fe_3O_4 into Tubular Mesoporous Carbon as a Superior Performance Anode Material for Lithium-Ion Batteries. *J. Alloys Compd.* **2020**. https://doi.org/10.1016/j.jallcom.2019.152542.

(140) Han, M.; Mu, Y.; Yuan, F.; Bai, X.; Yu, J. Vapor Pressure-Assisted Synthesis of Chemically Bonded TiO_2/C Nanocomposites with Highly Mesoporous Structure for Lithium-Ion Battery Anode with High Capacity, Ultralong Cycling Lifetime, and Superior Rate Capability. *J. Power Sources* **2020**. https://doi.org/10.1016/j.jpowsour.2020.228206.

(141) Yang, Y.; Yue, Y.; Wang, L.; Cheng, X.; Hu, Y.; Yang, Z. zheng; Zhang, R.; Jin, B.; Sun, R. Facile Synthesis of Mesoporous $TiNb_2O_7$/C Microspheres as Long-Life and High-Power Anodes for Lithium-Ion Batteries. *Int. J. Hydrogen Energy* **2020**. https://doi.org/10.1016/j.ijhydene.2020.02.214.

(142) Gong, Y.; Sun, L.; Si, H.; Zhang, Y.; Shi, Y.; Wu, L.; Gu, J.; Zhang, Y. MnO

Nanorods Coated by Co-Decorated N-Doped Carbon as Anodes for High Performance Lithium Ion Batteries. *Appl. Surf. Sci.* **2020**. https://doi.org/10.1016/j.apsusc.2019.144479.

(143) Tian, Q.; Chen, Y.; Zhang, F.; Zhang, W.; Sui, Z.; Yang, L. Hierarchical Carbon-Riveted 2D@0D TiO_2 Nanosheets@SnO_2 Nanoparticles Composite for a Improved Lithium-Ion Battery Anode. *Appl. Surf. Sci.* **2020**. https://doi.org/10.1016/j.apsusc.2020.145625.

(144) Liang, G.; Qin, X.; Zou, J.; Luo, L.; Wang, Y.; Wu, M.; Zhu, H.; Chen, G.; Kang, F.; Li, B. Electrosprayed Silicon-Embedded Porous Carbon Microspheres as Lithium-Ion Battery Anodes with Exceptional Rate Capacities. *Carbon N. Y.* **2018**. https://doi.org/10.1016/j.carbon.2017.11.013.

(145) Yang, X.; Rogach, A. L. Electrochemical Techniques in Battery Research: A Tutorial for Nonelectrochemists. *Advanced Energy Materials*. **2019**. https://doi.org/10.1002/aenm.201900747.

(146) Lim, Y. R.; Ko, Y.; Park, J.; Cho, W. Il; Lim, S. A.; Cha, E. H. Morphology-Controlled WO_3 and WS_2 Nanocrystals for Improved Cycling Performance of Lithium Ion Batteries. *J. Electrochem. Sci. Technol.* **2019**. https://doi.org/10.5229/JECST.2019.10.1.89.

(147) Li, Z.; Yang, X.; Yang, Y.; Li, X.; Gao, Y.; Wang, L.; Lü, W. Enhanced Li-Ion Battery Performance Based on Multisite Oxygen Vacancies in WO_{3-x}@rGO Negative Electrode. *Chem. Eng. J.* **2024**. https://doi.org/10.1016/j.cej.2024.155383.

(148) Mo, R.; Tan, X.; Li, F.; Tao, R.; Xu, J.; Kong, D.; Wang, Z.; Xu, B.; Wang, X.; Wang, C.; Li, J.; Peng, Y.; Lu, Y. Tin-Graphene Tubes as Anodes for Lithium-Ion Batteries with High Volumetric and Gravimetric Energy Densities. *Nat. Commun.* **2020**. https://doi.org/10.1038/s41467-020-14859-z.

(149) Yeom, S. J.; Lee, C.; Kang, S.; Wi, T. U.; Lee, C.; Chae, S.; Cho, J.; Shin, D. O.; Ryu, J.; Lee, H. W. Native Void Space for Maximum Volumetric Capacity in Silicon-Based Anodes. *Nano Lett.* **2019**. https://doi.org/10.1021/acs.nanolett.9b03583.

(150) Vejpravová, J. Mixed Sp^2-Sp^3 Nanocarbon Materials: A Status Quo Review. *Nanomaterials*. **2021**. https://doi.org/10.3390/nano11102469.

(151) Su, F. Y.; He, Y. B.; Li, B.; Chen, X. C.; You, C. H.; Wei, W.; Lv, W.; Yang, Q. H.; Kang, F. Could Graphene Construct an Effective Conducting Network in a High-Power Lithium Ion Battery? *Nano Energy*. **2012**. https://doi.org/10.1016/j.nanoen.2012.02.004.

(152) Su, F. Y.; You, C.; He, Y. B.; Lv, W.; Cui, W.; Jin, F.; Li, B.; Yang, Q. H.; Kang, F. Flexible and Planar Graphene Conductive Additives for Lithium-Ion Batteries. *J. Mater. Chem.* **2010**. https://doi.org/10.1039/c0jm01633k.

(153) Hölderle, T.; Monchak, M.; Baran, V.; Kriele, A.; Mühlbauer, M. J.; Dyadkin, V.; Rabenbauer, A.; Schökel, A.; Ehrenberg, H.; Müller-Buschbaum, P.; Senyshyn, A. Thermal Structural Behavior of ElectrochemicallyLithiated Graphite ($LixC_6$) Anodes in Li-Ion Batteries. *Batter. Supercaps.* **2024**. https://doi.org/10.1002/batt.202300499.

(154) Marinkovic, B. A.; Jardim, P. M.; De Avillez, R. R.; Rizzo, F. Negative Thermal Expansion in $Y_2Mo_3O_{12}$. *Solid State Sci.* **2005**. https://doi.org/10.1016/j.solidstatesciences.2005.08.012.

(155) Yan, P.; Zheng, J.; Gu, M.; Xiao, J.; Zhang, J. G.; Wang, C. M. Intragranular Cracking as a Critical Barrier for High-Voltage Usage of Layer-Structured Cathode for Lithium-Ion Batteries. *Nat. Commun.* **2017**. https://doi.org/10.1038/ncomms14101.

(156) An, Y.; Tian, Y.; Wei, C.; Zhang, Y.; Xiong, S.; Feng, J.; Qian, Y. Recent Advances and Perspectives of 2D Silicon: Synthesis and Application for Energy Storage and Conversion. *Energy Storage Materials*. **2020**. https://doi.org/10.1016/j.ensm.2020.07.006.

(157) Yi, X.; Qi, G.; Liu, X.; Depcik, C.; Liu, L. Challenges and Strategies toward Anode Materials with Different Lithium Storage Mechanisms for Rechargeable Lithium Batteries. *J. Energy Storage* **2024**. https://doi.org/10.1016/j.est.2024.112480.

(158) Shkvarina, E. G.; Titov, A. A.; Shkvarin, A. S.; Plaisier, J. R.; Gigli, L.; Titov, A. N. Thermal Stability of the Layered Modification of Cu0.5ZrTe2 in the Temperature Range 25–900 °C. *Acta Crystallogr. Sect. C Struct. Chem.* **2018**. https://doi.org/10.1107/S2053229618009841.

(159) Gupta, R.; Kumar, R.; Chauhan, R. P.; Chakarvarti, S. K. Gamma Ray Induced Modifications in Copper Microwires Synthesized Using Track-Etched Membrane. *Vacuum* **2018**.

https://doi.org/10.1016/j.vacuum.2017.11.031.

(160) Li, Z.; Yang, W.; Xie, L.; Li, Y.; Liu, Y.; Sun, Y.; Bu, Y.; Mi, X.; Zhan, S.; Hu, W. Prominent Role of Oxygen Vacancy for Superoxide Radical and Hydroxyl Radical Formation to Promote Electro-Fenton like Reaction by W-Doped CeO_2 Composites. *Appl. Surf. Sci.* **2021**. https://doi.org/10.1016/j.apsusc.2021.149262.

(161) Sarwan, B.; Pare, B.; Acharya, A. D. The Effect of Oxygen Vacancies on the Photocatalytic Activity of BiOCl Nanocrystals Prepared by Hydrolysis and UV Light Irradiation. *Mater. Sci. Semicond. Process.* **2014**. https://doi.org/10.1016/j.mssp.2013.09.015.

(162) Cho, J. M.; Yun, W. J.; Lee, J. K.; Lee, H. S.; So, W. W.; Moon, S. J.; Jia, Y.; Kulkarni, H.; Wu, Y. Electron Spin Resonance from Annealed Titania Nanotubes. *Appl. Phys. A Mater. Sci. Process.* **2007**. https://doi.org/10.1007/s00339-007-4063-0.

(163) Almeida, L. A.; Viol, J.; Cremona, M.; Menezes, F. A. F.; Guimarães, A. O.; Llorca, J.; Marinkovic, B. A. Enhanced Photocatalytic Activity of TiO_2 Anatase Nanoparticles Modified with Malonic Acid under Reduced Power Visible Light: Synthesis, Characterization and Degradation of Tetracycline and Chlorophenol. *J. Photochem. Photobiol. A Chem.* **2024**. https://doi.org/10.1016/j.jphotochem.2024.115617.

(164) Wang, Y.; Shao, X.; Xu, H.; Xie, M.; Deng, S.; Wang, H.; Liu, J.; Yan, H. Facile Synthesis of Porous $LiMn_2O_4$ Spheres as Cathode Materials for High-Power Lithium Ion Batteries. *J. Power Sources.* **2013**. https://doi.org/10.1016/j.jpowsour.2012.10.077.

(165) Qian, J.; Zhou, M.; Cao, Y.; Ai, X.; Yang, H. Template-Free Hydrothermal Synthesis of Nanoembossed Mesoporous $LiFePO_4$ Microspheres for High-Performance Lithium-Ion Batteries. *J. Phys. Chem. C.* **2010**. https://doi.org/10.1021/jp912102k.

(166) Kuo, C. K.; Lin, M. C.; Liu, W. R. Effects of Oxygen Vacancy Concentration and Sintering Temperature on Rechargeable Li-Ion Storage Performance of Titanium Niobate Anode Materials. *Ceram. Int.* **2023**. https://doi.org/10.1016/j.ceramint.2022.10.176.

(167) Esteve-Adell, I.; Porcel-Valenzuela, M.; Zubizarreta, L.; Gil-Agustí, M.; García-Pellicer, M.; Quijano-Lopez, A. Influence of the Specific Surface

Area of Graphene Nanoplatelets on the Capacity of Lithium-Ion Batteries. *Front. Chem.* **2022**. https://doi.org/10.3389/fchem.2022.807980.

(168) Lee, S.; Jin, W.; Kim, S. H.; Joo, S. H.; Nam, G.; Oh, P.; Kim, Y.; Kwak, S. K.; Cho, J. Oxygen Vacancy Diffusion and Condensation in Lithium-Ion Battery Cathode Materials. *Angew. Chemie* **2019**. https://doi.org/10.1002/ange.201904469.

(169) Hao, X.; Lin, X.; Lu, W.; Bartlett, B. M. Oxygen Vacancies Lead to Loss of Domain Order, Particle Fracture, and Rapid Capacity Fade in Lithium Manganospinel ($LiMn_2O_4$) Batteries. *ACS Applied Materials and Interfaces*. **2014**. https://doi.org/10.1021/am500671e.

(170) Feng, L.; Liu, Y.; Wu, L.; Qin, W.; Yang, Z.; Liu, J. Surface Modification with Oxygen Vacancy in $LiNi_{0.5}Co_{0.2}Mn_{0.3}O_2$ for Lithium-Ion Batteries. *J. Alloys Compd.* **2021**. https://doi.org/10.1016/j.jallcom.2021.160626.

(171) Sharma, N.; Peterson, V. K.; Elcombe, M. M.; Avdeev, M.; Studer, A. J.; Blagojevic, N.; Yusoff, R.; Kamarulzaman, N. Structural Changes in a Commercial Lithium-Ion Battery during Electrochemical Cycling: An in Situ Neutron Diffraction Study. *J. Power Sources* **2010**. https://doi.org/10.1016/j.jpowsour.2010.06.114.

Appendix: Supplementary material

S1.

Photos of the three $Al_2W_3O_{12}$ powders illustrating their colors.

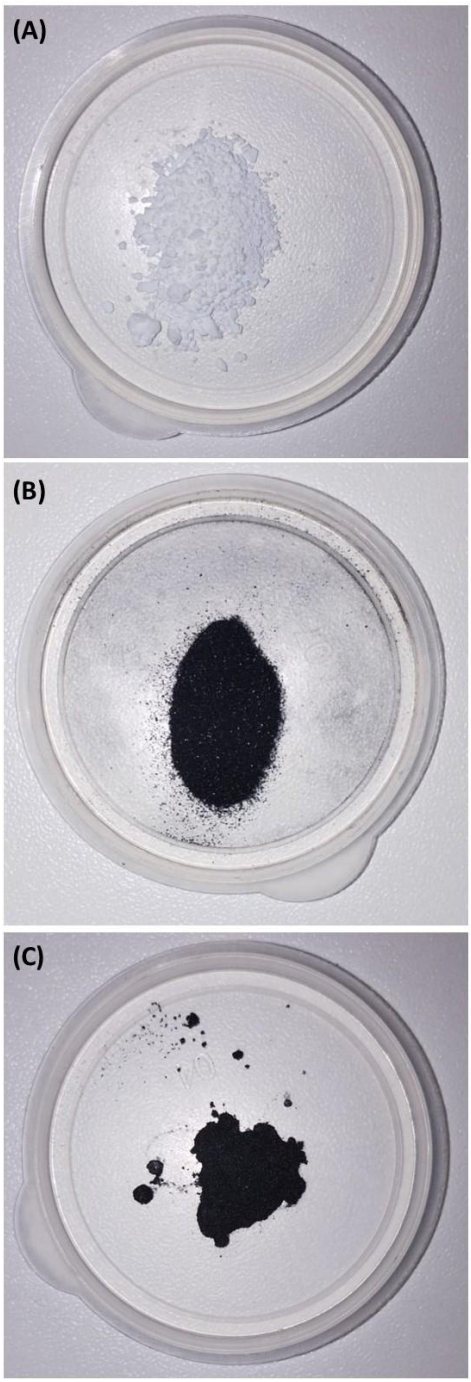

Figure S1. Photos of S800 (A), SC700 (B), and S800G(3:5) (C) samples.

S2.

XRPD patterns with Le Bail fits

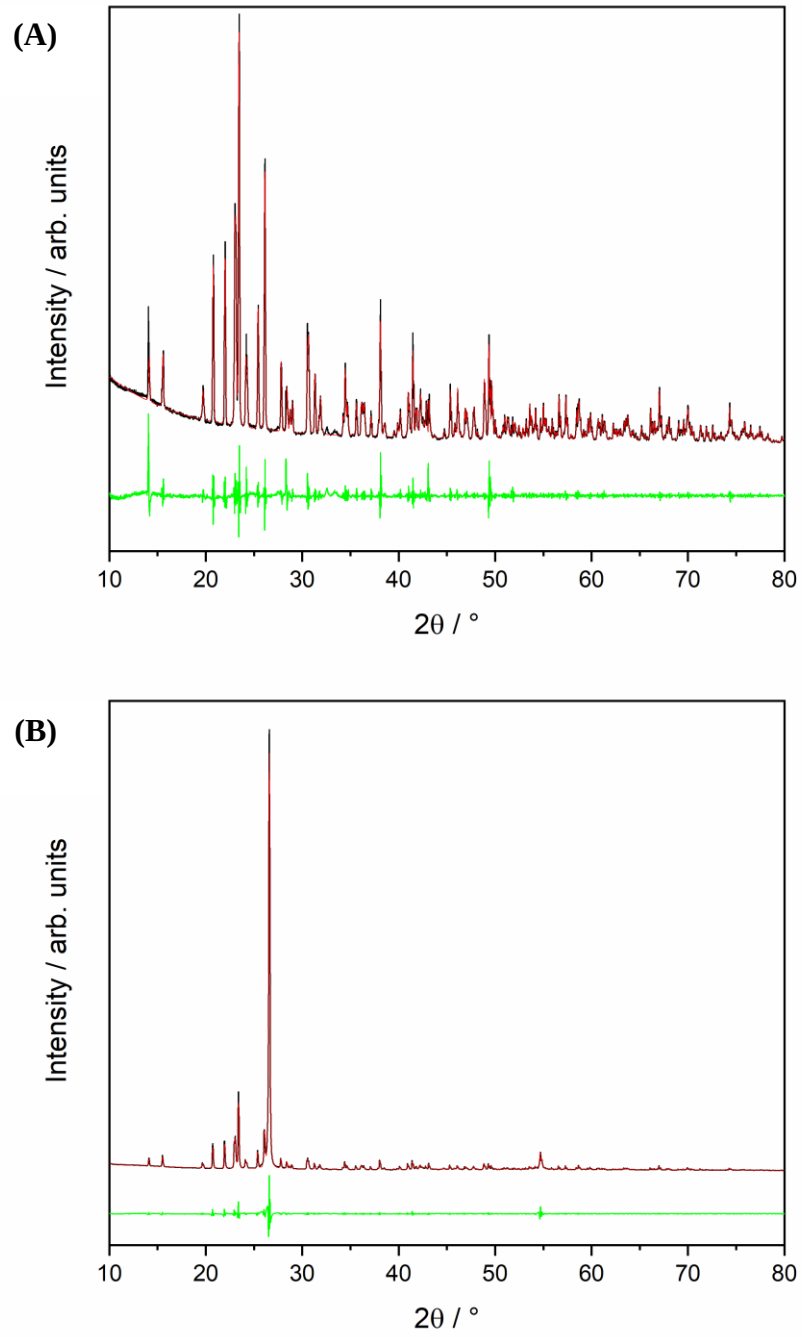

Figure S2. XRPD patterns of S800 (A) and S800G(3:5) (B) showing the Le Bail fits. The experimental data are represented by black lines, the calculated profiles by red lines, and the difference profiles by green lines.

S3.

SEM image of pristine graphite

(A)

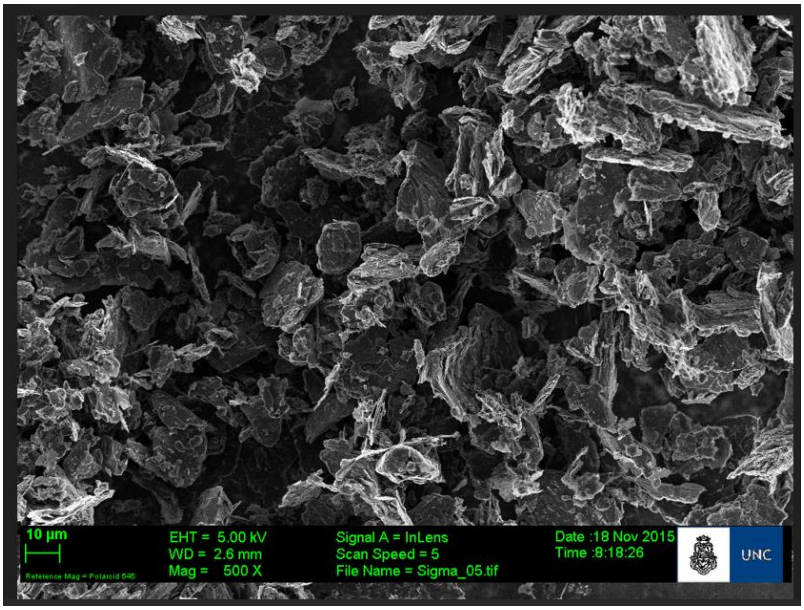

(B)

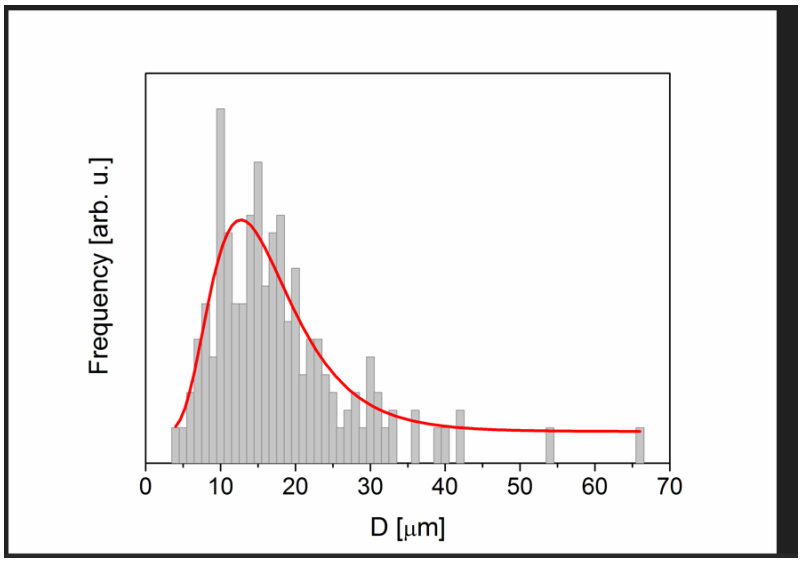

Figure S3. SEM image of pristine graphite (A) and particle size distribution of graphite obtained from SEM images with log-normal fitting (B).

S4.

Thermogravimetric analysis from 100 to 1000 ºC at a heating rate of 10 ºC min^{-1} in air.

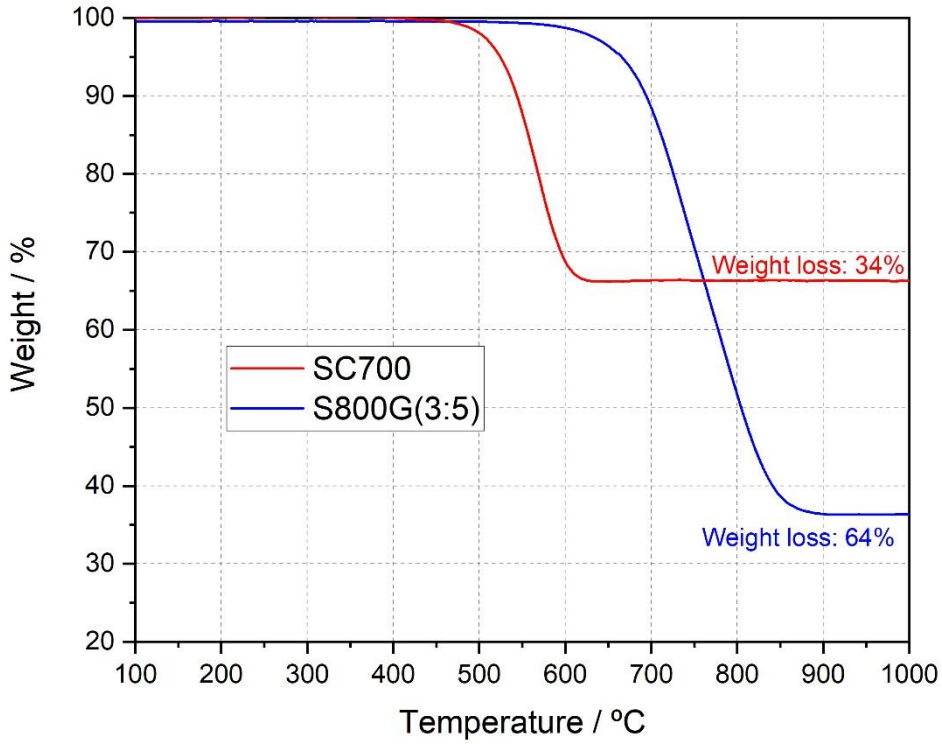

Figure S4. TGA curves of SC700 and S800G(3:5) samples between 100 and 1000 °C.

S5.

Raman spectrum of pristine graphite.

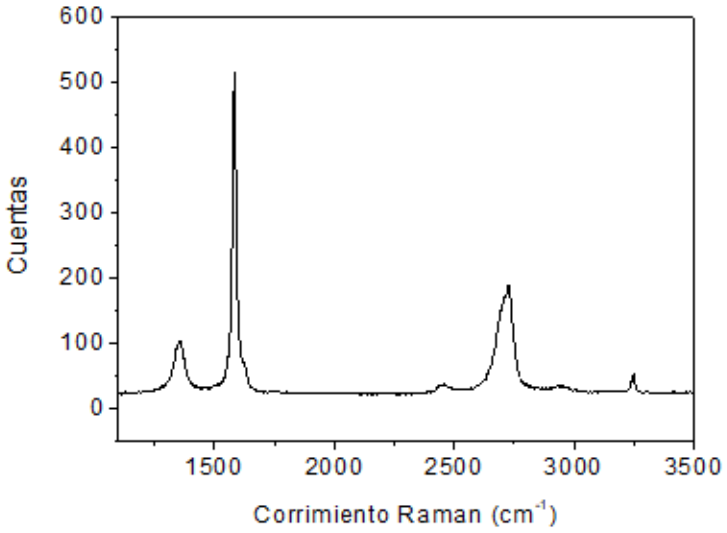

Figure S5. Raman spectrum of pristine graphite.

S6.

Survey XPS spectra of S800, S800G(3:5), and SC700.

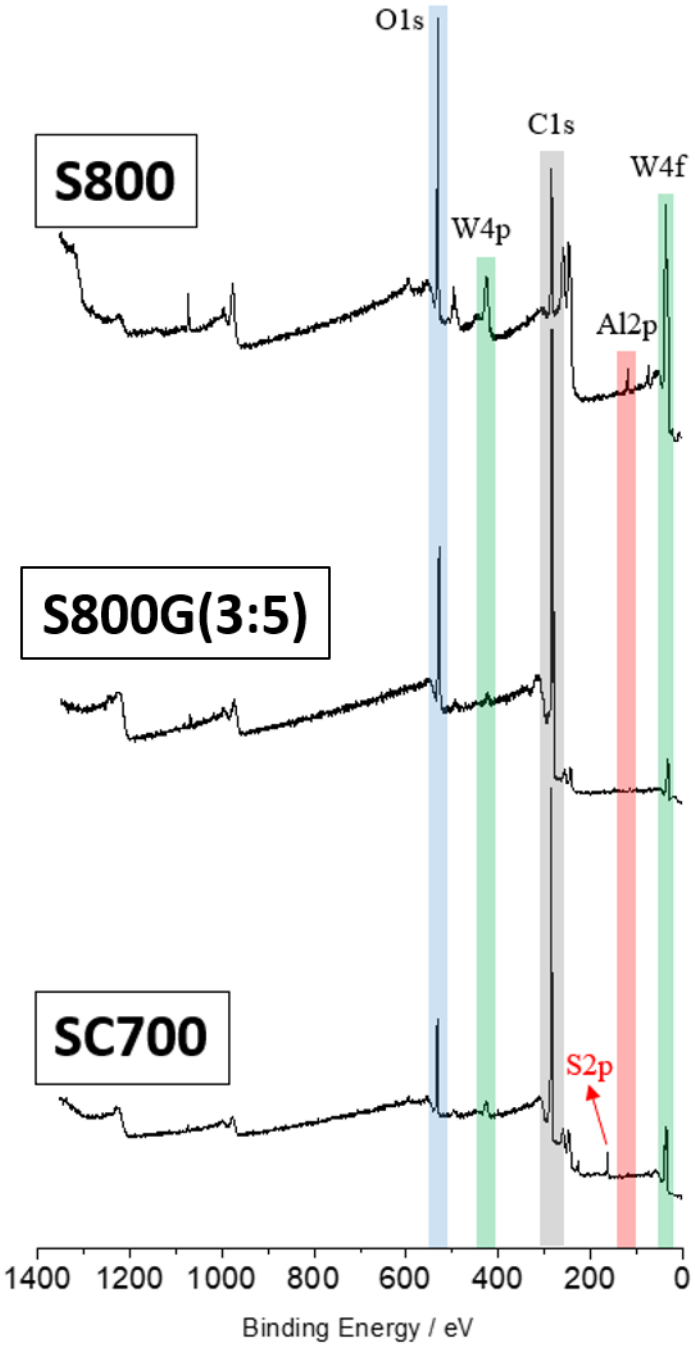

Figure S6. XPS survey spectra of S800, S800G(3:5), and SC700 samples showing the presence of C, O, Al, W, and S (only in the SC700 sample) elements.

S7.

Nitrogen adsorption/desorption isotherm

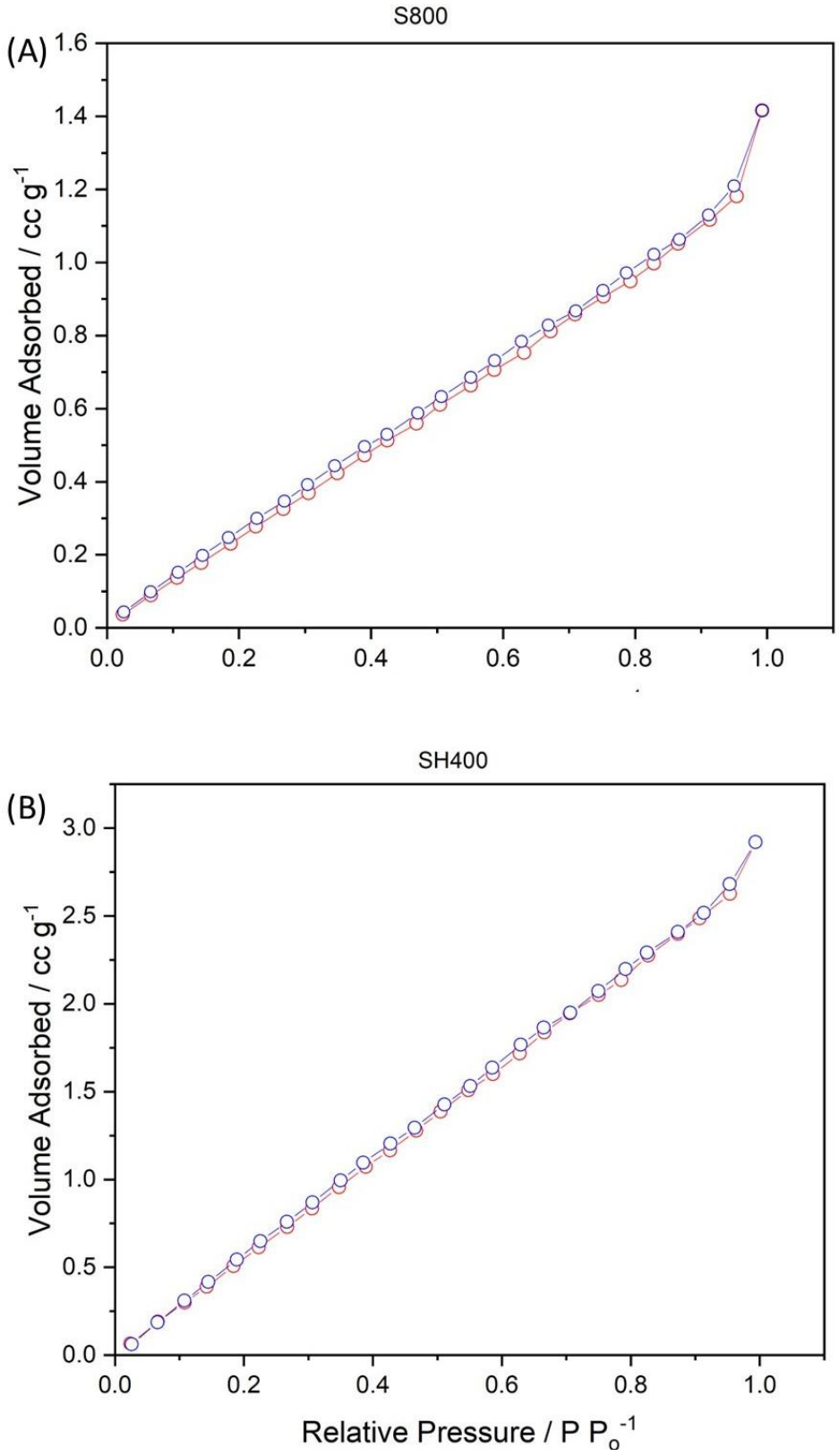

Figure S7. Nitrogen adsorption/desorption isotherm of S800 (A) and SH400 (B) sample.

S8.

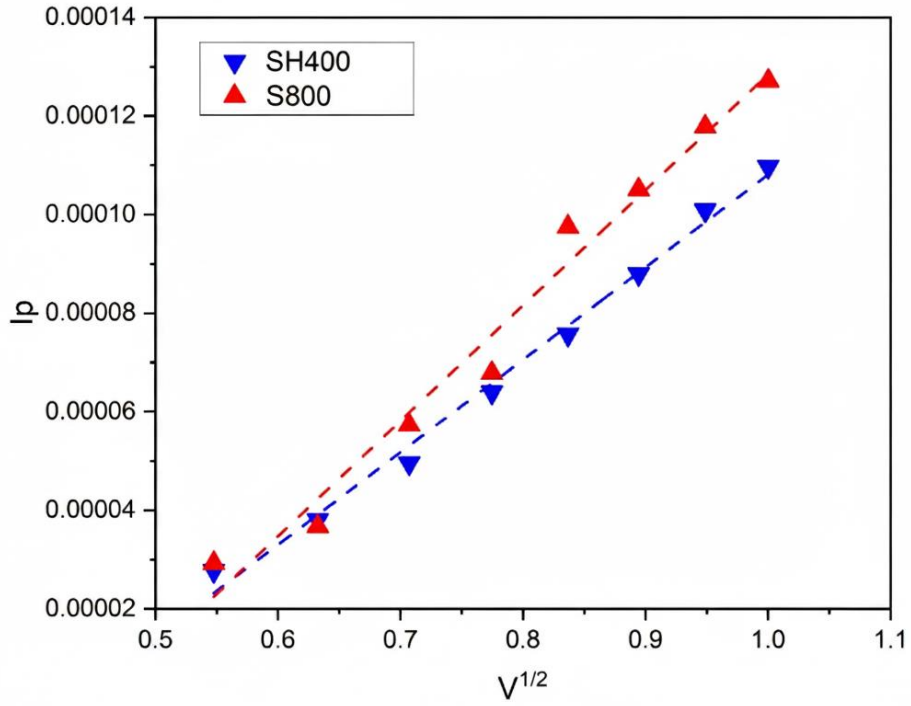

Figure S8. Plotting of peak current *vs.* square root of the scan rate for S800 and SH400.

S9.

Randles-Sevick equation

$$i_p = 2.69\ x\ 10^5 n^{3/2}\ AD^{1/2}\ v^{1/2}\ C$$

Where *ip* is the peak current value, *n* is the number of electrons per reaction species, *A* is the surface area of the electrode, *C* is the bulk concentration of lithium-ion in the electrode, *v* is the scanning rate, and D is the diffusion coefficient. D is the result from the slope of the linear fit *(m)* of the peak current vs. the square root of the scan rates (Figure S2)

$$D = \left(\frac{m}{2{,}69x10^5 * n^{3/2} * A * C}\right)^2$$

$$D_{Li(SH400)} = \left(\frac{0.000187695}{2{,}69x10^5 * 1^{3/2} * 0.00011304\ m * 1200\ {mol}/{m^3}}\right)^2 = 2.65x10^{-17}\ {m^2}/{s}$$

$$D_{Li(S800)} = \left(\frac{0.000234221}{2{,}69x10^5 * 1^{3/2} * 0.00011304\ m * 1200\ {mol}/{m^3}}\right)^2 = 4.12x10^{-17}\ {m^2}/{s}$$

S10.

XRPD pattern

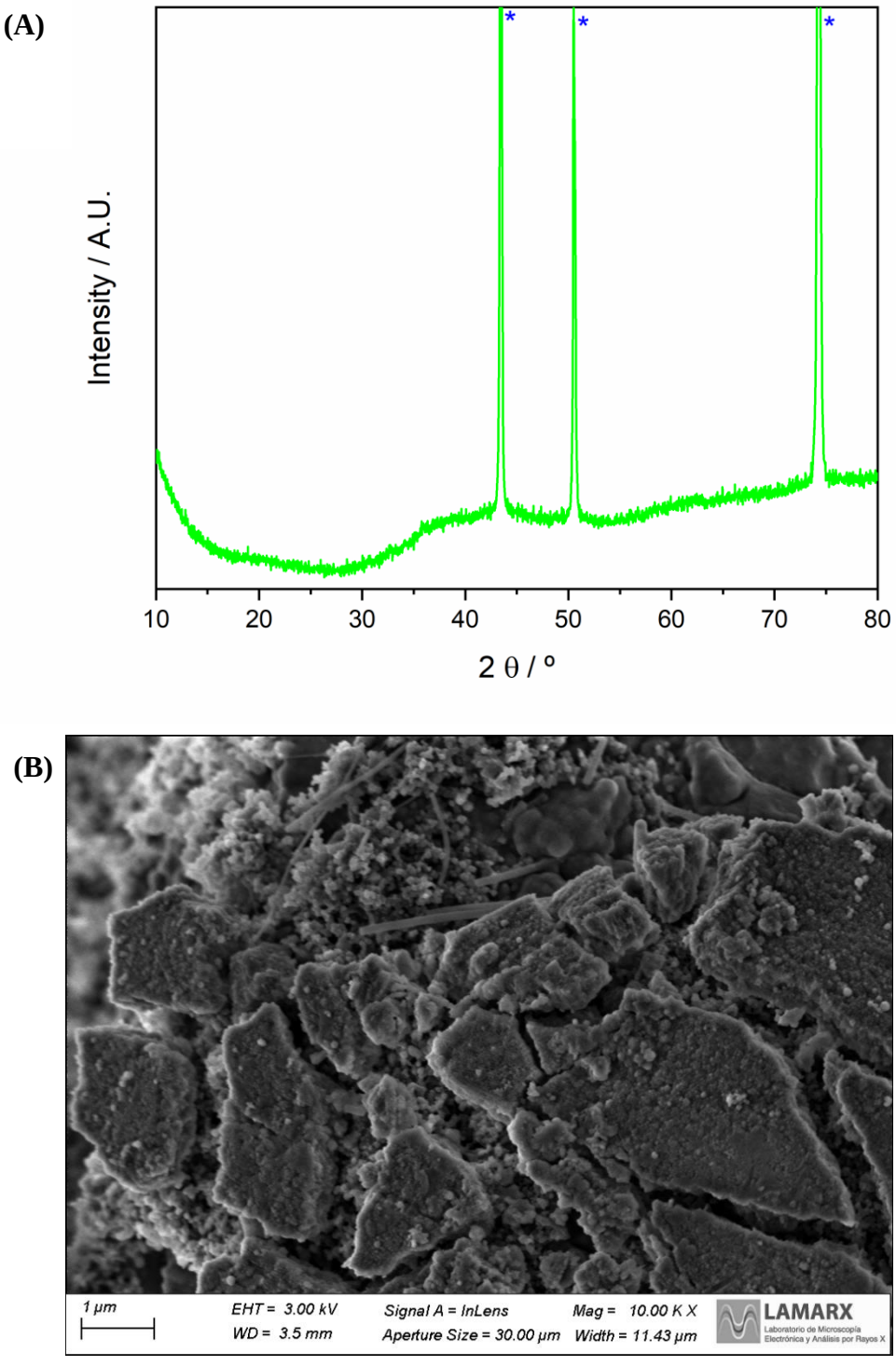

Figure S11. XRPD pattern (A) and SEM image(B) of the S800 sample after the 2nd cycle. * stands for diffraction lines of Cu foil (support of active material, S800).